

AD-A077 030

MCDONNELL DOUGLAS ASTRONAUTICS CO ST LOUIS MO
INJECTION LASER WAVEGUIDE COUPLER.(U)
JUN 79 R R RICE

F/G 20/6

N00173-78-C-0087
NL

UNCLASSIFIED

1 OF 1
AD-A077030



END
DATE
FILMED
12-79
DDC

AD A 077030

DDC FILE COPY

MCDONNELL DOUGLAS AERONAUTICS COMPANY - ST. LOUIS DIVISION

79 11 19 107

MCDONNELL DOUGLAS
CORPORATION

Approved for public release;
distribution unlimited

79 07 19 050

(12)

COPY NO. _____

(6) **INJECTION LASER
WAVEGUIDE COUPLER.**

DDC
RECEIVED
NOV 21 1979
E

(9) **FINAL REPORT,**

(12) 79

(11) **JUNE 1979**

(10) Prepared by: **R. R. Rice et. al.**

Prepared For: Naval Research Laboratory, Washington D. C. 20375
Contract No. N00173-78-C-0087 CDRL Sequence No. A003

(15)

This document has been approved
for public release and sale; its
distribution is unlimited.

404 231

MCDONNELL DOUGLAS AERONAUTICS COMPANY - ST. LOUIS DIVISION
Box 516, Saint Louis, Missouri 63166 (314) 232-0232

MCDONNELL DOUGLAS
CORPORATION

404 231 79 07 19 050 xlt

TABLE OF CONTENTS

	<u>Page</u>
Table of Contents	ii
List of Figures	iii
List of Tables	v
List of Pages	v
1.0 INTRODUCTION	1
2.0 TECHNICAL DISCUSSION	2
2.1 The Injection Laser Radiation Field	2
2.2 Mode Profile of a Ti-Indiffused LiNbO ₃ Waveguide	5
2.3 The Coupling Geometry	18
2.4 Technique for Numerical Evaluation of the Coupling Efficiency	20
2.5 Effects of Transverse Displacement	21
2.6 Effects of Angular Alignment	44
2.7 Comparison with E-ror Function Complement Diffusion Profile	46
2.8 Coupling Calculation - Gaussian Approximation	47
2.9 Laser Diode Development	51
2.10 Waveguide Edge Polishing	53
2.11 Optical Coating Development	53
2.12 Bulk Electromechanical Coupling Experiment	55
2.13 Prototype Coupler	64
2.14 Improved Coupler	68
3.0 CONCLUSION	71
4.0 REFERENCES	72

Accession For NTIS GR&I DOC TAB	Unannounced Justification	By	Distribution/ Availability Codes
Dist Avail and/or special			A

LIST OF FIGURES

<u>FIGURE #</u>		<u>PAGE</u>
1.	COMPARISON OF TE_0 MODE AND GAUSSIAN DISTRIBUTION	4
2.	TE_0 MODE DEPTH VS. DIFFUSION DEPTH	8
3.	TE_0 MODE DEPTH VS. DIFFUSION DEPTH	9
4.	INDIFFUSION TIME VS. TITANIUM THICKNESS	12
5.	TE_0 MODE EFFECTIVE INDEX VS. INDIFFUSION TIME	14
6.	TE_0 MODE EFFECTIVE INDEX VS. INDIFFUSION TIME	15
7.	TE_0 MODE DEPTH VSL INDIFFUSION TIME	16
8.	TE_0 MODE DEPTH VS. INDIFFUSION TIME	17
9.	THE GEOMETRICAL CONFIGURATION OF THE INJECTION LASER LiNbO ₃ WAVEGUIDE COUPLING PROBLEM	18
10.	ANGULAR ALIGNMENT GEOMETRY	19
11.	COUPLING EFFICIENCY VS. $\Delta(\mu\text{m})$, $z = 0.5 \mu\text{m}$	22
12.	COUPLING EFFICIENCY VS. $\Delta(\mu\text{m})$, $z = 0.5 \mu\text{m}$	23
13.	COUPLING EFFICIENCY VS. $\Delta(\mu\text{m})$, $z = 0.5 \mu\text{m}$	24
14.	COUPLING EFFICIENCY VS. $\Delta(\mu\text{m})$, $z = 1.0 \mu\text{m}$	26
15.	COUPLING EFFICIENCY VS. $\Delta(\mu\text{m})$, $z = 1.0 \mu\text{m}$	27
16.	COUPLING EFFICIENCY VS. $\Delta(\mu\text{m})$, $z = 1.0 \mu\text{m}$	28
17.	COUPLING EFFICIENCY VS. $\Delta(\mu\text{m})$, $z = 2.0 \mu\text{m}$	29
18.	COUPLING EFFICIENCY VS. $\Delta(\mu\text{m})$, $z = 2.0 \mu\text{m}$	30
19.	COUPLING EFFICIENCY VS. $\Delta(\mu\text{m})$, $z = 2.0 \mu\text{m}$	31
20.	CALCULATED COUPLING EFFICIENCY VALUE OF MODE DEPTH x_0 AS A FUNCTION OF δ AND Δn	32
21.	MAXIMUM CALCULATED COUPLING EFFICIENCY AS A FUNCTION OF LONGITUDINAL SEPARATION, z_0	33
22.	COUPLING EFFICIENCY VS. $\Delta(\mu\text{m})$, $z = 0.5 \mu\text{m}$	35
23.	COUPLING EFFICIENCY VS. $\Delta(\mu\text{m})$, $z = 0.5 \mu\text{m}$	36
24.	COUPLING EFFICIENCY VS. $\Delta(\mu\text{m})$, $z = 0.5 \mu\text{m}$	37
25.	COUPLING EFFICIENCY VS. $\Delta(\mu\text{m})$, $z = 1.0 \mu\text{m}$	38
26.	COUPLING EFFICIENCY VS. $\Delta(\mu\text{m})$, $z = 1.0 \mu\text{m}$	39
27.	COUPLING EFFICIENCY VS. $\Delta(\mu\text{m})$, $z = 1.0 \mu\text{m}$	40
28.	COUPLING EFFICIENCY VS. $\Delta(\mu\text{m})$, $z = 2.0 \mu\text{m}$	41
29.	COUPLING EFFICIENCY VS. $\Delta(\mu\text{m})$, $z = 2.0 \mu\text{m}$	42
30.	COUPLING EFFICIENCY VS. $\Delta(\mu\text{m})$, $z = 2.0 \mu\text{m}$	43

LIST OF FIGURES
(CONTINUED)

<u>FIGURE #</u>		<u>PAGE</u>
31.	COUPLING EFFICIENCY VS. $\Delta(\mu\text{m})$, $z = 0.5 \mu\text{m}$, AS A FUNCTION OF θ (DEG)	44
32.	COUPLING EFFICIENCY VS. $\Delta(\mu\text{m})$, $z = 1.0 \mu\text{m}$, AS A FUNCTION OF θ (DEG)	45
33.	BEAM RADIUS OF CURVATURE $R(z)$, $w_0 = 0.20396 \mu\text{m}$	46
34.	MODE PROFILE COMPARISON	47
35.	COUPLING EFFICIENCY VS. $\Delta(\mu\text{m})$, $z = 2.0 \mu\text{m}$	48
36.	EFFECT OF PHASE ON COUPLING EFFICIENCY	50
37.	GAUSSIAN BEAM PHASE VARIATION	51
38.	DIODE LAYER CONFIGURATION	51
39.	TRANSVERSE LASER BEAM PROFILE	52
40.	AR COATING FOR WAVEGUIDE EDGE	54
41.	ILD/WAVEGUIDE COUPLER EXPERIMENT	56
42.	PHOTOGRAPH OF THE COUPLING EXPERIMENT	56
43.	SAMPLE OF RAW DATA	57
44.	REDUCTION OF DATA OF FIGURE 43	58
45.	THROUGHPUT EFFICIENCY VS. ILD/WAVEGUIDE SEPARATION	59
46.	THROUGHPUT EFFICIENCY VS. TRANSVERSE DISPLACEMENT	60
47.	FWHM VS. ILD/WAVEGUIDE SEPARATION	61
48.	THROUGHPUT VS. SEPARATION DATA SHOWING FABRY-PEROT EFFECT	62
49.	THROUGHPUT VS. SEPARATION DATA (WITH AR COATING)	63
50.	LONGITUDINAL SENSITIVITY, THEORY AND EXPERIMENT	64
51.	PROTOTYPE COUPLER SCHEMATIC	65
52.	RADIATION PATTERN OF INJECTION LASER DIODE	66
53.	PHOTO OF SOLDERED ILD	67
54.	SOLDERED ILD RADIATION PATTERN	67
55.	IMPROVED COUPLER DESIGN	69
56.	PHOTOGRAPH OF THE IMPROVED COUPLER	70
57.	PHOTOGRAPH OF RADIATION EMERGING FROM WAVEGUIDE EDGE	70

LIST OF TABLES

<u>TABLE NO.</u>		<u>PAGE</u>
1	PERCENTAGE REFLECTANCE VS. WAVELENGTH	55

LIST OF PAGES

Title Page
ii thru v
1 thru 73

1.0 INTRODUCTION

This report summarizes the results of the Injection Laser/Waveguide Coupler Program (Contract N00173-78-C-0087). The program goal was the development and fabrication of an efficient, rugged, single mode laser to thin film optical waveguide coupler that operated over a 30°C temperature range and was stable against vibration and handling for extended periods. The design goals included <1 mW optical power coupled into the waveguide, which was Ti indiffused LiNbO₃, and a spot size at the input to the waveguide not to exceed 10 μm at the (1/e) points. The beam profile was to be as nearly Gaussian as possible, and scattering into the waveguide was to be at least 20 dB below the primary beam.

The program, which was scheduled to be a one-year effort, consisted of the following tasks: (1) waveguide coupling analysis, (2) laser and waveguide development, (3) waveguide edge polishing development, (4) waveguide to laser decoupling development, (5) alignment fixture development, (6) laser/waveguide coupler fabrication, and (7) laser/waveguide coupler evaluation. The program called for the delivery of two laser/waveguide coupler units, the first of which was to be discussed at the end of eight months and the second improved device at the conclusion of the program. This Final Report is being submitted as a deliverable item as required by the contract Statement of Work.

The study leader at MDAC-STL has been Dr. Robert R. Rice, Advanced Space Electronics Department (E413), and the activities under the subcontract to Washington University have been directed by Dr. William S. C. Chang, Laboratory for Applied Electronic Sciences. Other personnel at MDAC-STL who have contributed significantly to the program include Mr. Joseph D. Zino, waveguide measurements; Dr. Dennis G. Hall, waveguide measurements and coupling analysis; Dr. Louis B. Allen, laser diode development; Dr. David A. Bryan, edge polishing and alignment fixture development; and Mr. Philip D. Bear, coupler chip assembly. Substantial contributions were also made by Gordon H. Burkhart, Herbert G. Koenig, and John A. Powers.

Both approximate and exact theoretical analyses of the coupling process conclude that coupling efficiencies of approximately 50% can be expected under typical optimized conditions using a direct end-fire (butt) coupling approach. Subsequent to the development of an edge-polishing and an anti-reflection edge-coating procedure for the Ti:LiNbO₃ waveguides, and after assembly of an apparatus capable of precise alignment of a laser diode and a waveguide, it was shown that a 50% coupling

efficiency could actually be achieved. The sensitivity of the laser/waveguide coupling efficiency to both transverse and longitudinal misalignment was measured using an apparatus with submicron resolution. The measurements showed that the longitudinal separation between the laser diode and the waveguide could be increased to about 15 microns with only a 50% (3 dB) reduction in coupled power. The transverse misalignment sensitivity, on the other hand, was quite severe in that a misalignment of less than one micron resulted in a 50% reduction in coupled power. Because of this stringent transverse alignment constraint, the hybrid coupler chips (a flip-chip configuration with both a LiNbO_3 waveguide and a GaAlAs laser diode bonded to a silicon substrate) did not achieve the theoretical limit of 50% coupling efficiency. The two coupler chips delivered to NRL had coupling efficiencies in the 5% - 10% range.

2.0 TECHNICAL DISCUSSION

2.1 The Injection Laser Radiation Field

In order to calculate the coupling efficiency between a double heterostructure laser diode and a Ti-indiffused LiNbO_3 waveguide, a model for the radiation field of the laser diode must be developed. The electric field patterns of semiconductor lasers have been reported in the literature as closely approximating an elliptical Hermite-Gaussian beam profile^{1,2}.

From the physical data of the heterostructure used in the MDAC-STL laser for the coupling experiments, $\text{Ga}_{0.8}\text{Al}_{0.2}\text{As} - \text{GaAs} - \text{Ga}_{0.8}\text{Si}_{0.2}\text{As}$ with an active region thickness of $2d = 0.2 \mu\text{m}$ and a width of $10\text{-}12 \mu\text{m}$, the radiation field inside the laser diode was also modeled as that of a symmetric waveguide. Using a single mode laser with a center wavelength, $\lambda = 0.8350 \mu\text{m}$, $n(\text{Ga}_{0.8}\text{Al}_{0.2}\text{As}) = 3.495$ and $n(\text{GaAs}) = 3.635$, the electric field of the TE guided modes of this laser was found to be:³

$$E_y(x, z) = A \cos(hd) \exp[-p(|x| - d)] \exp[-j\beta_{\underline{z}}z] \quad (2.1)$$

for $|x| > d$

$$E_y(x, z) = A \cos(hx) \exp[-j\beta_{\underline{z}}z] \quad (2.2)$$

for $|x| < d$

$$A = \left[\frac{2k \sqrt{\frac{w_0}{\epsilon_0}}}{\beta_m \left(\frac{\sin(2hd)}{2h} + d \right)} \right]^{1/2}$$

where $d = 0.1 \mu\text{m}$

$$p = 6.71802 \mu\text{m}^{-1}$$

$$h = 7.38278 \mu\text{m}^{-1}$$

$$\beta_m = 26.3373 \mu\text{m}^{-1}$$

$$k = 7.52477 \mu\text{m}^{-1}$$

A laser diode typically has an active region that has a very large width and a very small height. Thus its radiation field can best be approximated by a two-dimensional gaussian beam (i.e., an elliptical gaussian beam with a very wide beam width in the y direction). For a two-dimensional gaussian beam ($\frac{\partial}{\partial y} = 0$) with its beam waist at $z = 0$, its E-field is:

$$E(x,0) = A \exp(-x^2/w_0^2). \quad (2.3)$$

In order to approximate a guided wave mode, the half-beam width, w_0 , was adjusted so that the magnitude of the electric field will be A/e at the same value of x as the TE_0 mode given in Equations 2.1 and 2.2. Thus,

$$w_0 = \frac{1 + \ln[\cos(hd)]}{p} + d. \quad (2.4)$$

For the mode given in Equation 2.1, a value of $w_0 = 0.20396 \mu\text{m}$ was obtained. Figure 1 shows a plot of both the gaussian beam and the TE_0 mode at $z = 0$. It is clear that the transverse pattern of the TE_0 waveguide mode of the laser can be closely approximated by a gaussian field variation at $z = 0$.

COMPARISON OF TE_0 MODE AND GAUSSIAN DISTRIBUTION

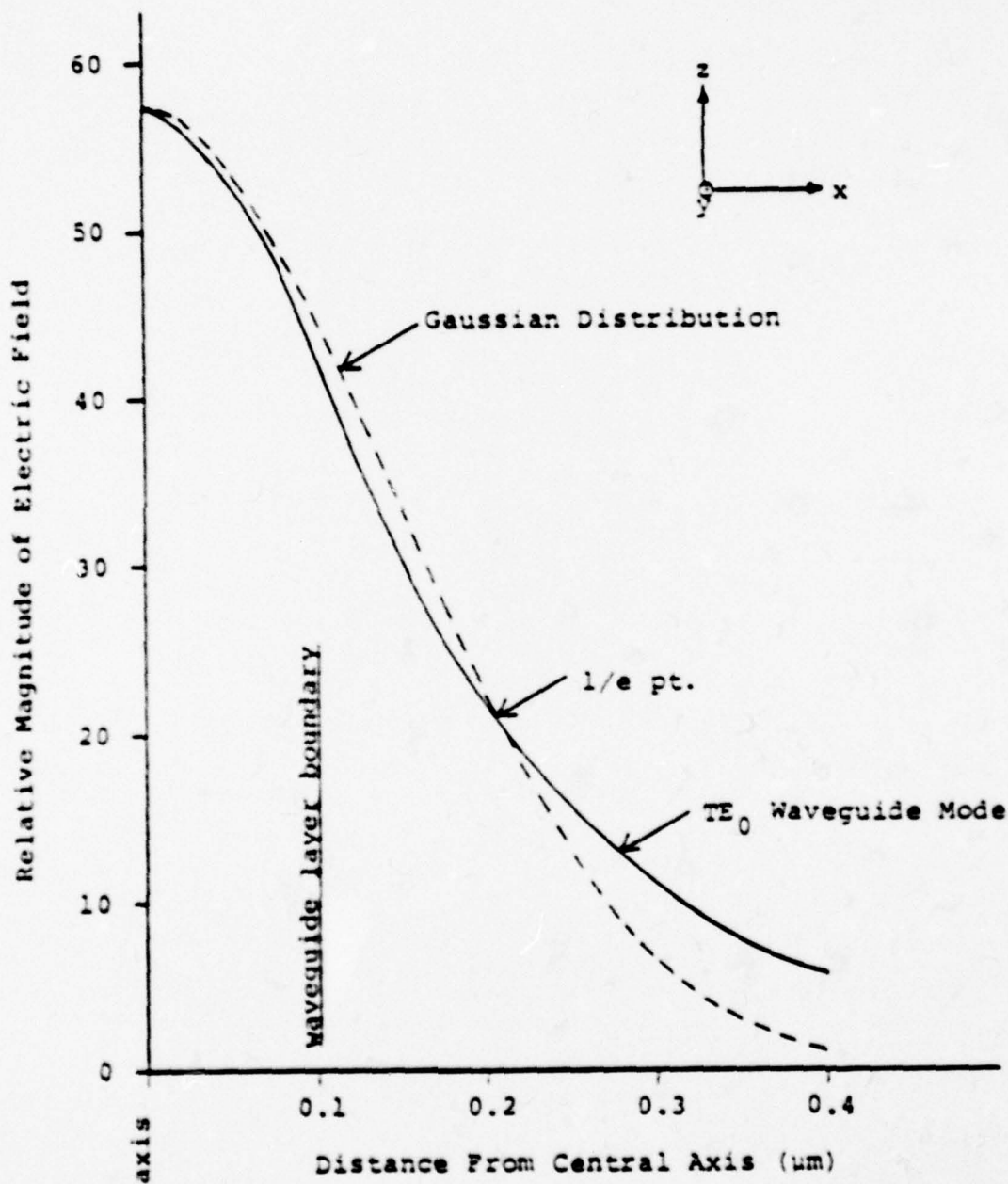


FIGURE 1

Based upon the preceding discussion, the following expression was used to describe the electric field of the laser diode in all of the analysis:

$$\psi_{inc} = A \sqrt{\frac{k}{2}} \frac{w_0 (j - 1)}{\sqrt{2z + jkw_0^2}} \exp(-jkz) \exp \left[\frac{-j2kz x^2}{4z^2 + (kw_0^2)^2} \right] \exp \left[\frac{-(kw_0^2 x)^2}{4z^2 + (kw_0^2)^2} \right]. \quad (2.5)$$

Clearly, there are also other methods that may be used to fit a gaussian beam to the radiation field of an injection laser. For example, one may choose to fit the gaussian beam to the far field radiation pattern of the laser. In that case, a different w_0 value will be obtained.

2.2 Mode Profile of a Ti-Indiffused LiNbO₃ Waveguide

Computation of the overlap integral between the laser diode radiation field and the LiNbO₃ waveguide guided wave mode requires the determination of the mode profile (i.e., the transverse x variation of the TE₀ mode) of an indiffused waveguide as a function of the waveguide parameters. In the following subsections, (a) the relationship between the mode profile and the diffusion profile; (b) the diffusion profile that may be obtained experimentally; and (c) the electric field of the TE₀ mode, will be discussed.

Optical waveguides have a refractive index which is a smoothly varying function of depth higher near the surface than in the bulk material. Theoretical analyses of the modes of LiNbO₃ waveguides have been performed for refractive index variations in the form of a complementary error function, a gaussian function, or an exponential function⁴⁻⁷.

Of the three profiles listed above, only the TE modes of the exponential profile can be obtained analytically in a closed form⁷. For the convenience of numerical calculation, the diffusion profile of the Ti atoms, i.e., the assumed profile of refractive index, has been approximated by an exponential variation. Later it will also be shown that such an approximation does not lead to a large error in the calculation of coupling efficiency for a specific example.

For a given diffusion profile the mode profile is determined whenever the propagation wave number β of the mode is known. In a Ti-indiffused waveguide the relationship between the normalized diffusion depth, V , normalized mode index, b , for various diffusion profiles has already been given by Hocker and Burns⁴. Assuming an exponential diffusion profile ($f(x) = e^{-x}$) and requiring a single mode waveguide ($m = 0$), one obtains:

$$2V \int_0^{-\ln(b)} (e^{-x} - b)^{1/2} dx = 3\pi/2 \quad (2.6)$$

where $V =$ normalized diffusion depth

$$= k_0 \delta [(n_b + \Delta n)^2 - n_b^2]^{1/2} \quad (2.7)$$

$b =$ normalized mode index

$$= (n_{\text{eff}}^2 - n_b^2) / [(n_b + \Delta n)^2 - n_b^2] \quad (2.8)$$

Here, n_b is the refractive index of the substrate ($n_b = 2.18$ at $\lambda = 0.8350 \mu\text{m}$), $\Delta n + n_b$ is the refractive index at the waveguide top surface and δ is the diffusion depth. n_{eff} is the effective index of the mode (i.e., normalized propagation constant β/k).

The only approximations that have been made in obtaining Equation 2.6 are

$$\Delta n \ll n_b \quad \text{and} \quad \tan^{-1} \left[\frac{n_{\text{eff}}^2 - 1}{(n_b + \Delta n)^2 - n_{\text{eff}}^2} \right]^{\frac{1}{2}} \approx \frac{1}{2}.$$

Substituting $y = e^{-x}$ into Equation 2.6, one obtains

$$V = \frac{\Delta n}{\delta} = \left[\int_1^b \frac{(y-b)^{\frac{1}{2}}}{y} dy \right]^{-1}$$

$$= \frac{\Delta n}{\delta} = \left\{ \left[2(y-b)^{\frac{1}{2}} - 2b^{\frac{1}{2}} \tan^{-1} \left[\left(\frac{y-b}{b} \right)^{\frac{1}{2}} \right] \right]_1^b \right\}^{-1}$$

or

$$V = \frac{\Delta n}{\delta} = \left\{ \sqrt{1-b} - \sqrt{b} \tan^{-1} \sqrt{(1/b) - 1} \right\}^{-1} = 0. \quad (2.10)$$

For a given V , Equation 2.10 can be solved for b using Newton's method. This numerical solution yields values of b , (i.e., values of n_{eff}) as a function of V (i.e., Δn and δ that are controlled by the experimental process). Although solutions of b have already been presented graphically in Reference 4, the above procedure determines n_{eff} to the high degree of accuracy necessary for subsequent numerical calculations.

For a given b (i.e., n_{eff}), one can define a mode depth x_0 where x_0 is the absolute value of x_1 (i.e., $|x_1|$) at which $n(x_1) = n_{\text{eff}}$

$$x_0 = -\delta \ln \left[\frac{n_{\text{eff}} - n_b}{\Delta n} \right]. \quad (2.11)$$

The mode depth defined in this manner has the physical meaning of being the starting point of the evanescent tail of the electric field. In a strongly guided mode, one may assume that most of the optical power is confined in the region from $x = 0$ to $x = x_0$. In a weakly guided mode the power interpretation of the mode depth is not correct. Figures 2 and 3 show the calculated mode depth x_0 given in Equation 2.11 as a function of diffusion depth, δ , for various Δn values at $\lambda = 0.6328 \mu\text{m}$ and $\lambda = 0.8350 \mu\text{m}$. Observe that x_0 (or n_{eff}), useful for r.f. spectrum analysis applications, is limited by the requirements for both single-mode operation (shown as a dashed line) and ease in experimental fabrication process (shown as the line with dot-dashes). In the region above the line for easy experimental control of x_0 , small variations in δ or Δn will yield very large variations in x_0 implying that in the latter region it would be difficult

TE₀ MODE DEPTH VS DIFFUSION DEPTH

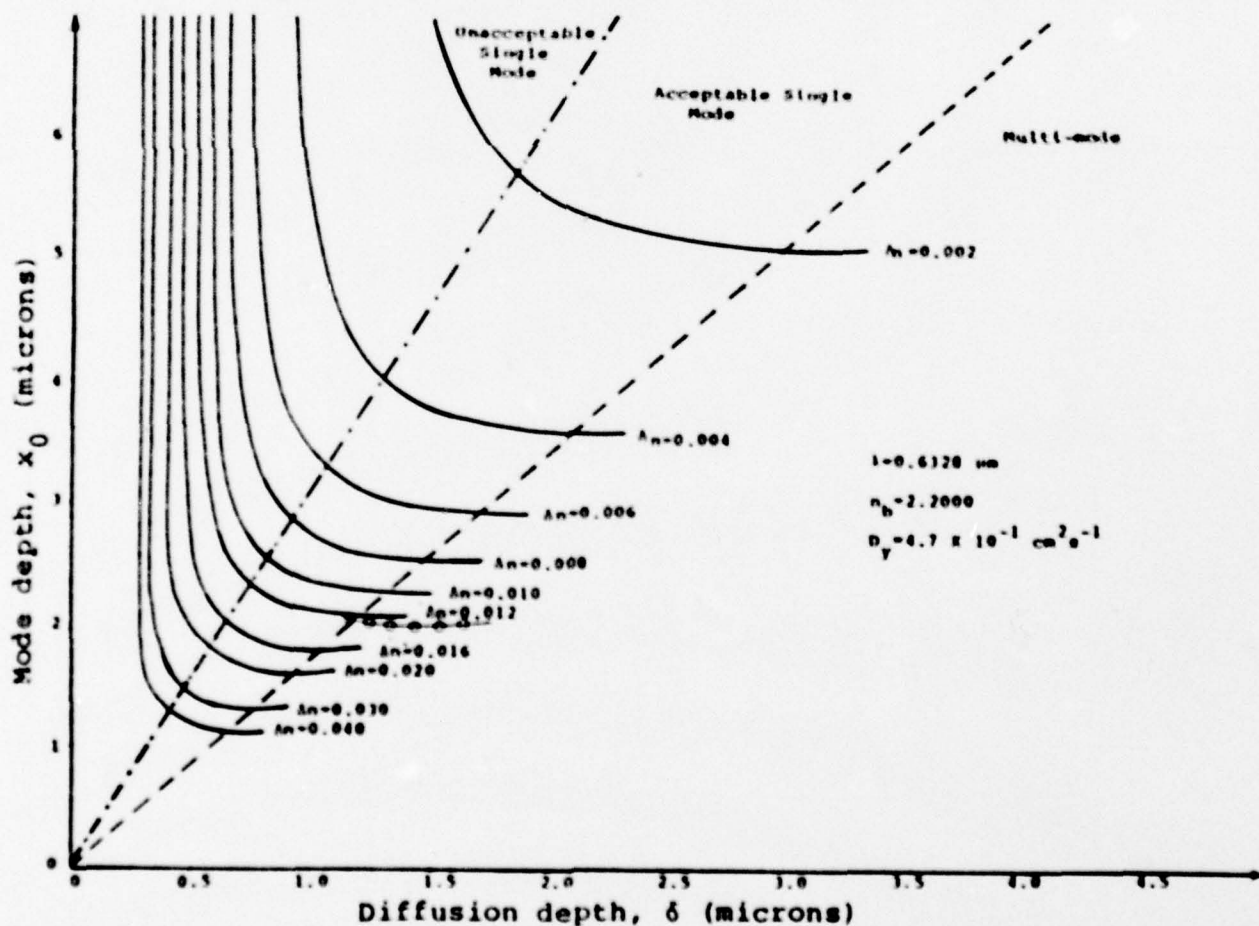


FIGURE 2

TE₀ MODE DEPTH VS DIFFUSION DEPTH

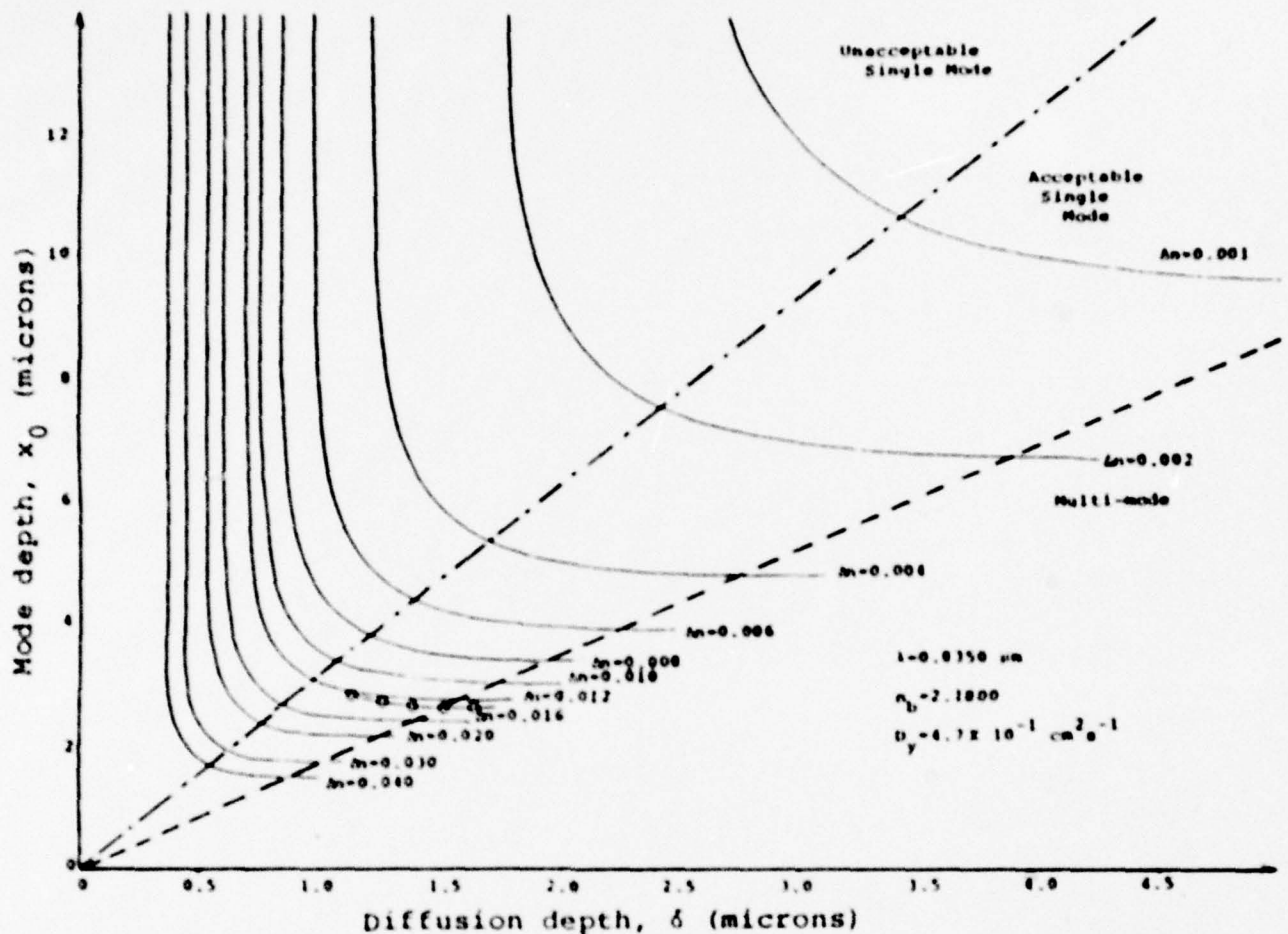


FIGURE 3

to control the mode depth experimentally. As it will be discussed in a later section, the coupling efficiency will be very small unless the mode depth, x_0 , of the fabricated waveguide can be kept small. Therefore, it is apparent that the only useful region is that between the dashed line and line with dot-dashes. Numerical calculations of coupling efficiency will be limited to this region.

The Ti-indiffused LiNbO_3 waveguides were fabricated according to the following procedure. The waveguide substrates were Y-face cut LiNbO_3 , polished to $\lambda/10$ on the top surface. A Ti film $\pm \text{\AA}$ thick was deposited on the top surface in an Ar atmosphere using a r.f. sputtering apparatus. The sample was placed Ti covered side face down on platinum foil lining the bottom of an Al_2O_3 boat, placed in an Al_2O_3 furnace tube and flushed with Ar gas at 30 cc/min for two hours. The flow rate was changed to 6.25 cc/min and the furnace temperature was raised to 1000°C in thirty minutes. At twelve minutes before the end of the diffusion run, the diffusion atmosphere was changed to O_2 at a flow rate of 6.28 cc/min. At time

t, the end of the diffusion run, the furnace was shut off and allowed to cool slowly (overnight) to room temperature in the O_2 atmosphere at 6.25 cc/min. For such a diffusion process, diffusion theory predicts that

$$D = \text{diffusion constant} = D_0 \exp(-T_0/T), \quad (2.12)$$

$$\delta = 2 \sqrt{Dt}. \quad (2.13)$$

For this process, D is the diffusion coefficient along the y direction (D_y) in the $LiNbO_3$ crystal (\vec{y} is perpendicular to the top surface in this geometry). Optical mode measurements at $0.6328 \mu m$ have been used to determine the y component, D_y , of the anisotropic diffusion coefficient for this process of fabricating $Ti:LiNbO_3$ waveguides. Specifically, experimentally obtained effective mode indices, n_{eff} , have been fit to published normalized mode dispersion curves⁴ under the assumption of a gaussian index profile, with the result $D_y = 5.0 \times 10^{-13} \text{ cm}^2 \text{ s}^{-1}$ at 1000°C . Similar measurements on waveguides fabricated at 1025°C indicate, using Equation 2.12, that $D_y = 6.8 \times 10^{-4} \text{ cm}^2 \text{ s}^{-1}$ and $T_0 = 2.7 \times 10^4 \text{ K}$. Comparable data of Naitoh *et al*⁸ yield $D_y = 1.6 \times 10^{-12} \text{ cm}^2 \text{ s}^{-1}$ at 1000°C . From direct probing of waveguides of known diffusion parameters, Fukuma *et al*⁹ found $D_y = 4.6 \times 10^{-13} \text{ cm}^2 \text{ s}^{-1}$ at $T = 1000^\circ\text{C}$ and Burns *et al*¹⁰ found $D_y = 4.6 \times 10^{-13} \text{ cm}^2 \text{ s}^{-1}$ at $T = 1000^\circ\text{C}$. For the following calculations, a value of $D_y = 4.7 \times 10^{-13} \text{ cm}^2 \text{ s}^{-1}$, which is the average of fit and the latter two values from the probing experiments, has been assumed.

The Ti concentration in $LiNbO_3$ using the exponential profile approximation is given by

$$C(x_1, z) = \frac{\alpha T}{\delta} \exp(x_1/\delta) \quad \text{for } x_1 < 0 \quad (2.14)$$

where α is the number of atoms per unit volume in the sputter deposited film ($\alpha = 5.71 \times 10^{22} \text{ cm}^{-3}$), t is the thickness of Ti deposited on the top surface

(units: °A), and C is normalized such that $\int_{-\infty}^0 C(x_1, t) dx_1 = \alpha\tau$. The quantity Δn is related⁶ to C by $\Delta n = C(0) \frac{dn}{dC}$ where $\frac{dn}{dC} = 1.6 \times 10^{-23} \text{ cm}^3$. Thus,

$$\begin{aligned} \Delta n &= \frac{\alpha\tau}{\delta} \frac{dn}{dC} \\ &= \frac{\tau}{\sqrt{t}} 8.6020 \times 10^{-4} \end{aligned} \quad (2.15)$$

where τ is in units of Å and t is in units of minutes. Equations 2.12, 2.13, and 2.14 relate the parameters Δn and δ to the experimental parameters τ , t and T that are used in the actual fabrication process.

For a given Ti layer thickness, τ , if the diffusion time t is less than a minimum value, t_{\min} , there will be a layer of TiO_2 residue left on the surface after diffusion. It is well known that such a TiO_2 residue will increase the scattering loss and the surface roughness. There is no generally accepted criterion regarding the maximum thickness of a TiO_2 layer that can remain on the waveguide surface without introducing significant attenuation. The following qualitative visual inspection criterion for "no TiO_2 residue" was devised: Let there be a step discontinuity of the deposited Ti film pattern in the form of a straight edge. After diffusion, the sample is placed under an optical microscope focused on the top surface, at 700X magnification, using neither filter nor polarizer, in the transmission mode. The boundary line separating the Ti and NO-Ti region should be clearly visible, and the sample is translated slowly under the microscope in a direction parallel to the boundary line. By comparing the two regions and by correlating the observation with the linear motion, one can now recognize any surface defects such as TiO_2 residue patterns that may occur in one region and not in the other region. If both regions appear to be identical, the sample is classified as having no TiO_2 residue. If there are TiO_2 residue patterns in one region, the sample is then scanned in a direction perpendicular to the boundary line to assess the total extent of TiO_2 residue.

Using the preceding criteria, the TiO_2 residue on LiNbO_3 waveguide surfaces was examined after different diffusion times for several Ti thicknesses. The result of this experimental investigation is shown in Figure 4. From this

INDIFFUSION TIME VS TITANIUM THICKNESS

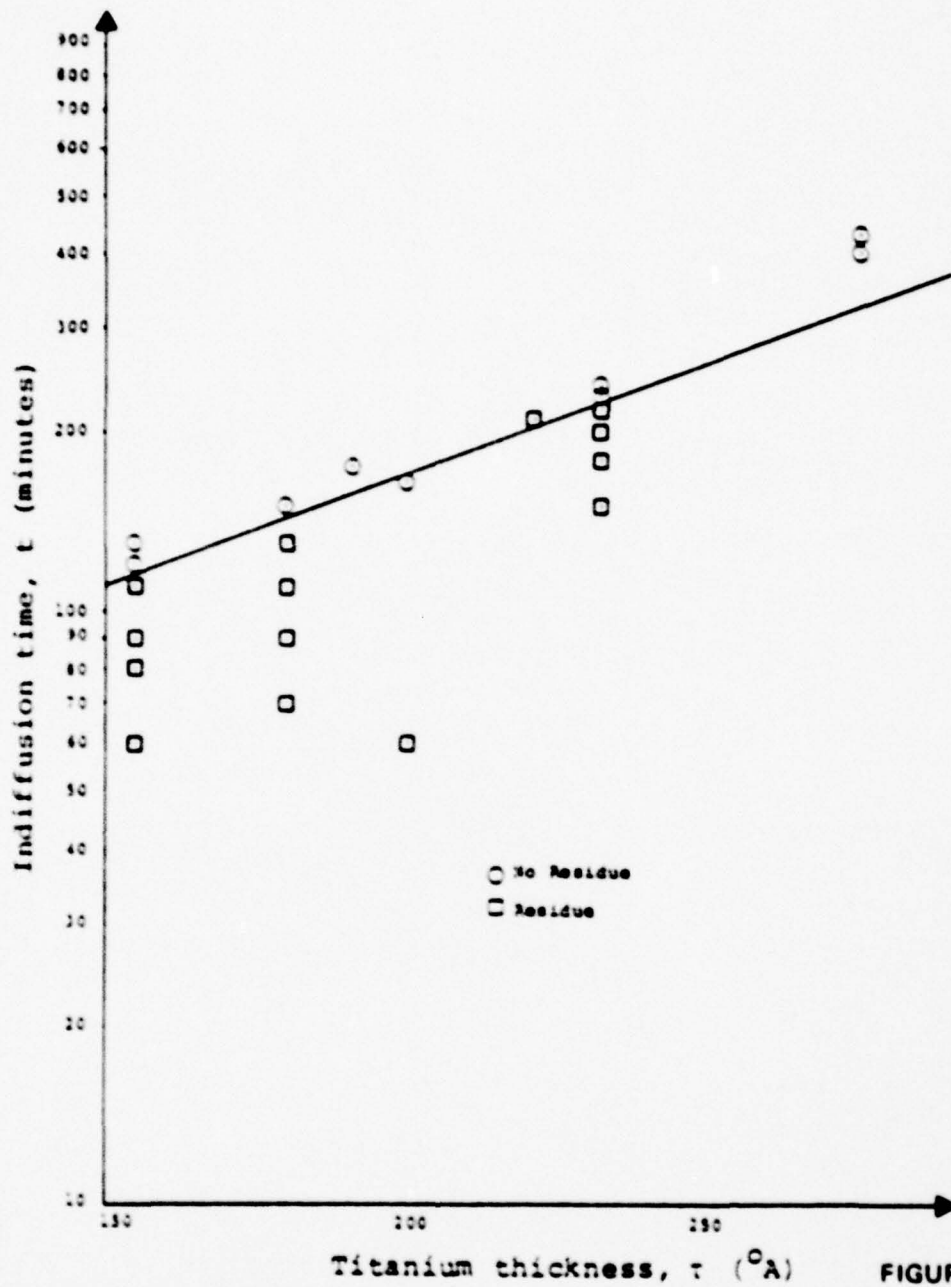


Figure it was clear that for $150 \text{ \AA} \leq \tau \leq 250 \text{ \AA}$, t_{\min} could be defined empirically by

$$t_{\min} = 29.23 \exp [0.0088 \tau] . \quad (2.16)$$

Equation 2.16 (i.e., the no-residue limit) is represented by the solid curve with circles in Figure 3. The calculated mode effective index, n_{eff} , of the TE_0 mode is plotted as a function of diffusion time t for various Ti layer thicknesses in Figures 5 and 6. Figures 7 and 8 are Figures 2 and 3 replotted with mode depth, x_0 , as a function of diffusion time, t , for various thicknesses, τ , of the deposited Ti layer. The non-residue limit and the lines for easy experimental control and for single mode operation are indicated once more in these Figures. Clearly, one is only interested in waveguides that fall within these limits.

For a LiNbO_3 waveguide with an exponentially varying Ti atom concentration⁷, one finds:

$$n(x_1) = n_b + \Delta n \exp(x_1/\delta) \quad (2.17)$$

where n_b is the refractive index of the substrate ($n_b = 2.18$ at $\lambda = 0.8350 \mu\text{m}$), $\Delta n + n_b$ is the refractive index on the waveguide top surface, and δ is the diffusion depth.

Using Conwell's result, the electric field of the TE_0 mode of the LiNbO_3 waveguide is given by

$$\psi_1 = A_1 J_{u_b} \left[\xi \exp\left(\frac{x_1}{2\delta}\right) \right] \exp(-j\beta z) \quad \text{for } x_1 \leq 0 \text{ in } \text{LiNbO}_3 \quad (2.18)$$

$$\psi_1 = A_1 J_{u_a}(\xi) \exp\left[-u_a \frac{x_1}{2\delta}\right] \exp(-j\beta z) \quad \text{for } x_1 > 0 \text{ in air} \quad (2.19)$$

where

$$J_{u_b} = \text{Bessel function of the order } u_b$$

$$u_b = 2k\delta [n_{\text{eff}}^2 - n_b^2]^{1/2} \quad (2.20)$$

$$\xi = 2k\delta [2n_b \Delta n]^{1/2}$$

$$u_a = 2k\delta [n_{\text{eff}}^2 - 1]^{1/2}$$

$$A_1 = \text{constant}$$

$$n_{\text{eff}} = \text{effective index of the mode} = \beta/k.$$

TE₀ MODE EFFECTIVE INDEX VS INDIFUSSION TIME

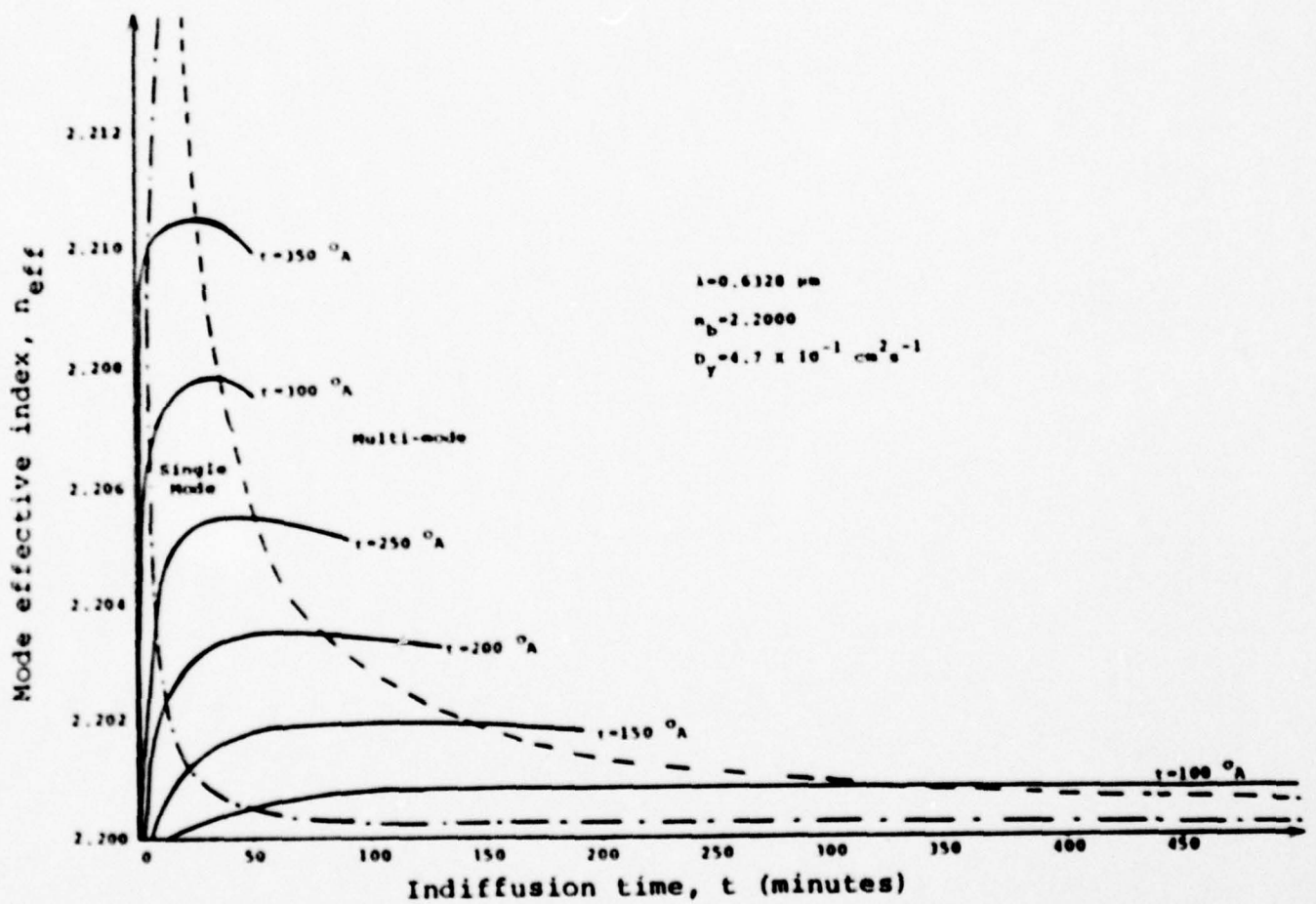


FIGURE 5

TE₀ MODE EFFECTIVE INDEX VS INDIFFUSION TIME

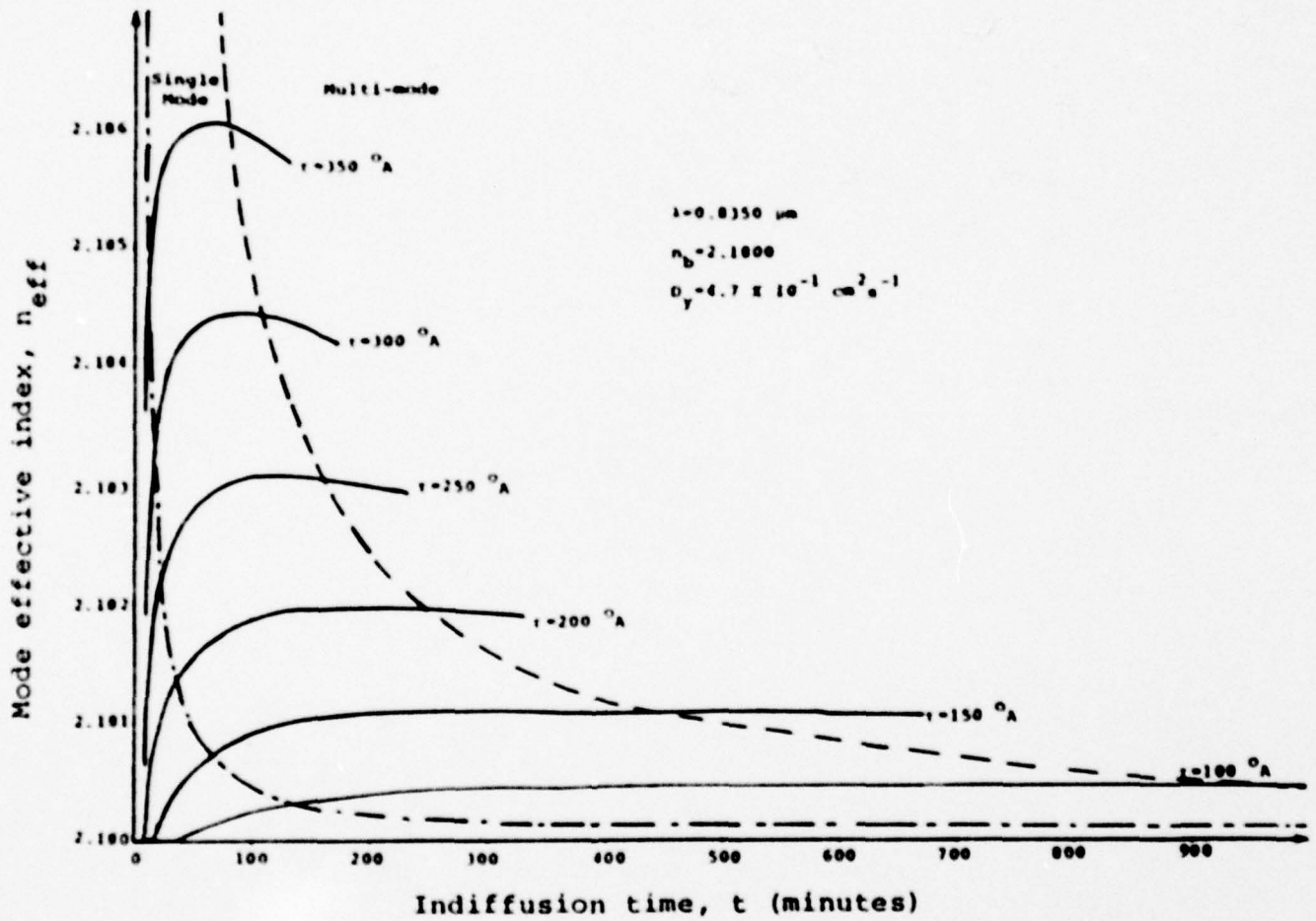


FIGURE 6

TE₀ MODE DEPTH VS INDIFFUSION TIME

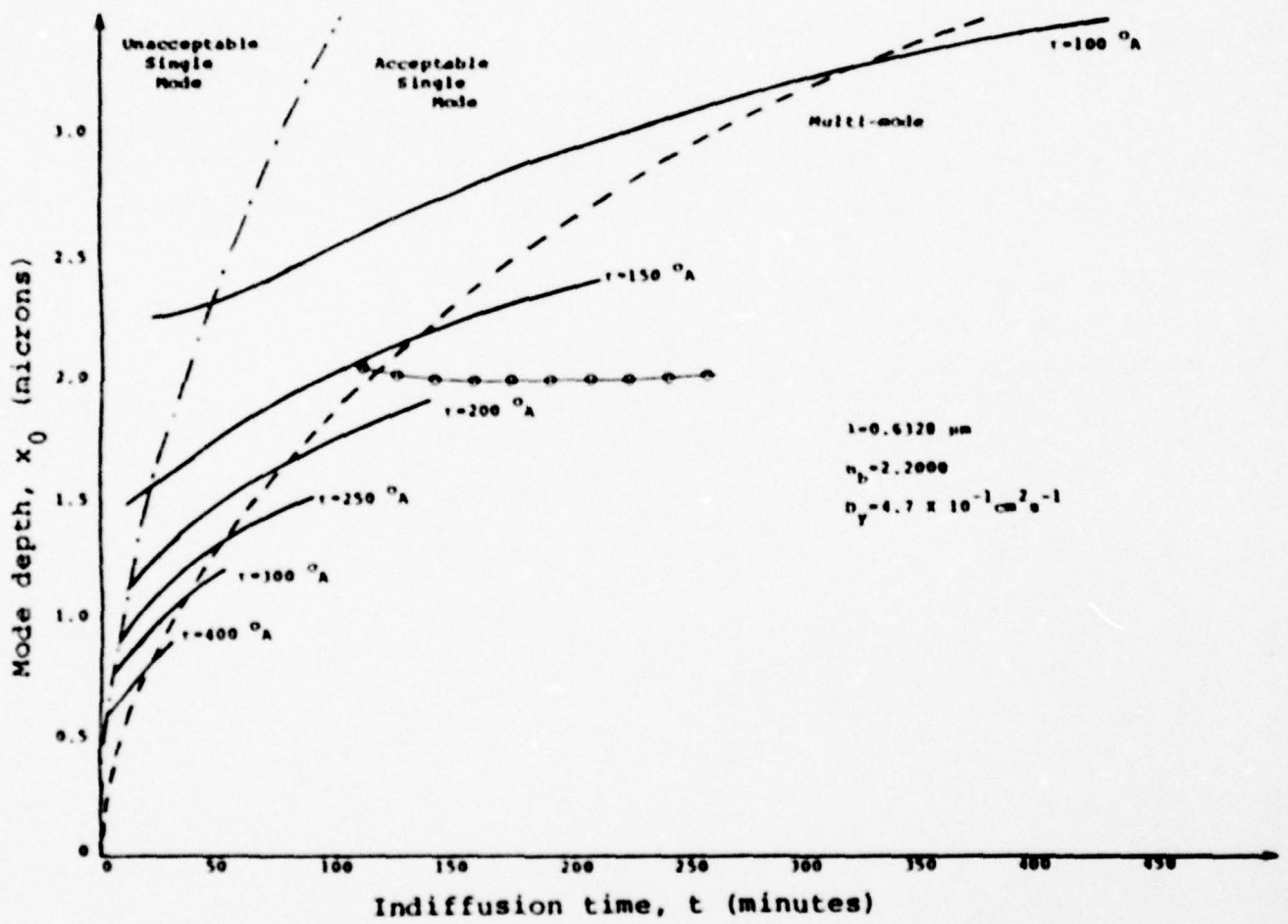


FIGURE 7

TE₀ MODE DEPTH VS INDIFFUSION TIME

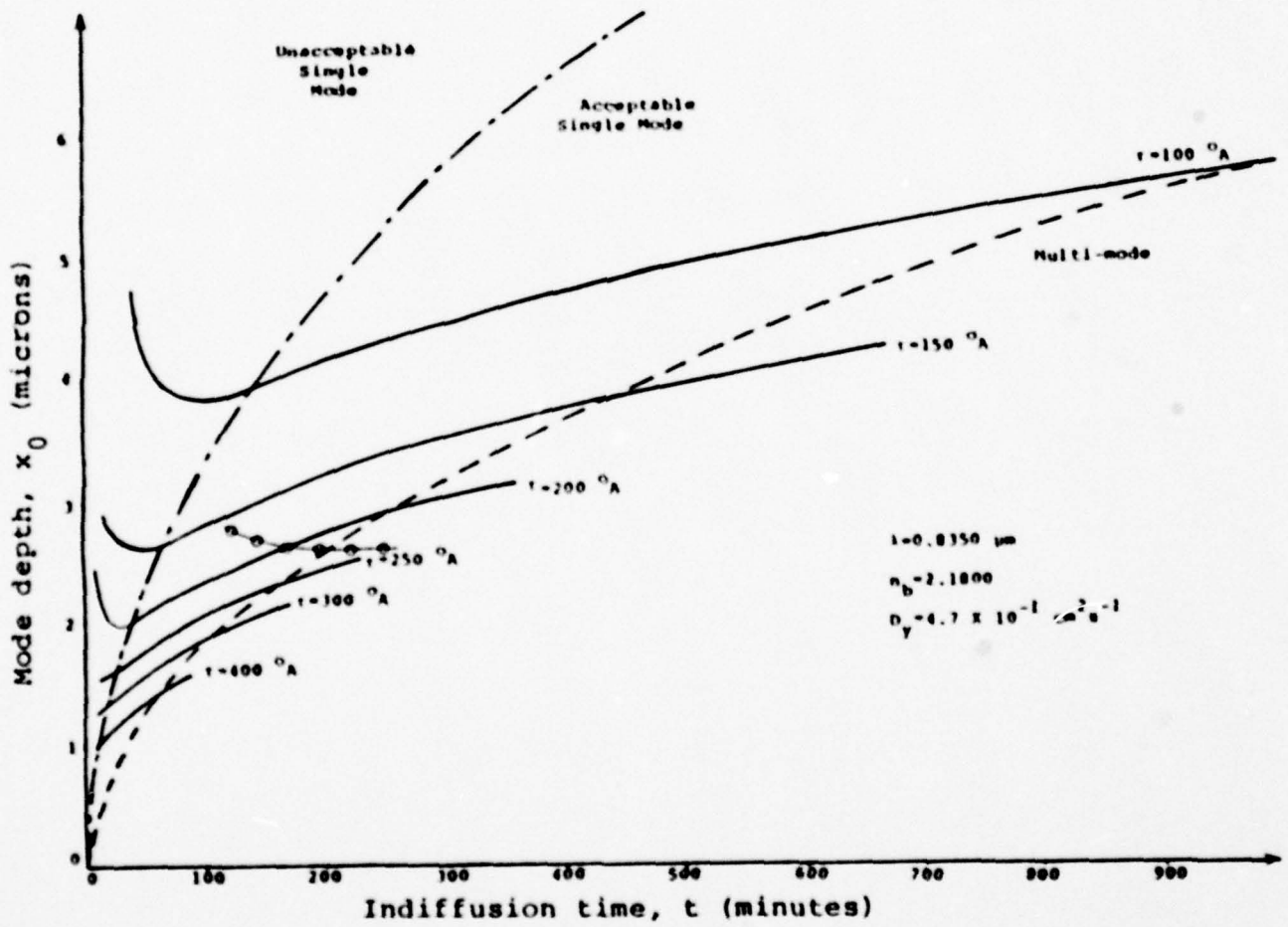


FIGURE 8

2.3 The Coupling Geometry

The first part of the calculation assumes; (a) that the directions of guided wave propagation in the GaAs laser diode and the LiNbO_3 waveguide are parallel (i.e., perfect angular alignment with $\vec{z} \parallel \vec{z}_1$ and (b) that the end surface of LiNbO_3 waveguide is antireflection coated to eliminate reflections. The geometrical configuration for this part of the calculation is illustrated in Figure 9. Here z_0 is the longitudinal separation and Δ is the transverse displacement of the top surface of the LiNbO_3 waveguide with respect to the center of the laser diode GaAs active layer.

THE GEOMETRICAL CONFIGURATION OF THE INJECTION LASER-LiNbO₃ WAVEGUIDE COUPLING PROBLEM

Side View

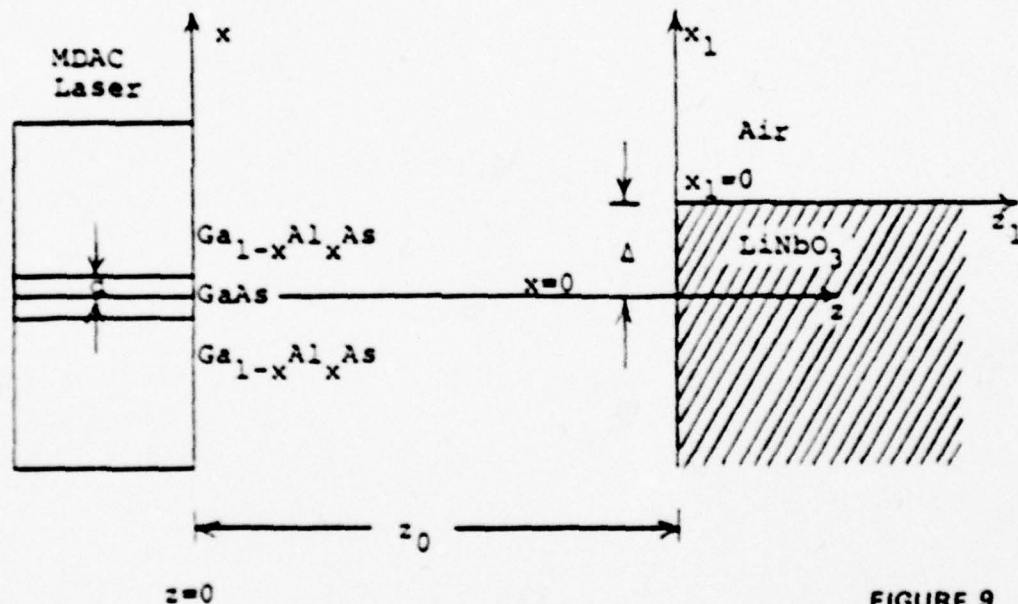


FIGURE 9

In the second part of the calculation the angular alignment, θ , becomes a variable. The geometry for this part of the calculation is shown in Figure 10. The angle, θ , between directions of the propagation of the guided wave mode in the GaAs laser diode (also the propagation direction of the gaussian beam), \vec{z} , and the direction of propagation of the TE_0 mode in the LiNbO_3 waveguide, \vec{z}' , is defined to be positive when it is measured from the \vec{z}' axis in the counter-clockwise direction. \vec{z} is parallel to \vec{z}' when $\theta = 0$. The displacement, Δ , for

ANGULAR ALIGNMENT GEOMETRY

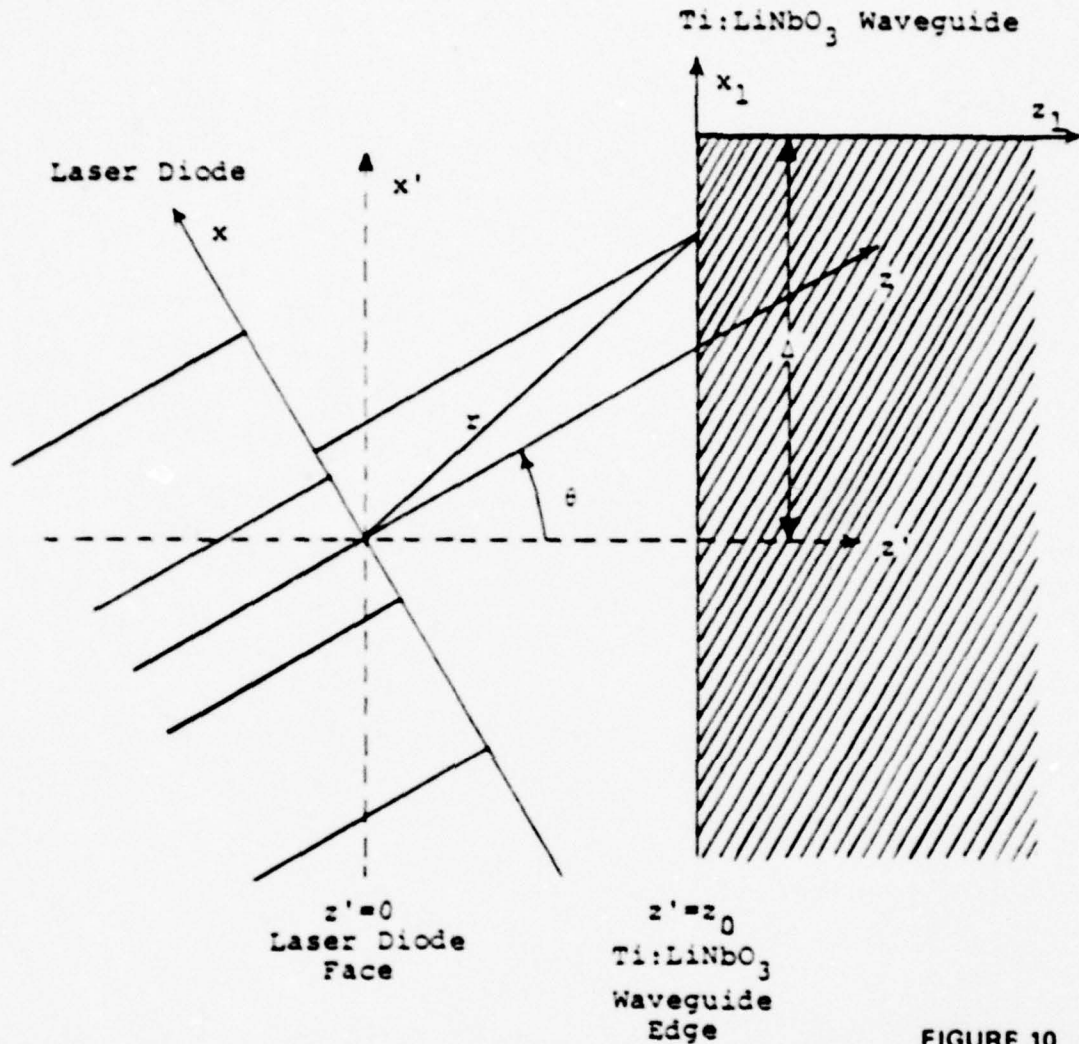


FIGURE 10

this part of the calculation, is the transverse displacement of the top surface of the LiNbO₃ waveguide with respect to the z' axis. Constant z₀ values were chosen for this part of the calculation.

To obtain the incident field on the LiNbO₃ waveguide from the incident beam given by Equation 2.5, a transformation from x, y, z to x', y', z' coordinates will be made. The appropriate transformation is:

$$x = x' \cos \theta - z_0 \sin \theta \quad (2.21)$$

$$z = x' \sin \theta + z_0 \cos \theta \quad (2.22)$$

where x' is the axis parallel to the LiNbO₃ waveguide edge and z₀ is the axial displacement.

Substituting Equations 2.21 and 2.22 into Equation 2.5, one obtains the following incident field on the LiNbO_3 waveguide end surface at $z' = z_0$:

$$\begin{aligned} \psi_{\text{inc}}(x_1, \theta) &= \frac{A \sqrt{k}}{\sqrt{z}} \frac{w_0 (j-1) \exp[-jk(x_1 \sin \theta + z_0 \cos \theta)]}{\sqrt{4(x_1 \sin \theta + z_0 \cos \theta)^2 + jk w_0^2}} \\ &\exp \left[\frac{j2k(x_1 \sin \theta + z_0 \cos \theta)(x_1 \cos \theta - z_0 \sin \theta)^2}{4(x_1 \sin \theta + z_0 \cos \theta)^2 + (k w_0^2)^2} \right] \\ &\exp \left[\frac{-(k w_0 (x_1 \cos \theta - z_0 \sin \theta))^2}{4(x_1 \sin \theta + z_0 \cos \theta)^2 + (k w_0^2)^2} \right] \end{aligned} \quad (2.23)$$

2.4 Technique for Numerical Evaluation of the Coupling Efficiency

At the end surface of the LiNbO_3 waveguide one can clearly express ψ_{inc} as a superposition of all the discrete and continuous modes of the LiNbO_3 waveguide plus the reflected radiation fields. For any end surface that has an effective antireflection coating, the reflected radiation fields were found to be negligible and, from the orthogonality properties of the modes, the coupling efficiency is given by

$$E = \text{coupling efficiency} = \frac{\left| \int_{-\infty}^{+\infty} \psi_{\text{inc}} \psi_1^* dx \right|^2}{\int_{-\infty}^{+\infty} \psi_{\text{inc}} \psi_{\text{inc}}^* dx \int_{-\infty}^{+\infty} \psi_1 \psi_1^* dx} \quad (2.24)$$

In this formation, the coupling efficiency is independent of the normalization constants A and A' in Equations 2.5, 2.18, 2.19 and 2.20. For the first part of the calculation x_1 and x are related to each other by

$$x_1 = x - \Delta. \quad (2.25)$$

For the second part of the calculation ($\theta \neq 0$) x_1 and x' are related to each other by

$$x_1 = x' - \Delta \quad (2.26)$$

where Δ is the displacement of the top surface of the LiNbO_3 waveguide with respect to the center of the active layer for $\theta = 0$ in both cases, as shown in Figure 9 and 10.

The coupling efficiency between the laser diode and the LiNbO_3 waveguide is determined by calculating the overlap integral between the incident field, ψ_{inc} (Equation 2.5 or 2.23), and the guided wave mode (Equations 2.18, 2.19) given by Equation 2.24.

Equation 2.24 was evaluated numerically by Simpsons rule on the IBM 360/2065 computer with $\Delta x = 0.02 \mu\text{m}$. The limits of the integration were truncated at values of x where $\psi_{\text{inc}}(x,z) = \psi_{\text{inc}}(0,z)/e^4$. The Bessel function in Equations 2.18 and 2.19 was usually of fractional order and real argument, and was computed by the series¹¹

$$J_\nu(x) = \sum_{k=0}^{\infty} \frac{(-1)^k}{k! \Gamma(\nu + k + 1)} \left(\frac{x}{2}\right)^{\nu + 2k}$$

where Γ is the gamma function and a double precision procedure was used for the computation. The series was truncated at the k th term when the value of the k th term was less than 10^{-16} . Comparison of the $J_\nu(x)$ evaluated in this manner with the tabulated values indicated that the accuracy was better than 4 significant figures^{12,13}.

2.5 Effects of Transverse Displacement

The coupling efficiency is given in Figures 11 through 19 for the case of perfect angular alignment ($\theta = 0$). Figures 11 through 13 show the coupling efficiency as a function of transverse displacement, Δ , for various x_0 and δ values characterizing the TE_0 mode in the LiNbO_3 waveguide and for $0.5 \mu\text{m}$ separation between the end surfaces of the waveguide and the laser. Figures

COUPLING EFFICIENCY VS Δ (μm) $Z = 0.5 \mu\text{m}$

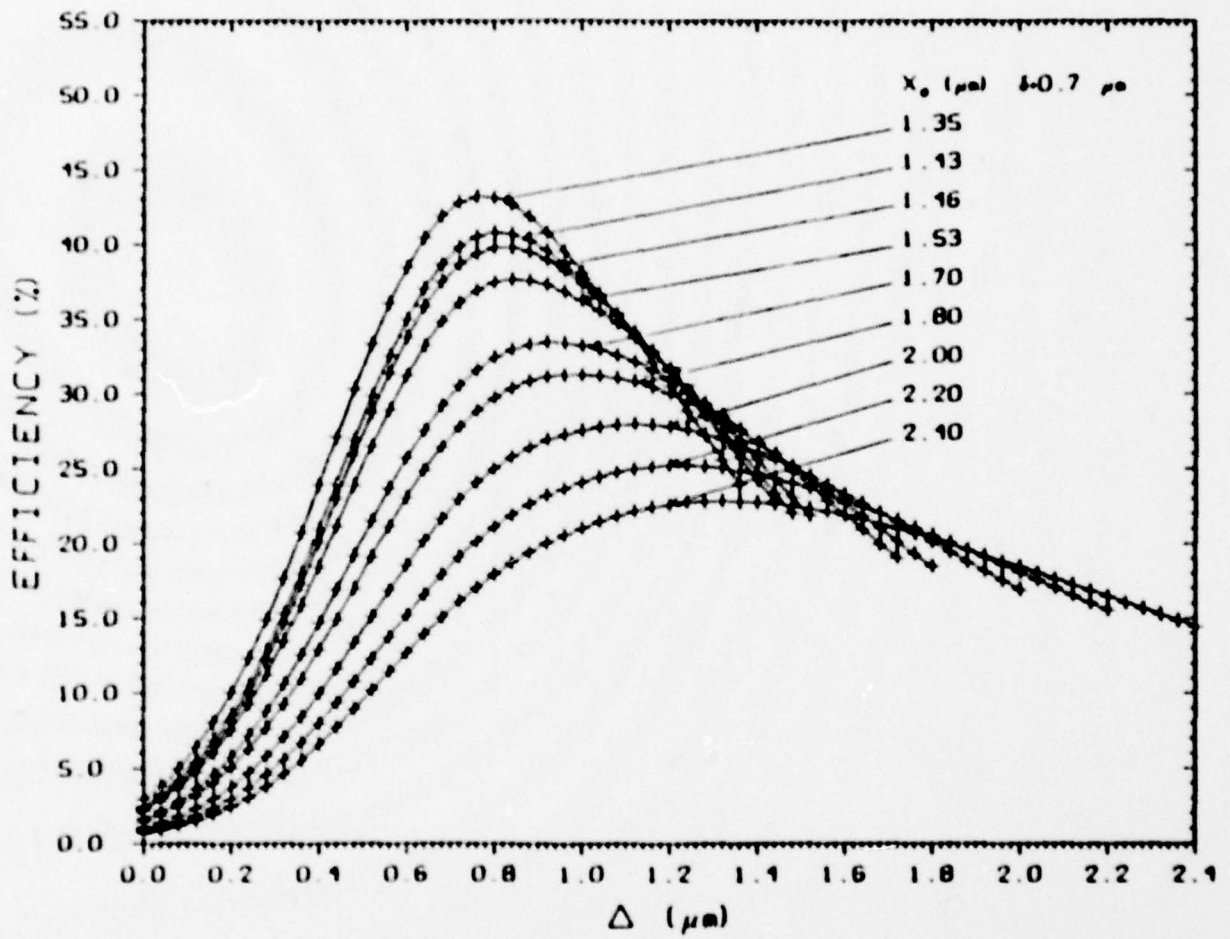


FIGURE 11

COUPLING EFFICIENCY VS Δ (μm) $Z = 0.5 \mu\text{m}$

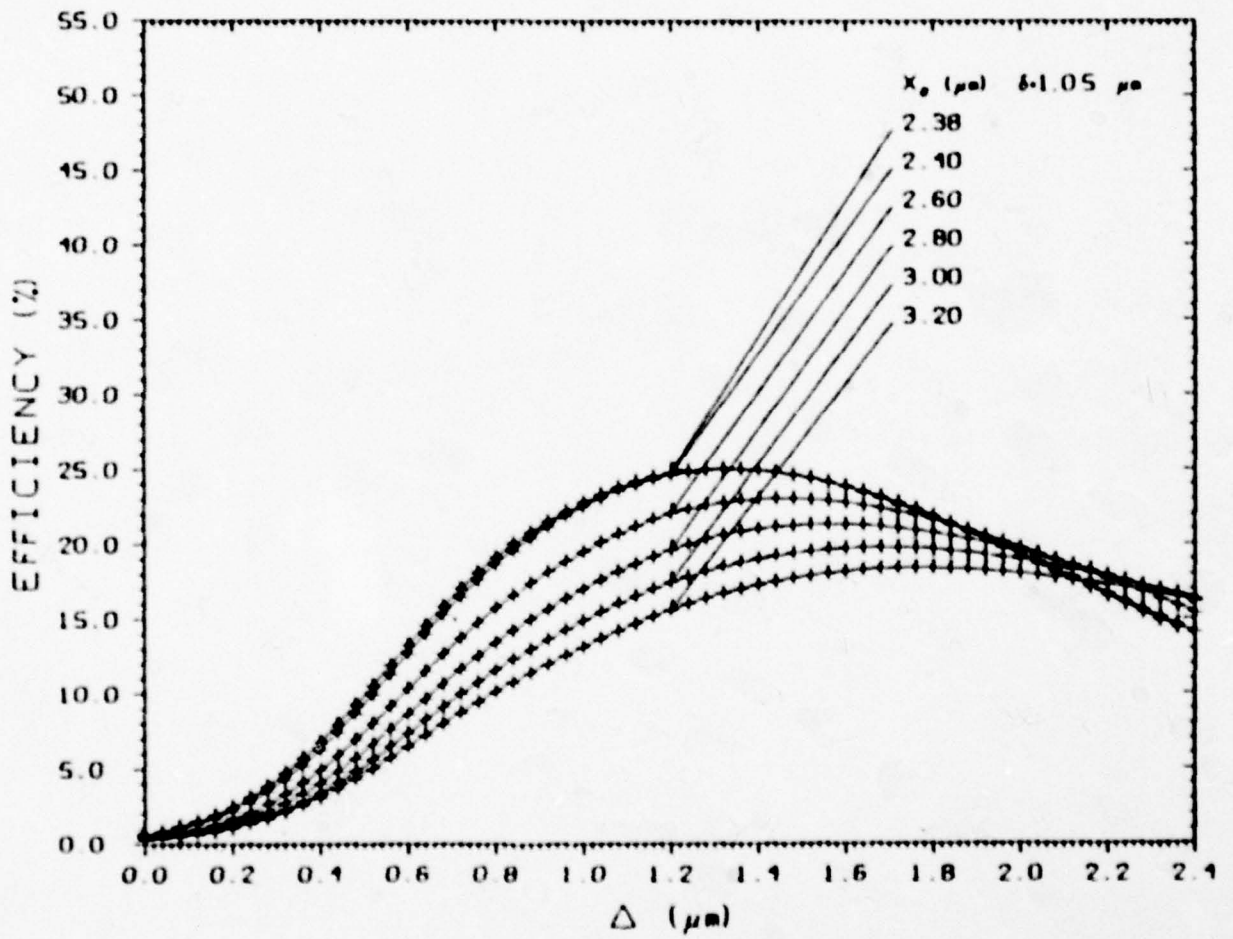


FIGURE 12

COUPLING EFFICIENCY VS Δ (μm) $Z = 0.5 \mu\text{m}$

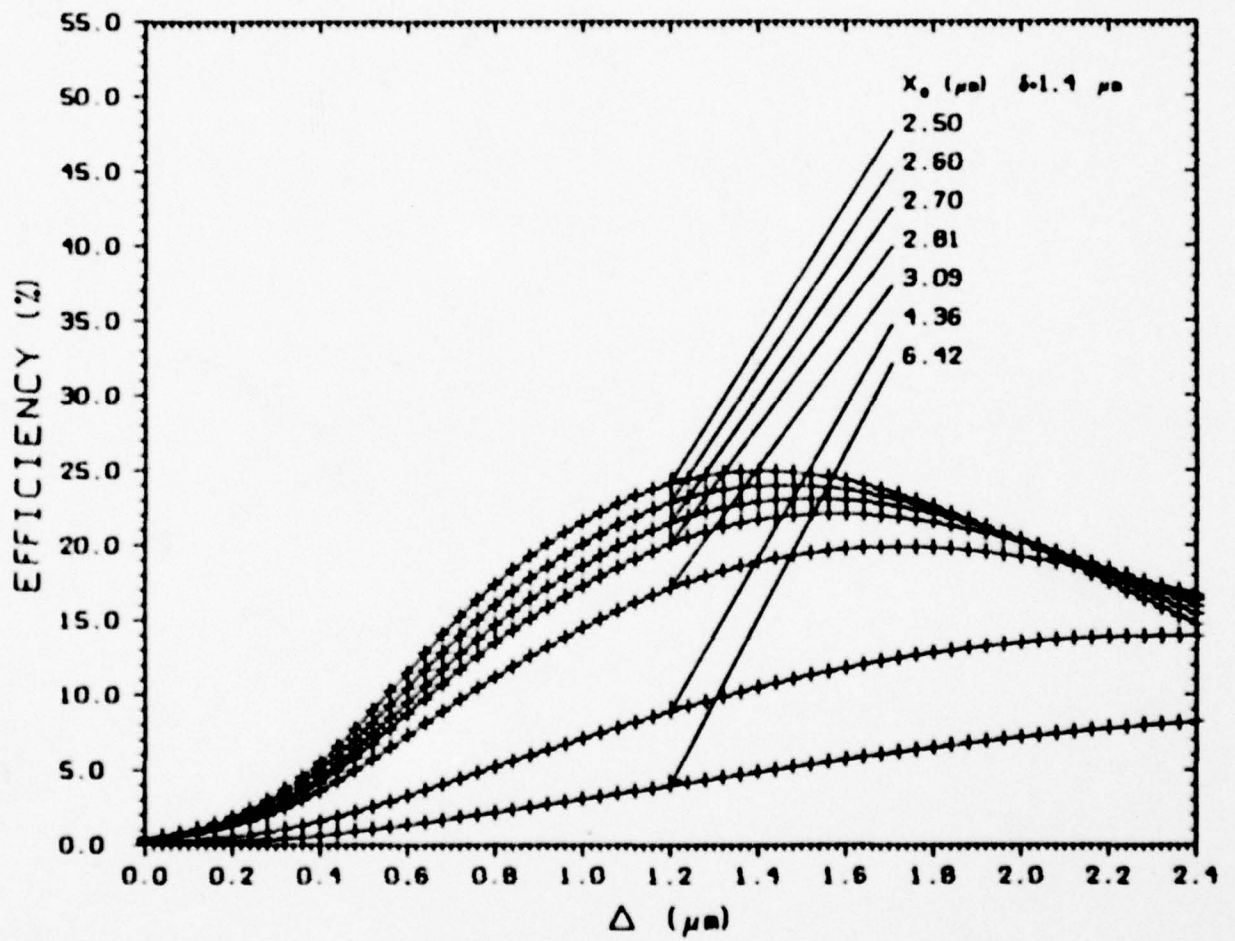


FIGURE 13

14 through 19 show the results of similar calculations for the same x_0 , δ and Δ values obtained at 1.0 μm and 2.0 μm separations.

To illustrate the coupling efficiency that may be obtained in experimentally realizable waveguides, the coupling efficiencies have been evaluated for the δ and Δn (t and τ) values marked by triangles in Figure 20. To show the significance of the mode profile variations, points beyond the "no TiO_2 residue" limit, typically for $\delta = 0.7 \mu\text{m}$, have been included.

Notice that even at $\delta = 0.7 \mu\text{m}$ and $x_0 = 1.35 \mu\text{m}$, corresponding to $\Delta n = 0.05$ and $\delta = 0.7 \mu\text{m}$, the maximum efficiency is 43% for $\Delta = 0.76 \mu\text{m}$. Coupling efficiency of the order of 25% to 30% is obtained in other cases. The coupling efficiency is not very sensitive to errors in transverse displacement alignment. The coupling efficiency also does not degrade rapidly as the longitudinal separation distance is increased as shown in Figure 21.

The general conclusion is that the coupling efficiency is fairly low which is caused by the mismatch between the LiNbO_3 waveguide mode and the incident laser diode radiation field. For the chosen beam waist size, w_0 , the following observations can be made: for $z_0 < 0.01 \mu\text{m}$, the mode depth x_0 is made larger than $w(z)$, the half beam width, and the beam radius of curvature, $R(z)$ is very large. There is a large amplitude mismatch and small phase variations between ψ_{inc} and ψ_1 . For $0.01 \mu\text{m} < z_0 < 2.0 \mu\text{m}$, $x_0 \approx w(z)$ and $R(z) \approx z$ resulting in a close amplitude match and large phase mismatch between ψ_{inc} and ψ_1 . For $z_0 > 2.0 \mu\text{m}$, $x_0 \ll w(z)$ and $R(z)$ is large, resulting in a large amplitude mismatch and small phase variations between ψ_{inc} and ψ_1 . The net effect is a small value for the overlap integral in Equation 2.24 for all values of z_0 .

The incident radiation field was shown to fit a gaussian beam with half beam waist size, $w_0 = 0.2 \mu\text{m}$, in Section 2.1. In general, there are two methods which can be used to determine the parameter, w_0 : (a) to match the gaussian beam field distribution to the E-field of the guided mode at the laser diode end surface and (b) to match the gaussian far field distribution to the calculated far field pattern (40,41) (or the experimentally measured far field intensity profile) to find w_0 .

COUPLING EFFICIENCY VS $\Delta(\mu\text{m})$ $Z = 1.0 \mu\text{m}$

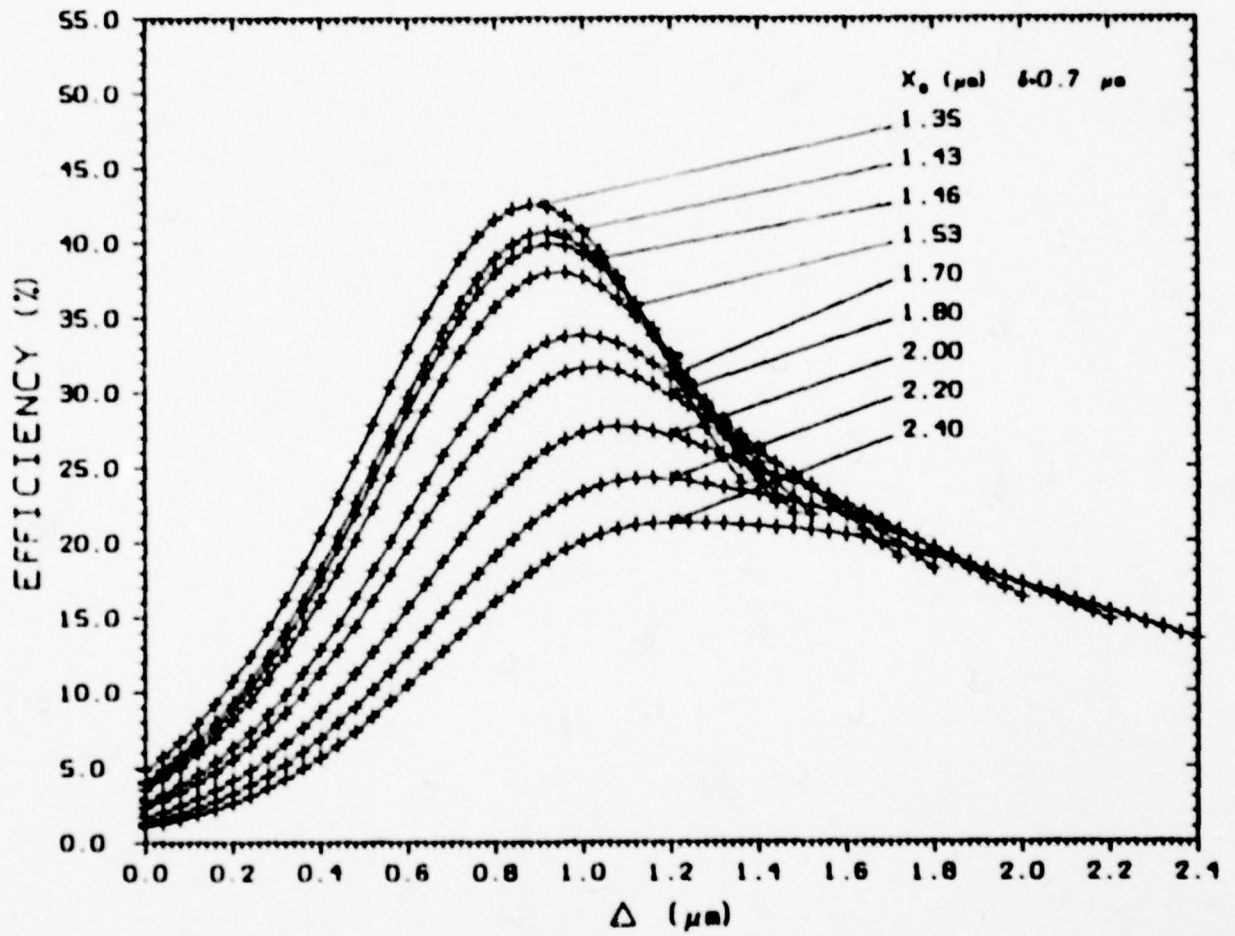


FIGURE 14

COUPLING EFFICIENCY VS $\Delta(\mu\text{m})$ $Z = 1.0\mu\text{m}$

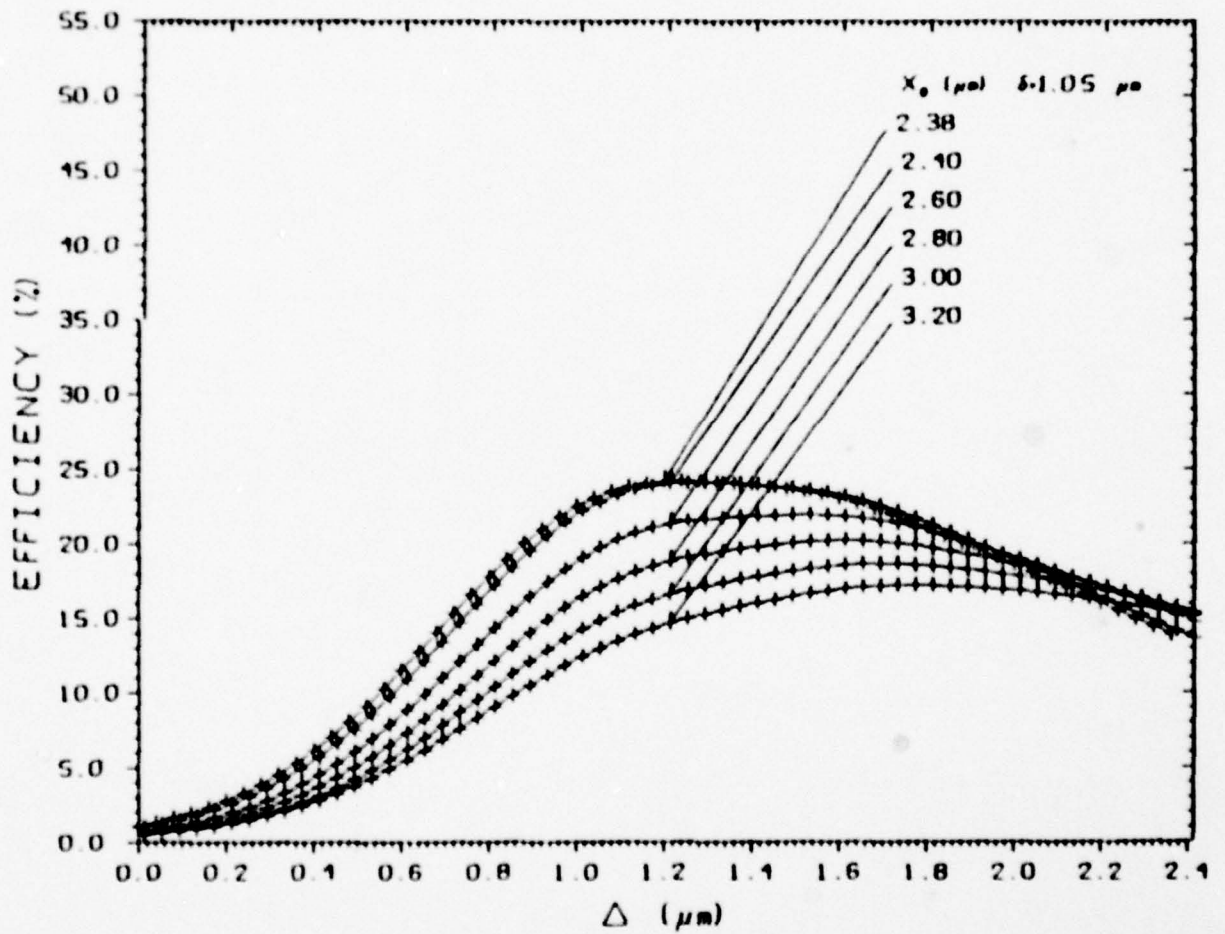


FIGURE 15

COUPLING EFFICIENCY VS $\Delta(\mu\text{m})$ $Z = 1.0 \mu\text{m}$

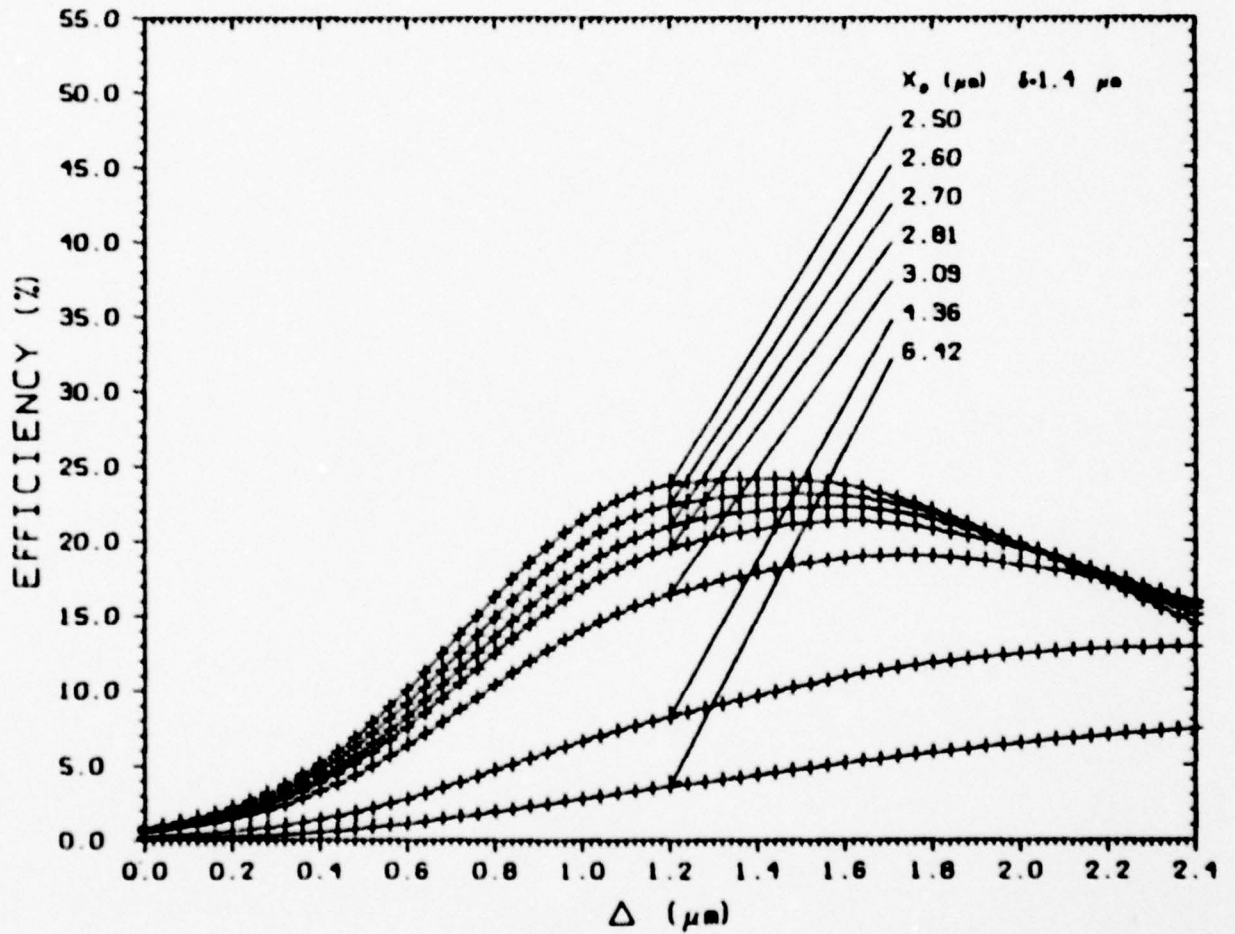


FIGURE 16

COUPLING EFFICIENCY VS $\Delta(\mu\text{m})$ $Z = 2.0\mu\text{m}$

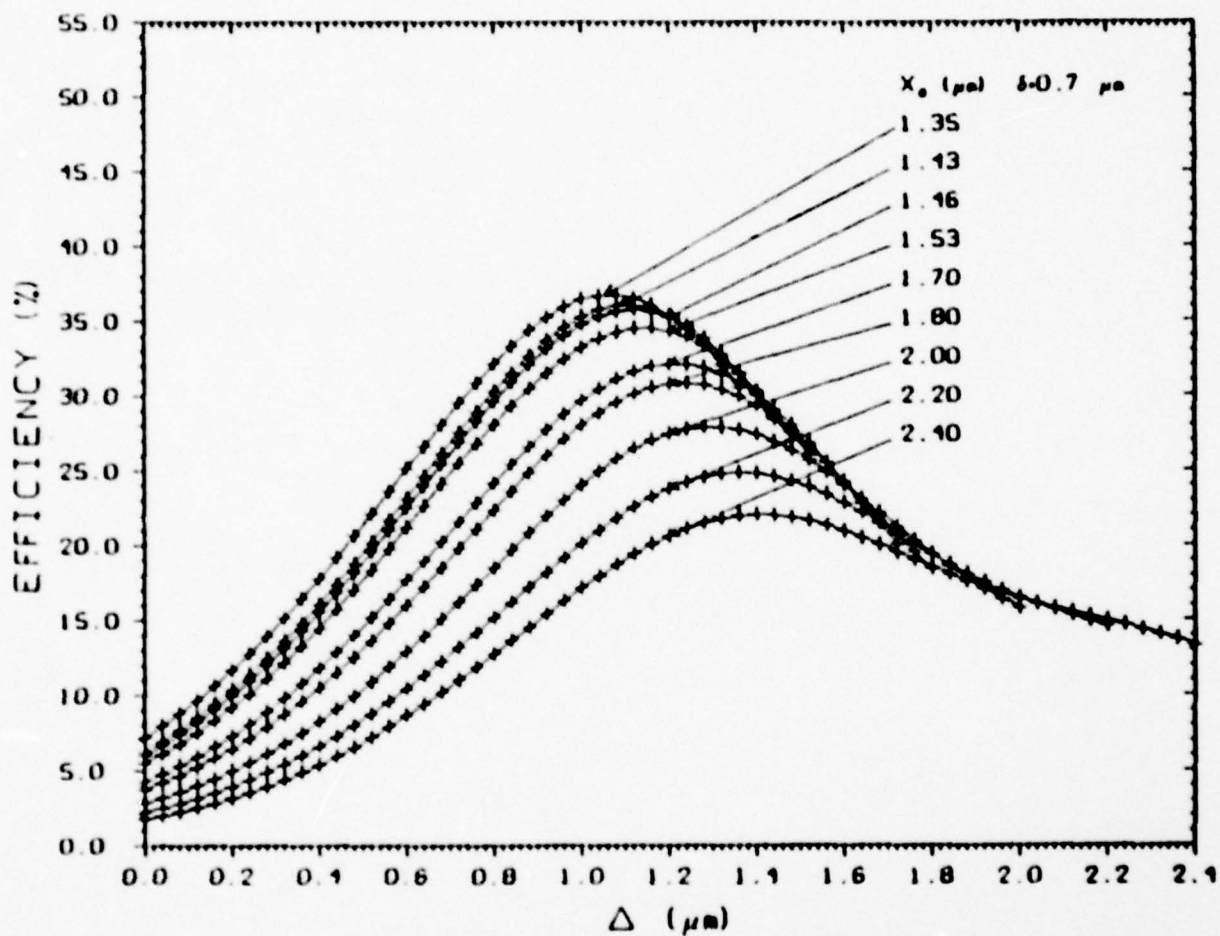


FIGURE 17

COUPLING EFFICIENCY VS Δ (μm) $Z = 2.0\mu\text{m}$

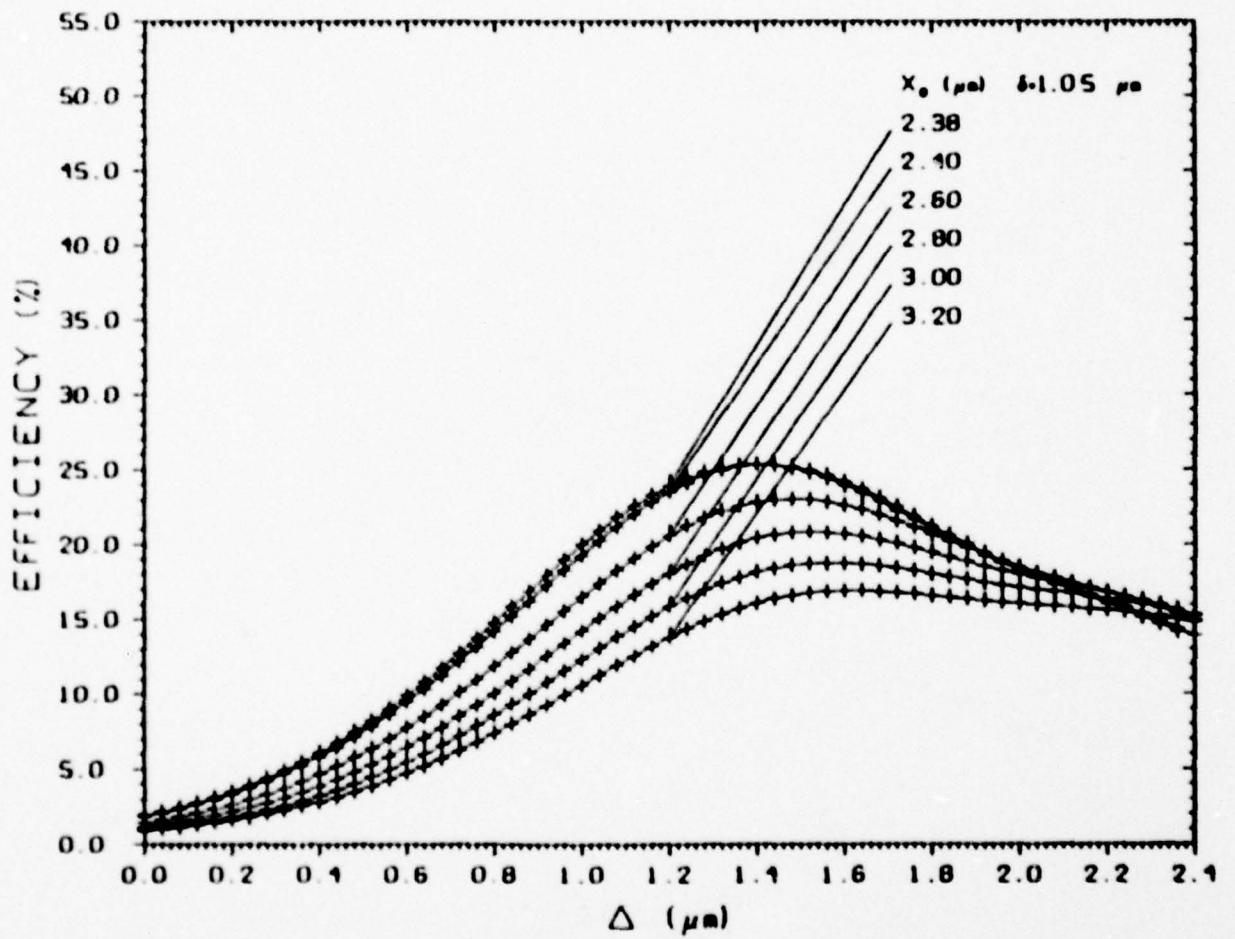


FIGURE 18

COUPLING EFFICIENCY VS $\Delta(\mu\text{m})$ $Z = 2.0\mu\text{m}$

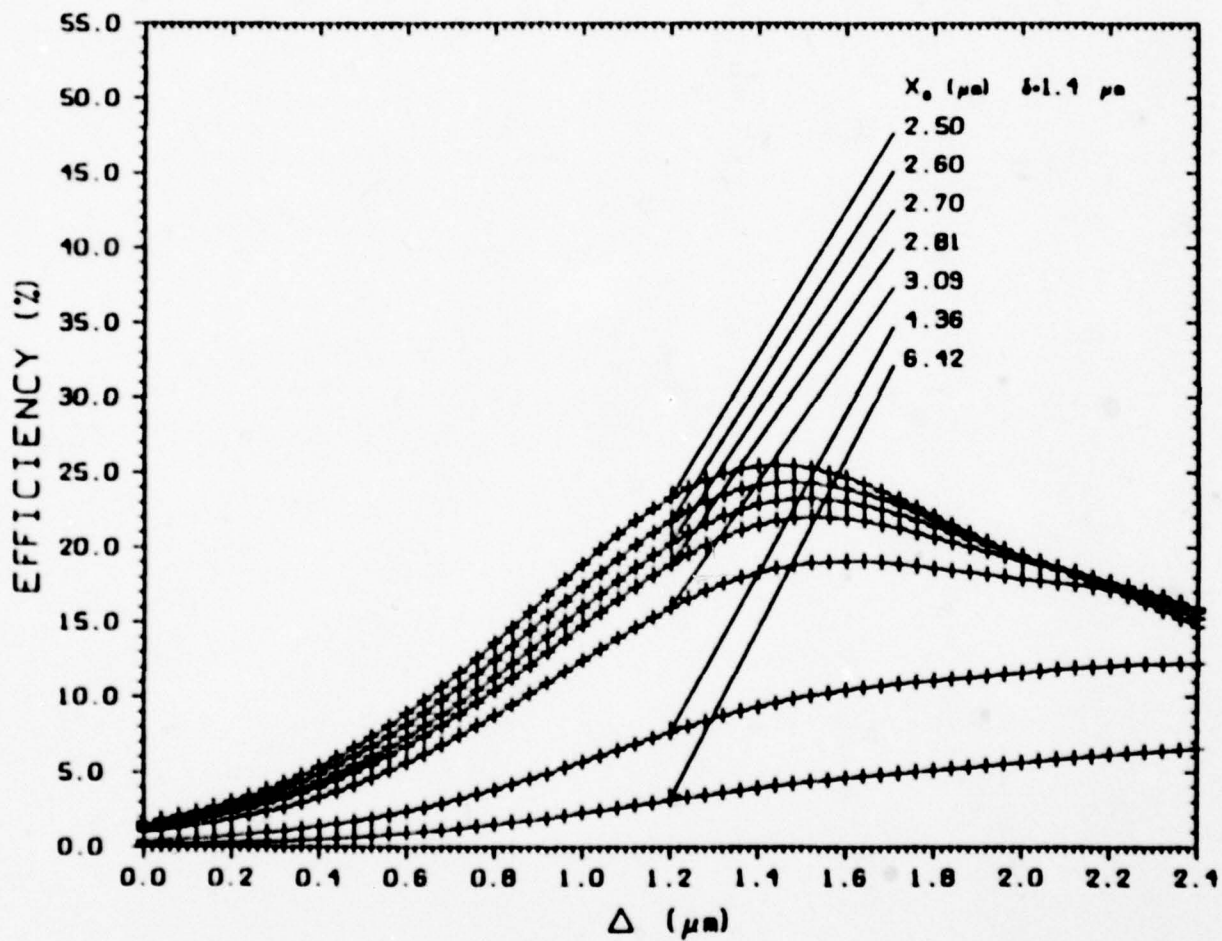


FIGURE 19

**CALCULATED COUPLING EFFICIENCY VALUE
OF MODE DEPTH, x_0 AS A FUNCTION OF δ AND Δn**

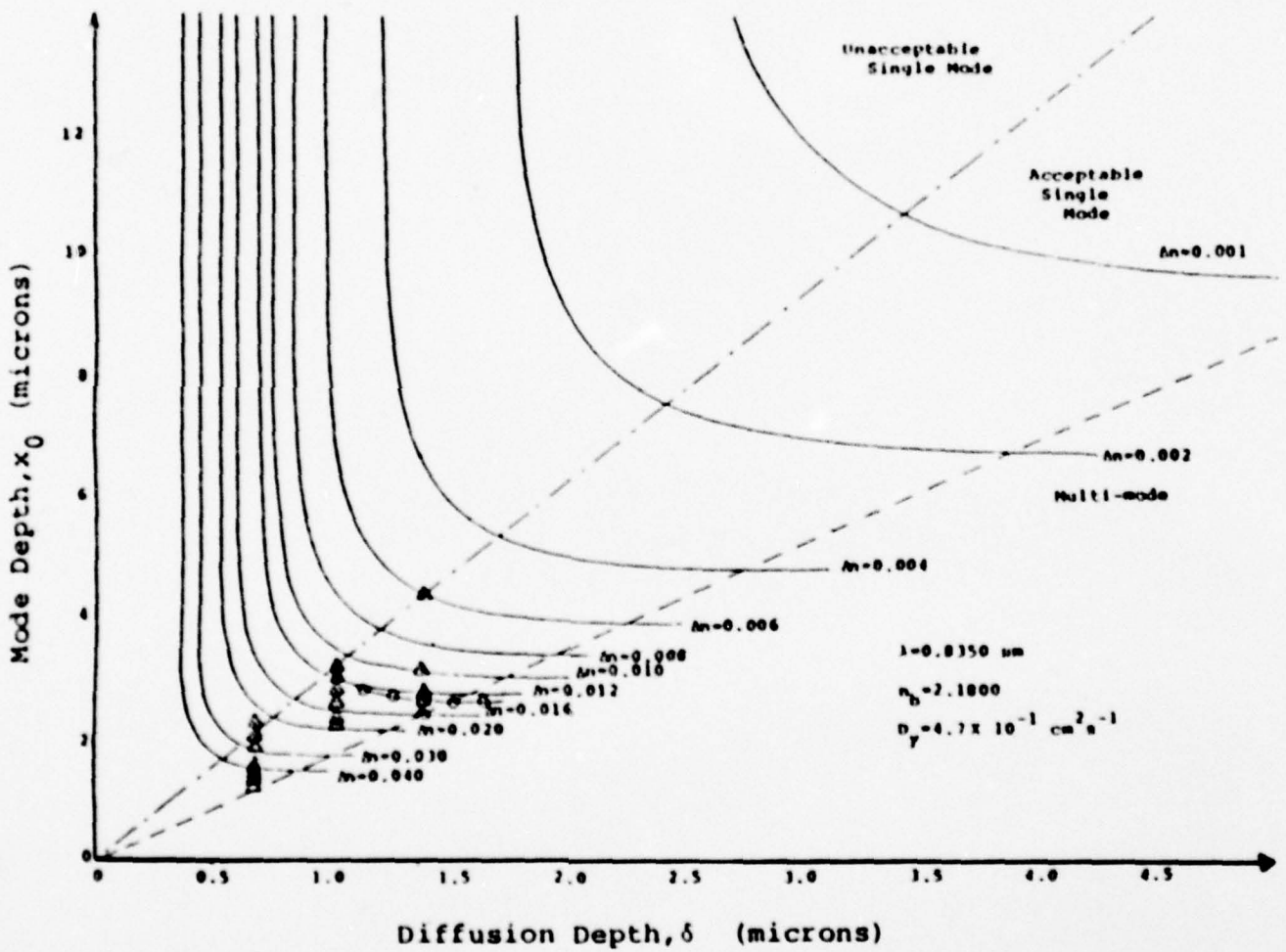


FIGURE 20

MAXIMUM CALCULATED COUPLING EFFICIENCY
AS A FUNCTION OF LOGITUDINAL SEPARATION, Z_0

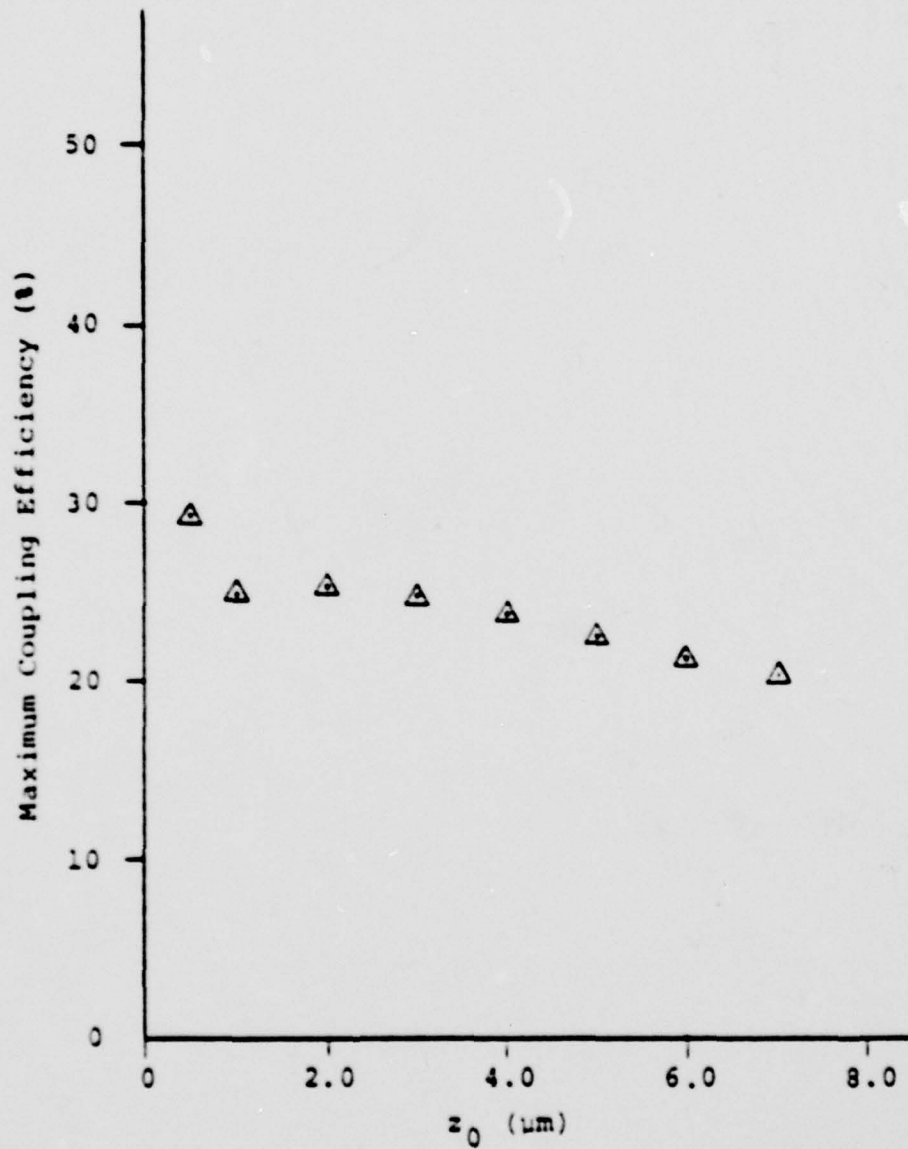


FIGURE 21

In the present analysis, w_0 has been chosen according to method (a). For coupling efficiency calculations the radiation field distribution in the near field may be needed. Therefore, matching the gaussian beam to the oscillating mode profile at the laser end surface may provide a more accurate representation of the near field radiation pattern. Botez has done a similar calculation to match a gaussian distribution to the oscillating mode profile for slightly different parameters¹⁶. For an active region thickness $d = 0.288 \mu\text{m}$, $\lambda = 0.9 \mu\text{m}$, $n_1 = 3.6$ and $\Delta n = 0.14$. Equation 15 and Figure 3 (d) in Reference 14 yields $w_0 = 0.32 \mu\text{m}$.

In order to match the far field patterns, the beam divergence of a gaussian beam is determined according to

$$\theta = \tan^{-1} \left(\frac{\lambda}{\pi w_0} \right), \quad (2.28)$$

where θ is the 1/e point of the far field distribution (i.e., the half beam width). Butler et al¹⁵ have defined θ_{\perp} as the angle subtended between the half intensity points of the far field intensity distribution in the plane perpendicular to the junction plane.

Following Botez et al¹⁶:

$$\theta_{\perp} = 2 \tan^{-1} \left(\frac{\lambda \sqrt{(n_1 n_2)/2}}{\pi w_0} \right), \quad (2.29)$$

we obtain for w_0

$$w_0 = \frac{\lambda \sqrt{(n_1 n_2)/2}}{\pi \tan \left\{ \frac{\theta_{\perp}}{2} \right\}}. \quad (2.30)$$

Butler et al¹⁵ have calculated the far field intensity profile. Figure 10 of Reference¹⁵ shows θ_{\perp} as a function of the effective guide width $0.9 \cdot d/\lambda_0$ for index differences between the active layer and surrounding layers, $\Delta n = 0.06$ to 0.22. Using the physical data of active layer thicknesses and index difference

given for the MDAC-STL laser (i.e., $2d = 0.2 \mu\text{m}$, $\lambda = 0.8350 \mu\text{m}$, $n_1 = 3.635$ and $\Delta n = 0.14$) and the θ_{\perp} given in Figure 10 of Reference 15, we find $w_0 = 0.45 \mu\text{m}$. If the θ_{\perp} value experimentally measured by MDAC-STL in the far field is matched to the beam divergence of a gaussian beam, a w_0 value ranging from $0.48 \mu\text{m}$ to $0.51 \mu\text{m}$ is obtained.

The variation between the value of $w_0 = 0.20396 \mu\text{m}$ determined by method (a) in Section 2.1 and the w_0 values from the far field calculations and experimental measurements of the intensity profile indicate that the coupling efficiency should be examined for $w_0 = 0.45 \mu\text{m}$. Therefore, the coupling efficiency as a function of displacement Δ is presented again in Figures 22 to 30 for $z_0 = 0.5 \mu\text{m}$, $1 \mu\text{m}$, and $2 \mu\text{m}$ for $\delta = 0.7, 1.06$ and $1.4 \mu\text{m}$ at various mode depths x_0 . Clearly an increase in coupling efficiency by a factor of two can be obtained at $w_0 = 0.45 \mu\text{m}$ as compared to $w_0 = 0.2 \mu\text{m}$.

COUPLING EFFICIENCY VS $\Delta(\mu\text{m})$ $Z = 0.5 \mu\text{m}$

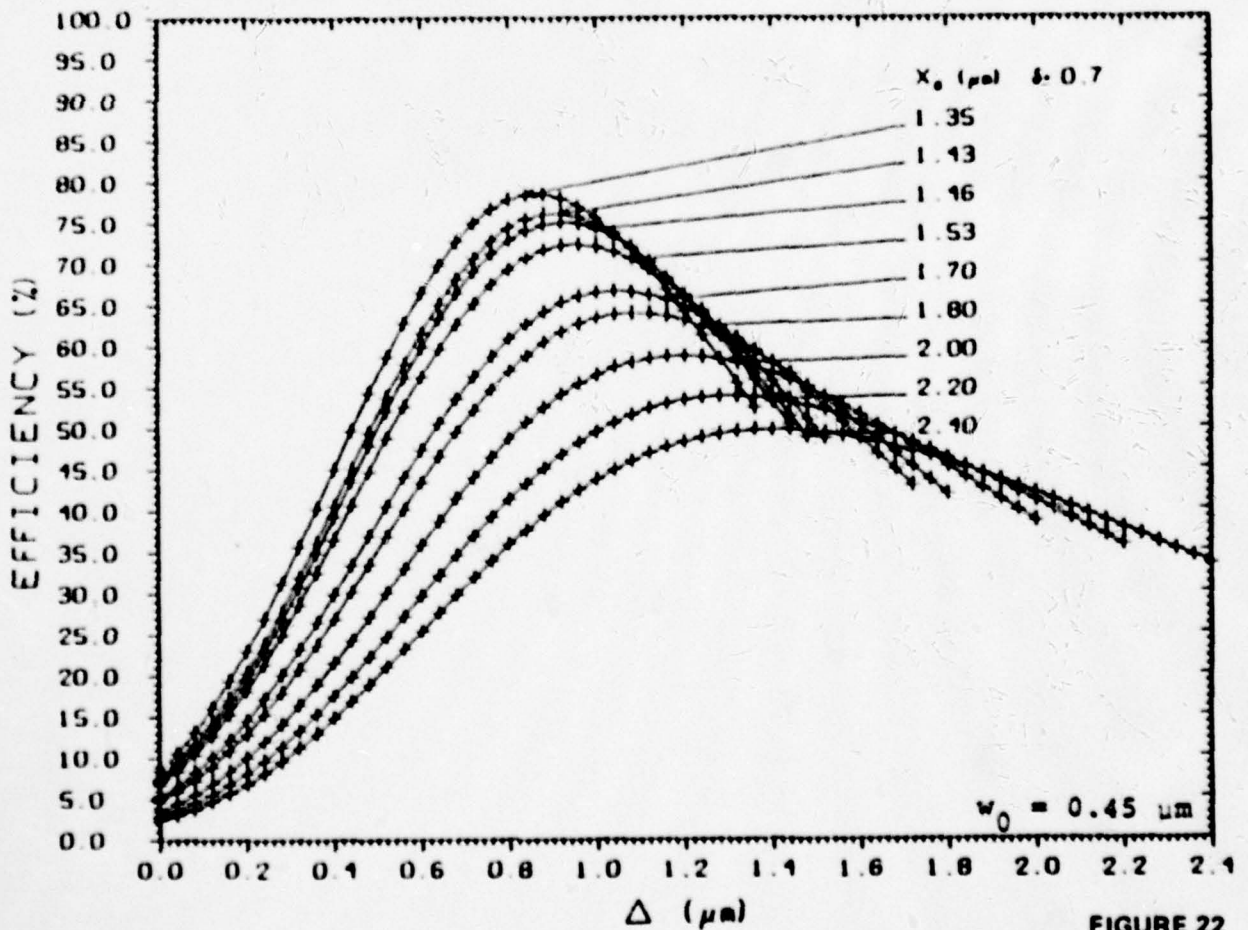


FIGURE 22

COUPLING EFFICIENCY VS $\Delta(\mu\text{m})$ $Z = 0.5\mu\text{m}$

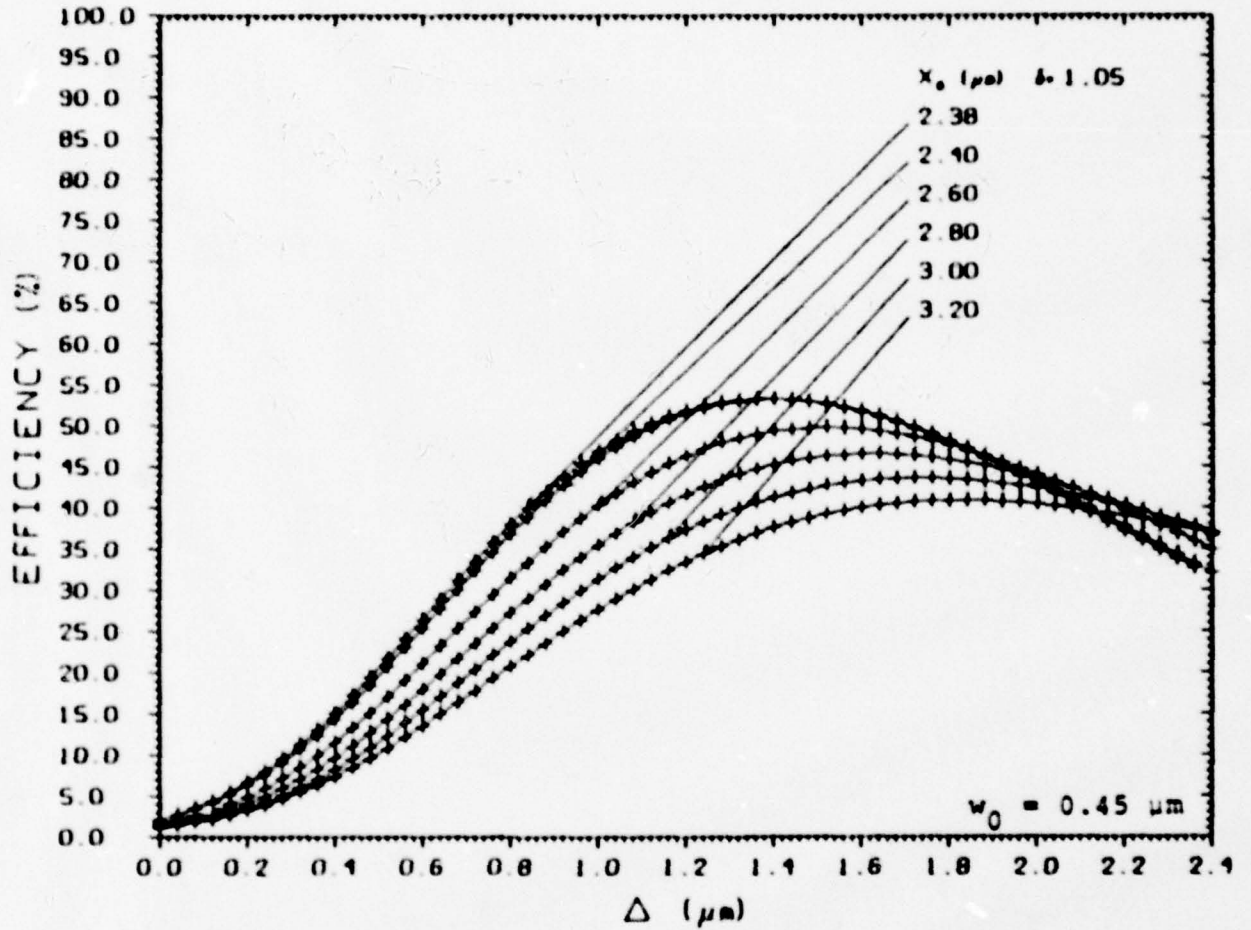


FIGURE 23

COUPLING EFFICIENCY VS $\Delta(\mu\text{m})$ $Z = 0.5 \mu\text{m}$

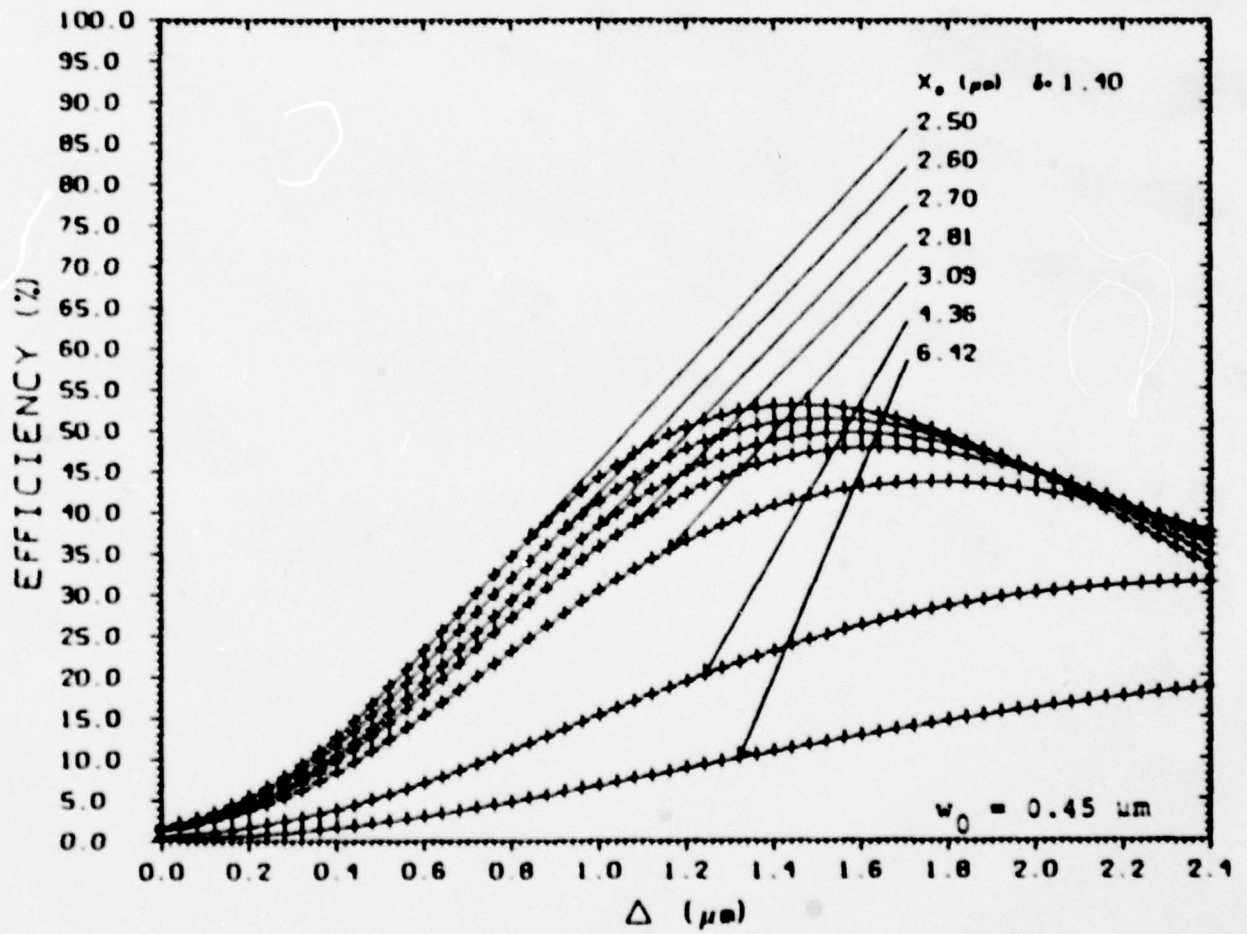


FIGURE 24

COUPLING EFFICIENCY VS Δ (μm) $Z = 1.0 \mu\text{m}$

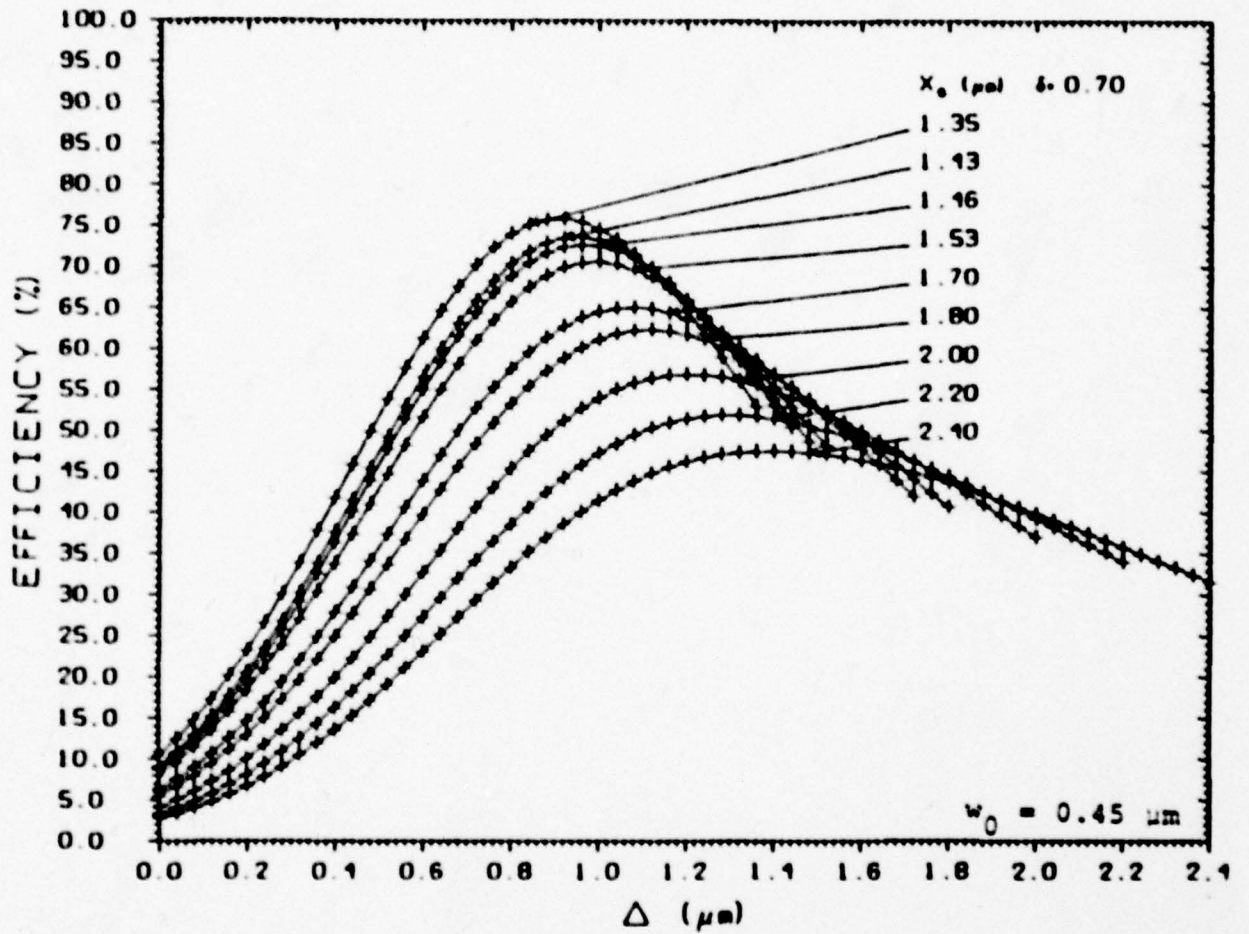


FIGURE 25

COUPLING EFFICIENCY VS Δ (μm) $Z = 1.0\mu\text{m}$

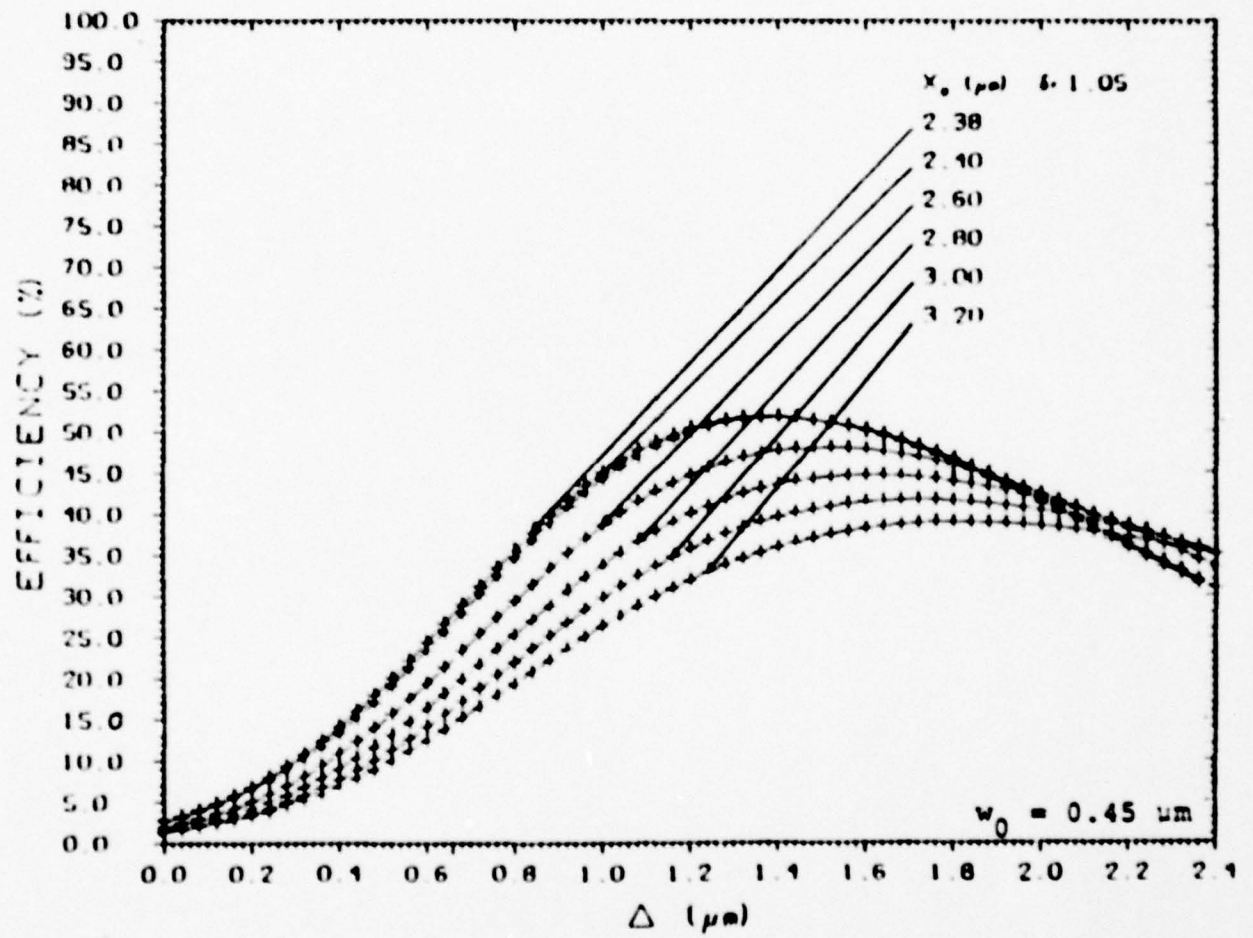


FIGURE 26

COUPLING EFFICIENCY VS Δ (μm) $Z = 1.0\mu\text{m}$

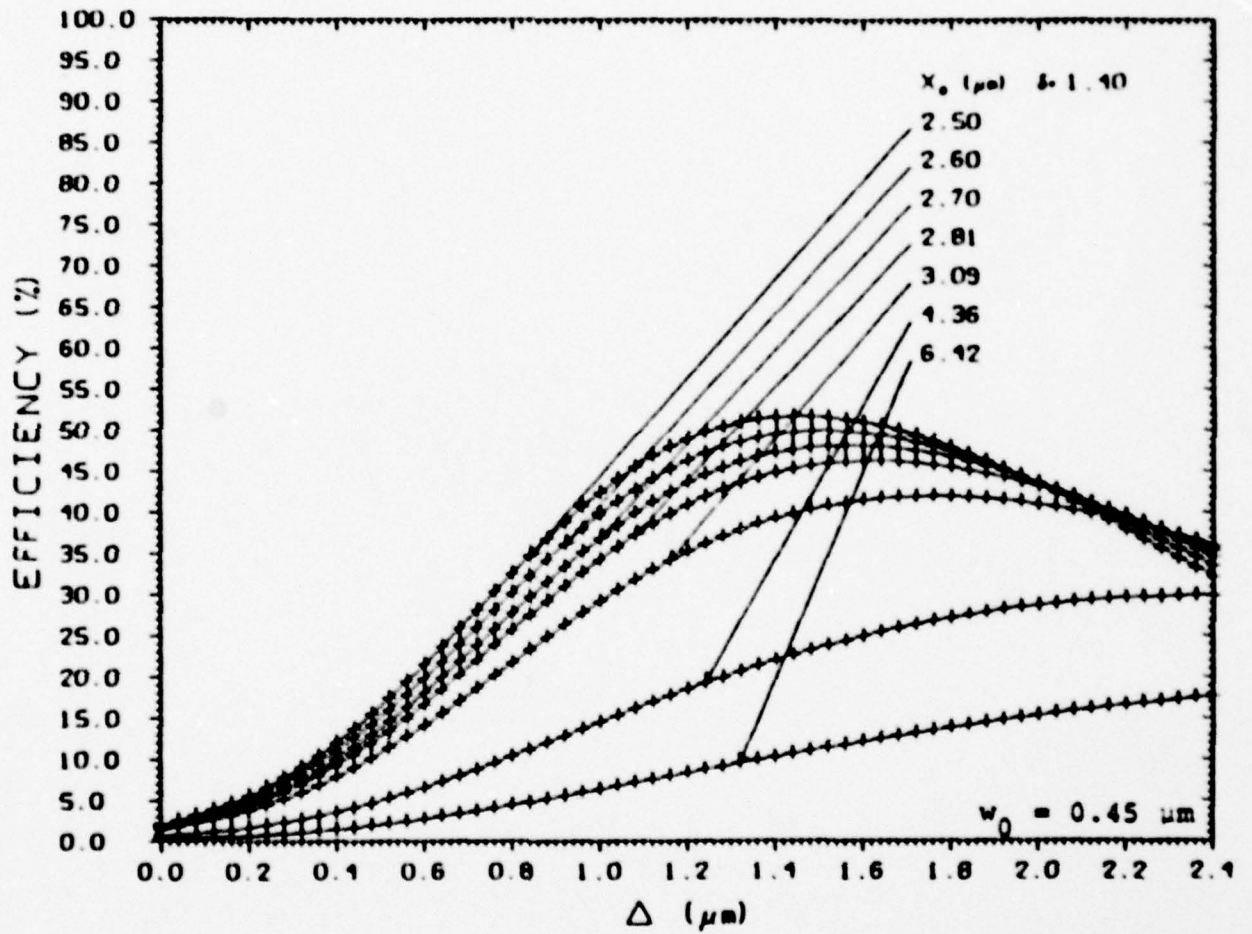


FIGURE 27

COUPLING EFFICIENCY VS $\Delta(\mu\text{m})$ $Z = 2.0\mu\text{m}$

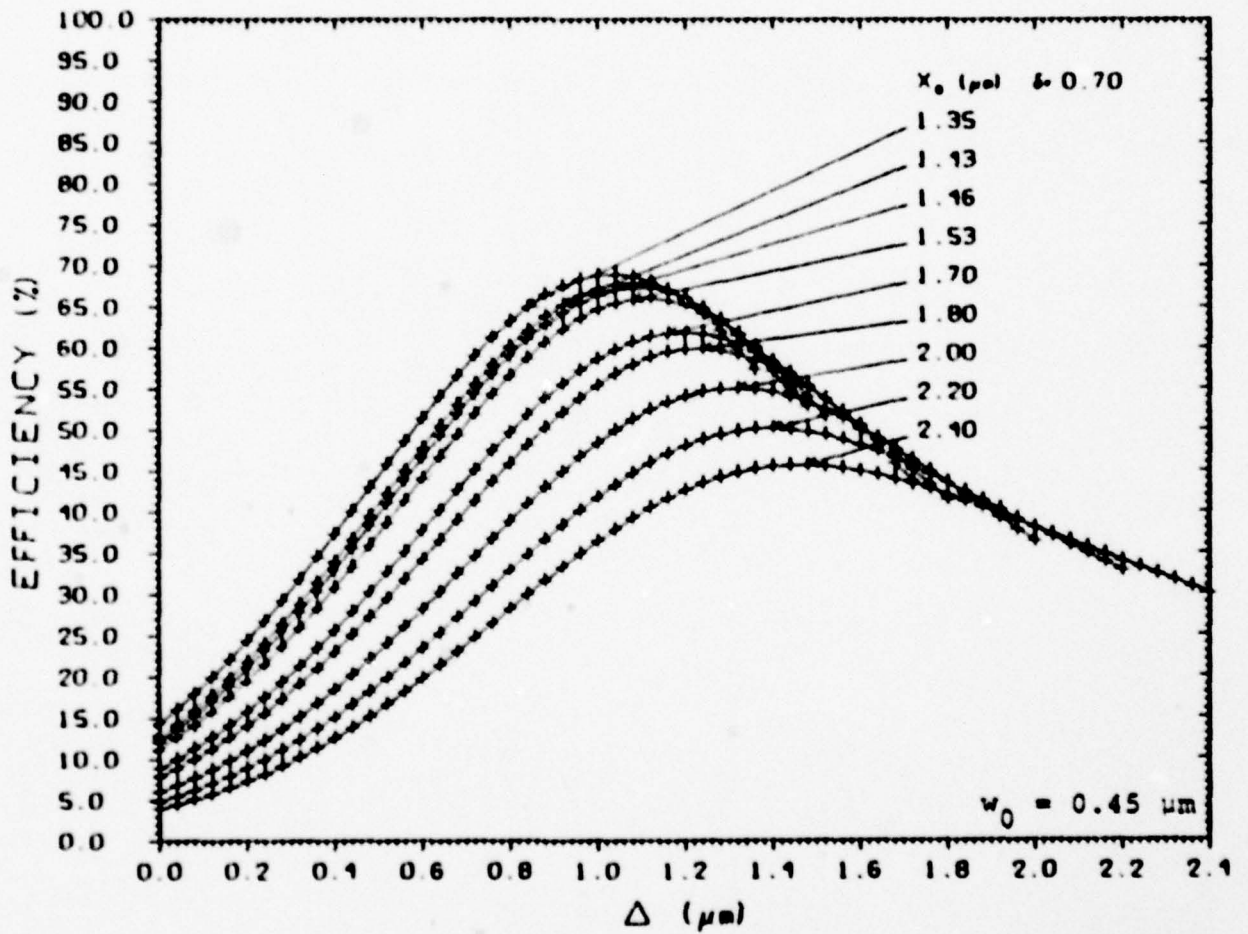


FIGURE 28

COUPLING EFFICIENCY VS $\Delta(\mu\text{m})$ $Z = 2.0\mu\text{m}$

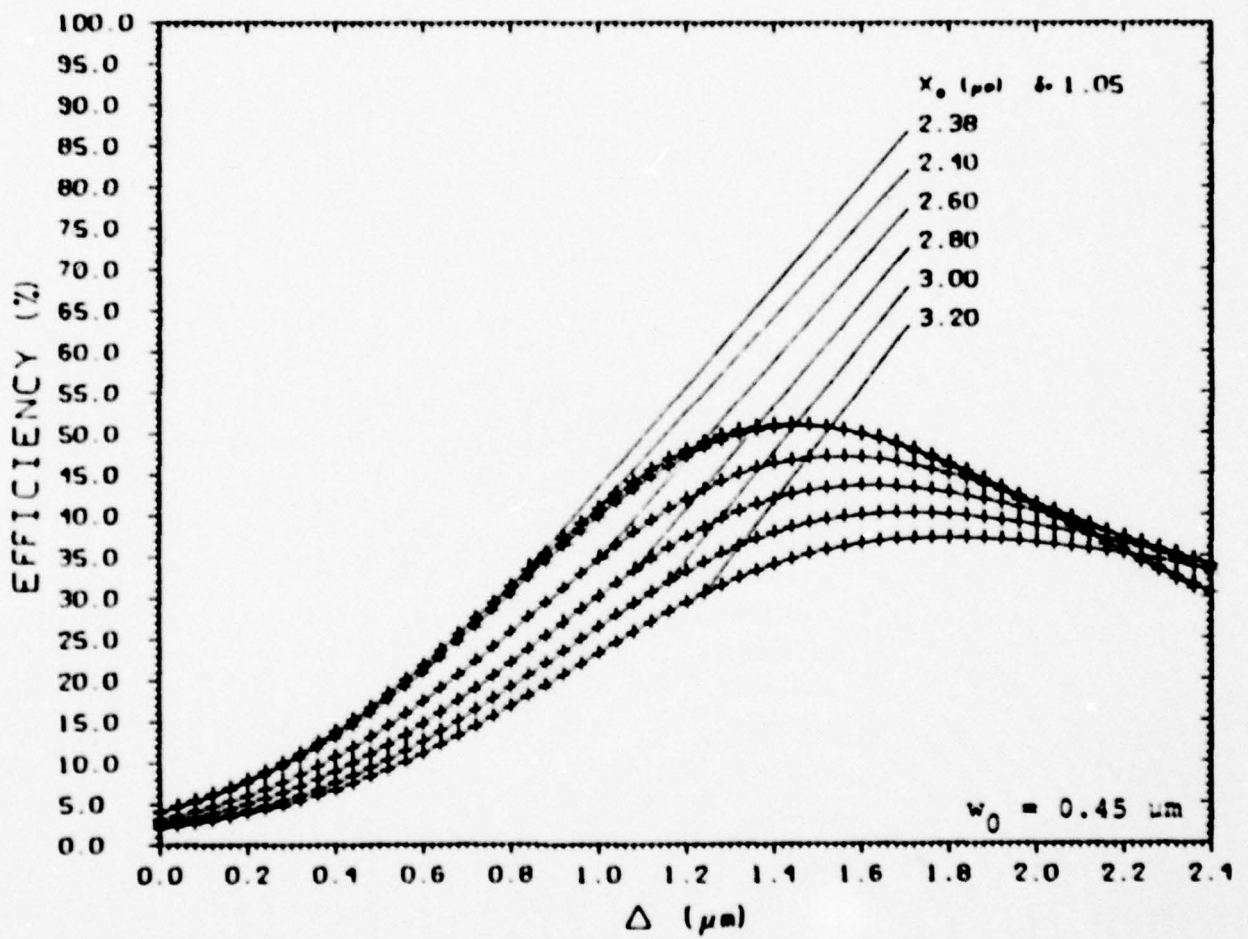


FIGURE 29

COUPLING EFFICIENCY VS $\Delta(\mu\text{m})$ $Z = 2.0\mu\text{m}$

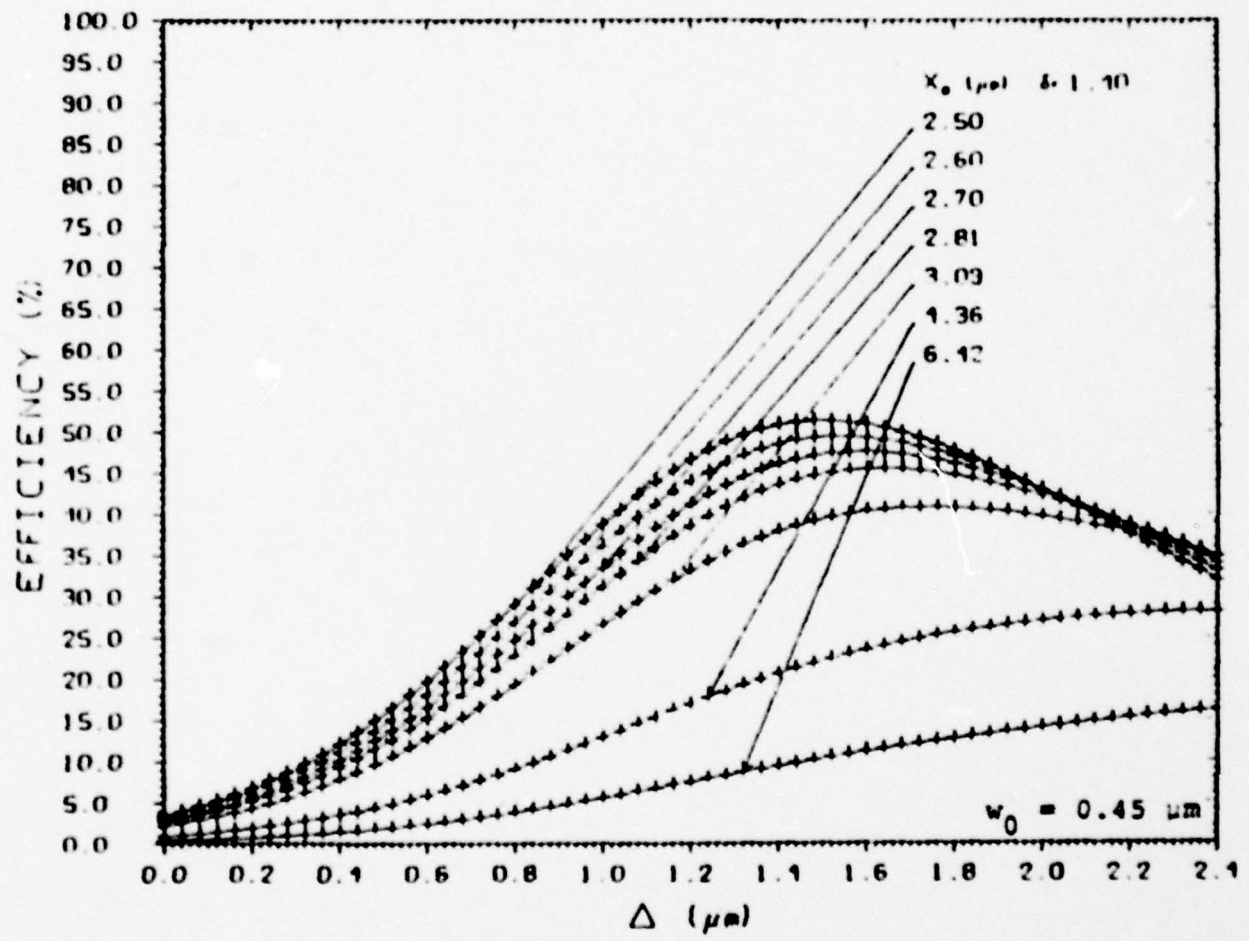


FIGURE 30

2.6 Effects of Angular Alignment

The coupling efficiency between the laser diode and the waveguide for $\theta = 0$ is determined by calculating the overlap integral between the incident electric field, ψ_{inc} , as given by Equation 2.23 and the guided wave mode. A small mode depth, $x_0 = 2.38 \mu\text{m}$ and $\delta = 1.06 \mu\text{m}$, is chosen as close to the "no TiO_2 residue" limit as experimental fabrication will allow. The results are shown in Figures 31 and 32 for $z_0 = 0.5 \mu\text{m}$ and $1.0 \mu\text{m}$, respectively as a function of θ ($-15^\circ \leq \theta \leq +15^\circ$) and Δ ($0 \leq \Delta \leq 2.4 \mu\text{m}$).

**COUPLING EFFICIENCY VS $\Delta(\mu\text{m})$ $Z = 0.5 \mu\text{m}$
AS A FUNCTION OF θ (DEG)**

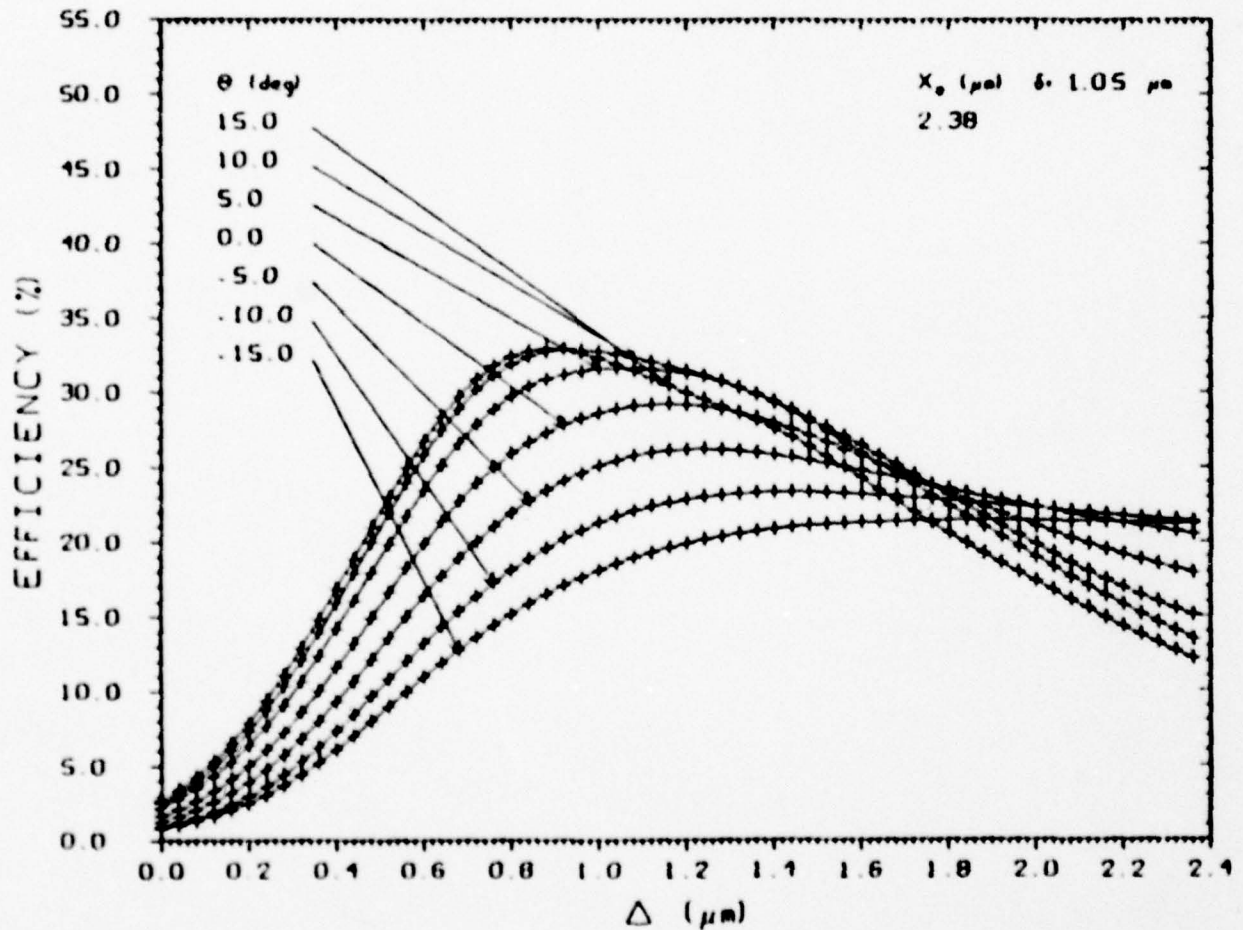


FIGURE 31

**COUPLING EFFICIENCY VS $\Delta(\mu\text{m})$ $Z = 1.0 \mu\text{m}$
AS A FUNCTION OF θ (DEG)**

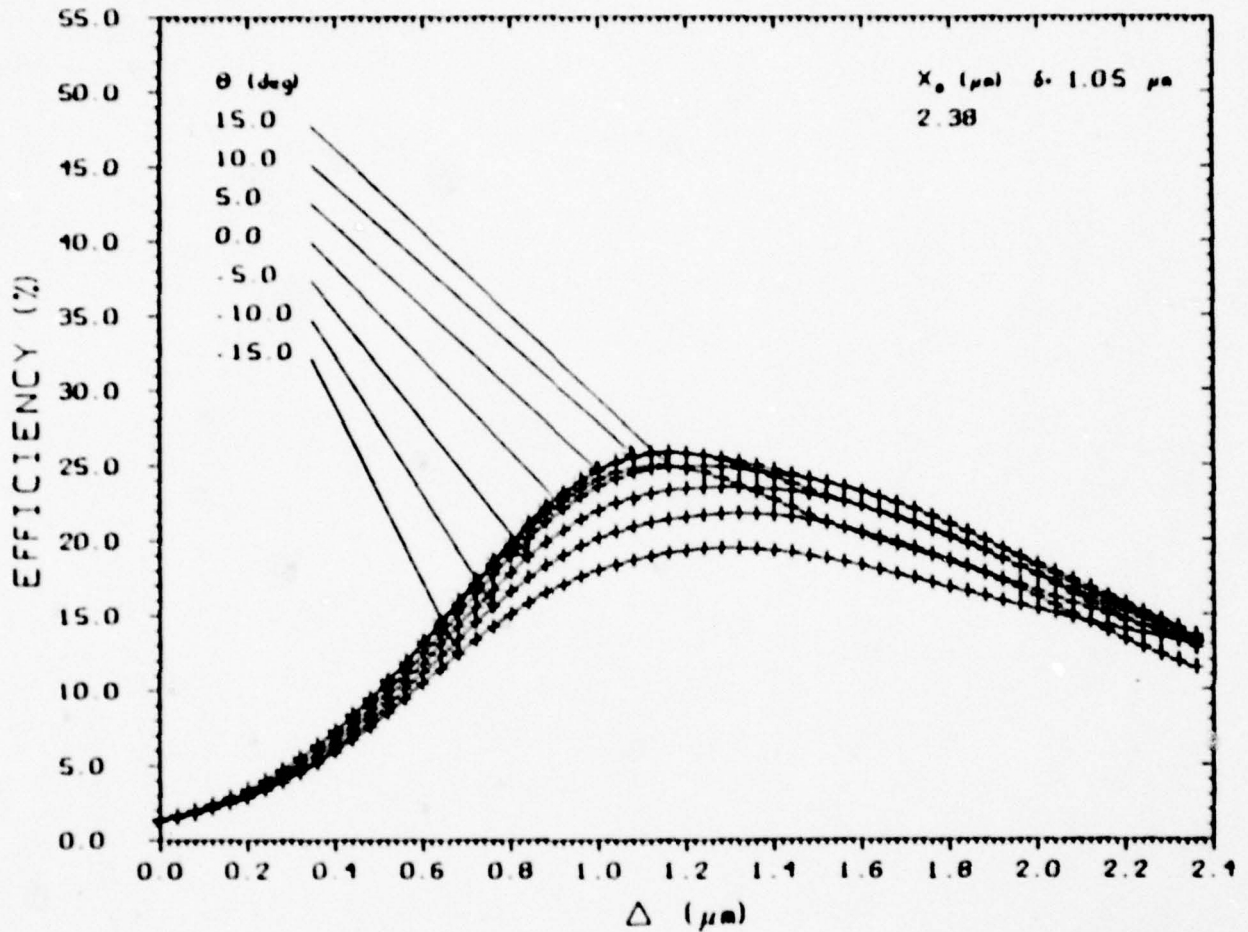


FIGURE 32

At positive values of θ , the incident electric field amplitude decays slower in the negative x' direction than in the positive x' direction. Such a field matches the amplitude variation of the guided wave mode somewhat better. However, the radius of curvature R of the wavefront (i.e., the constant phase surface) of the incident gaussian beam is also a function of the distance of propagation away from the laser end surface. Figure 33 illustrates the variation of R as a function of z for the gaussian beam in our calculation. At $z_0 = 0.5 \mu\text{m}$ the phase of the incident field for $x < 0$ varies more rapidly across the waveguide edge at larger positive angle of θ , and the phase variation tends to reduce the value of the overlap integral. The opposite effect occurred for negative values of θ . Thus, the net effect of these two compensating factors, i.e., the amplitude and phase

BEAM RADIUS OF CURVATURE, $R(z)$, $w_0 = 0.20396 \mu\text{m}$

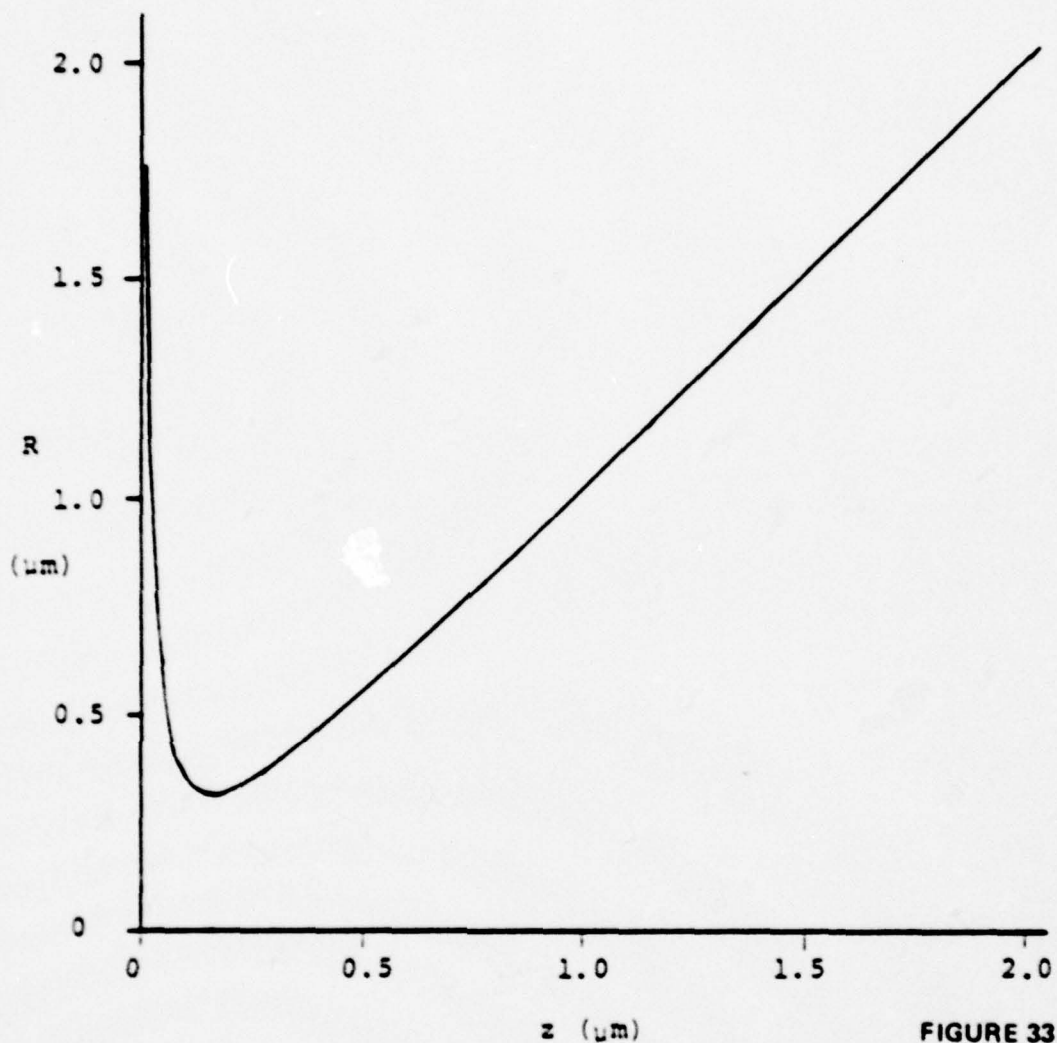


FIGURE 33

variations, is that the coupling efficiency is not very sensitive to angular misalignment and that a slightly higher efficiency is achieved at $\theta = 10^\circ$ than at $\theta = 0^\circ$.

2.7 Comparison with Error Function Complement Diffusion Profile

The possible errors that can be produced by using the assumption of an exponential diffusion profile have been examined. In an unpublished work, Hocker¹⁷ has given a computer calculated electric field pattern of the TE_0 mode for $V = 9.80$ and $b = 0.469$ in an error function diffusion profile. Using the same V value it was found that $b = 0.56079$ for the equivalent mode in the exponential diffusion profile. Figure 34 shows a comparison of the field

MODE PROFILE COMPARISON

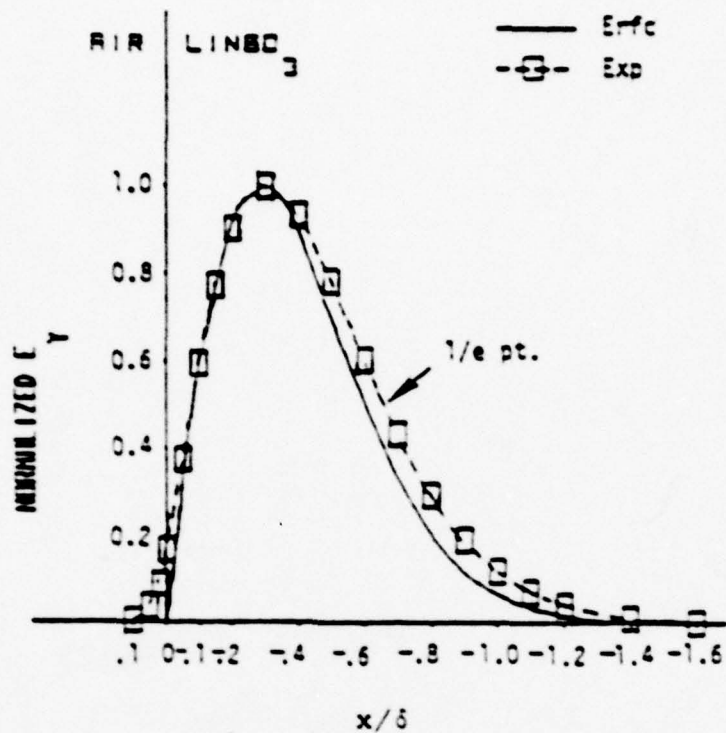


FIGURE 34

patterns in the two cases. Figure 35 shows the calculated efficiency as a function of displacement for a mode with an exponential diffusion profile with $\Delta n = 0.09518$ and $\delta = 2.0 \mu\text{m}$ and an error function complement diffusion profile. Notice the close agreement that exists between the two cases. Therefore, it is unlikely that the use of an exponential diffusion profile is an important source of error in the calculation of coupling efficiency.

2.8 Coupling Calculation - Gaussian Approximation

To complement the calculation performed at Washington University and described in Section 2.4 of this report, a second calculation was performed by MDAC-STL. This calculation took a simplified approach in which the waveguide mode and the laser mode were both approximated by Gaussians. While such a model cannot be expected to predict all features of a coupling experiment, it does provide a closed form result for the coupling efficiency as a function of both longitudinal and transverse misalignments. The closed form result can then be used to check the gross features of the exact numerical calculation of the previous section.

COUPLING EFFICIENCY VS $\Delta(\mu\text{m})$ $Z = 2.0 \mu\text{m}$

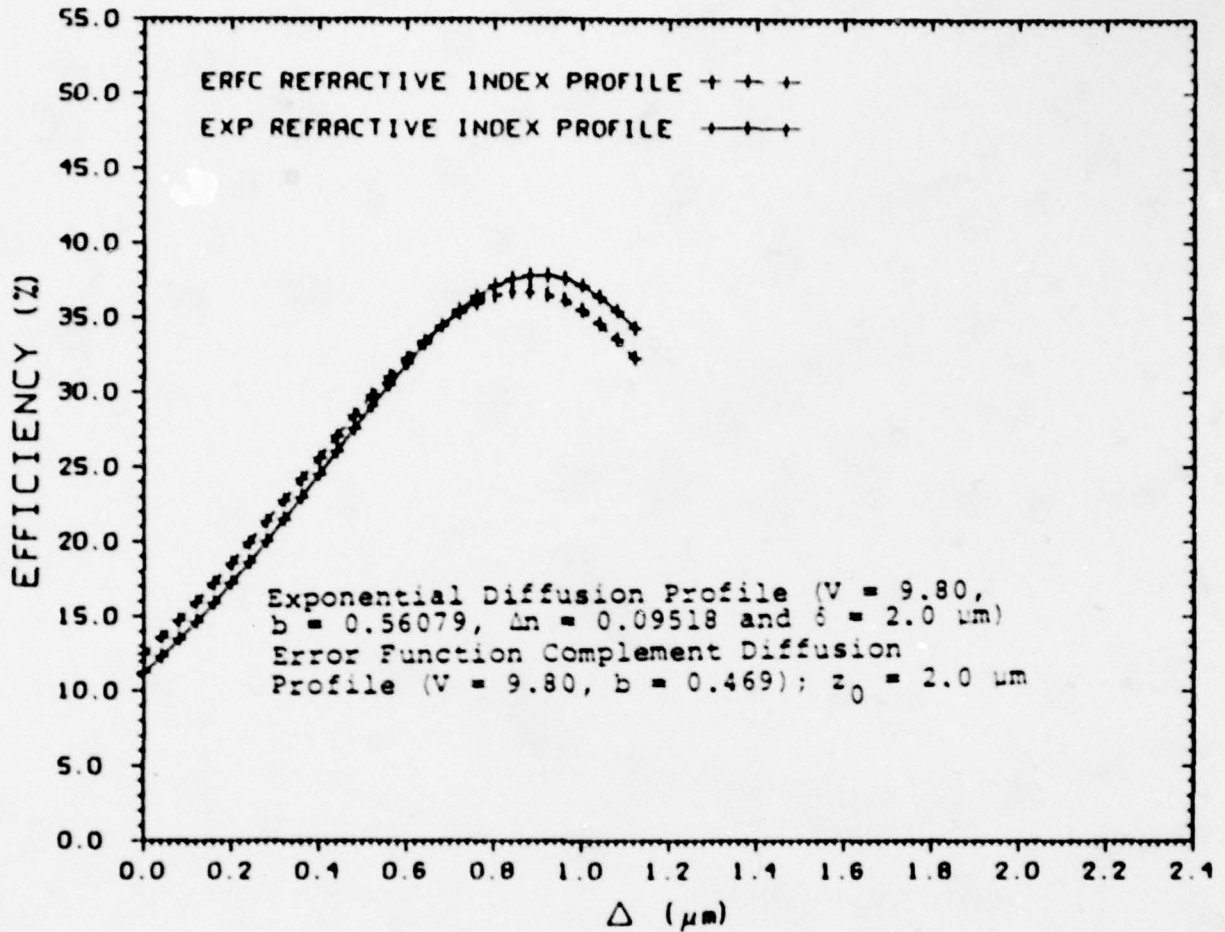


FIGURE 35

The electric field emerging from the laser diode and incident along the z-direction upon the edge of the planar waveguide was assumed to be of the form:

$$\psi_1(x, z) = A(z) \exp \left[- \left(\frac{x-\Delta}{w_1} \right)^2 \right] \exp \left[-i \frac{k(x-\Delta)^2}{2R_1(z)} \right] e^{-i(kz-\omega t)}, \quad (2.31)$$

where $A(z)$ is a z-dependent amplitude, Δ is a transverse offset, $k = 2\pi/\lambda$, and $w_1(z)$ and $R_1(z)$ satisfy the usual relations

$$w_1^2(z) = w_{10}^2 \left[1 + \left(\frac{\lambda z}{\pi w_{10}^2} \right)^2 \right] \quad (2.32)$$

and

$$R_1(z) = z \left[1 + \left(\frac{w_{10}^2}{\lambda z} \right) \right] \quad (2.33)$$

Similarly, the waveguide mode was assumed to be of the form

$$\psi_2(x,z) = B(z) \exp \left[- \left(\frac{x}{w_{20}} \right)^2 \right] e^{-i(kz - \omega t)} \quad (2.34)$$

where w_{20} is the waist radius of the waveguide mode and $B(z)$ is a z -dependent amplitude. The coupling efficiency η is given by

$$\eta = \frac{\left| \int_{-\infty}^{\infty} \psi_1(x,z) \psi_2^*(x,z) dx \right|^2}{\int_{-\infty}^{\infty} \psi_1(x,z) \psi_1^*(x,z) dx \int_{-\infty}^{\infty} \psi_2(x,z) \psi_2^*(x,z) dx} \quad (2.35)$$

Performing the necessary integrations, one finds

$$\eta = \frac{\eta_0}{\sqrt{1+\gamma}} \exp \left[- \frac{(w_{20}/w_1) \eta_0 + 2\gamma}{1+\gamma} \frac{\Delta^2}{w_2^2} \right] \quad (2.36)$$

$$\text{where } \gamma = \left[\frac{k}{2R_1(z)} \right]^2 \left[\frac{w_1 w_{20} \eta_0}{2} \right]^2 \quad (2.37)$$

$$\text{and } \eta_0 = \frac{2 w_1 w_{20}}{w_1^2 + w_{20}^2} \quad (2.38)$$

is the maximum value of the coupling efficiency when $z = 0$.

While this Gaussian-Gaussian coupling model is a very simple model, its predictions compare very favorably with the results of coupling experiments. This will be discussed in greater detail in Section 2.6 of this report. It is instructive to examine Equation (2.36) in some detail. For example, again assuming optimum transverse alignment ($\Delta = 0$), the role of the phase variation of $\psi_1(x,z)$ in degrading the coupling efficiency can be determined by plotting η for both the exact case and the case for which $R_1(z) = \infty$. A comparison of these two cases is shown in Figure 36 for $w_{20} = 1.4 \mu\text{m}$ and $w_{10} = 0.4 \mu\text{m}$. Both calculations yield virtually identical curves for $z > 30 \mu\text{m}$ and both give the same coupling efficiency for $z = 0$. However the "no phase" coupling efficiency goes through a large peak near $z = 2 \mu\text{m}$ whereas the inclusion of phase effects produces a coupling efficiency which is a relatively slow and monotonically decreasing function of z . The large peak in the "no phase" coupling efficiency is to be expected since, as shown in Equation 2.32, the width of $\psi_1(x,z)$ increases with z and so there exists some value of z for which $\psi_1(x,z)$ and $\psi_2(x,z)$ have equal widths. Figure 37 shows the phase of $\psi_1(x,z)$ as a function of x for $\Delta = 0$ and $z = 2.0 \mu\text{m}$. The severe departure from constant phase is responsible for the striking difference between the two curves in Figure 36.

EFFECT OF PHASE ON COUPLING EFFICIENCY

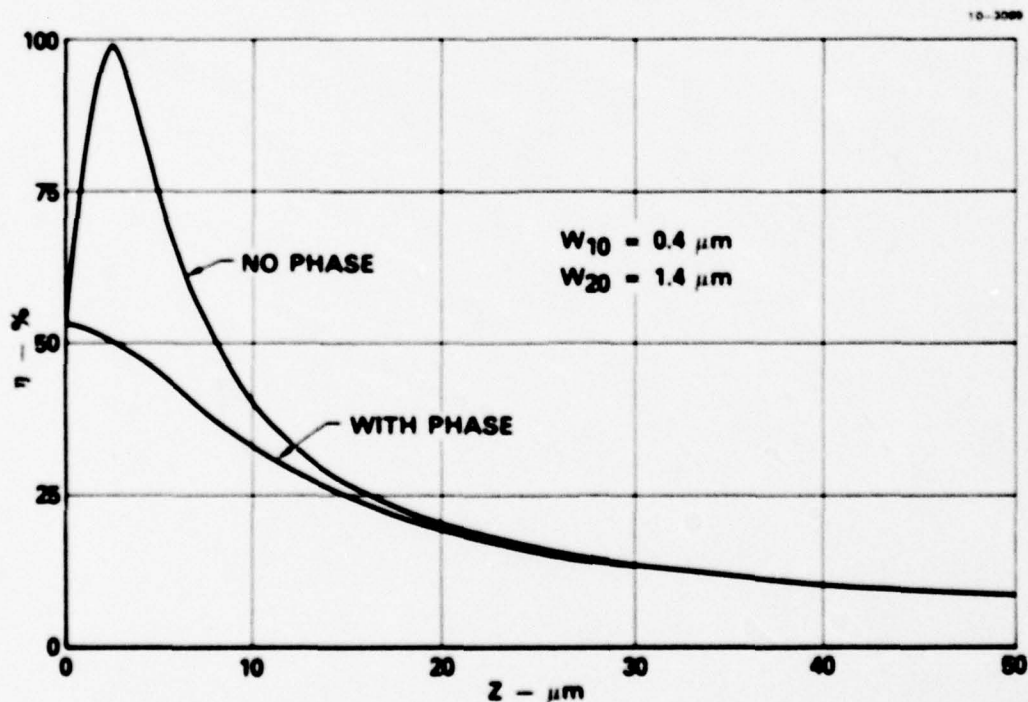


FIGURE 36

GAUSSIAN BEAM PHASE VARIATION

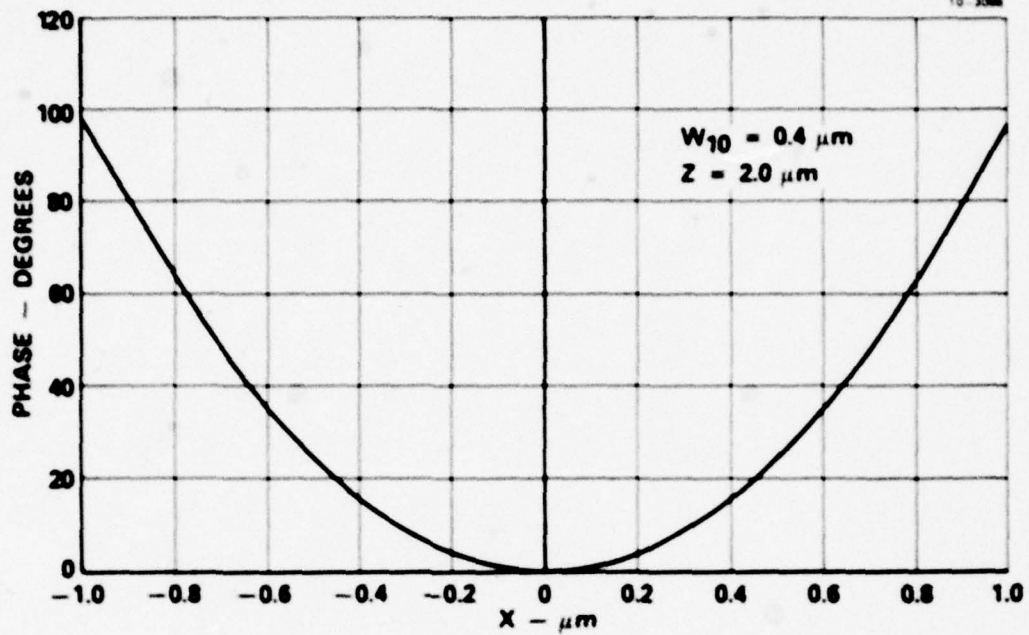


FIGURE 37

2.9 Laser Diode Development

The laser diodes used in this program were fabricated from commercial (ITT) wafers of double heterostructure GaAlAs. Figure 38 shows a typical diode layer configuration including dopant concentrations and layer thicknesses. The far-field radiation patterns from several such diodes were measured and found to exhibit a Gaussian dependence upon the coordinate perpendicular to the junction

DIODE LAYER CONFIGURATION

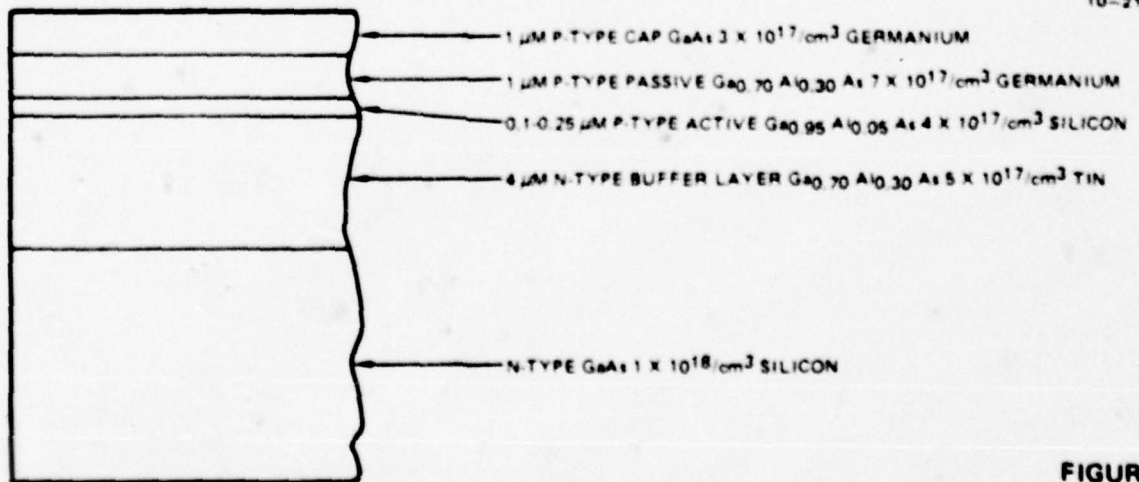


FIGURE 38

plane. The Gaussian waist parameter (w_0) values required to fit the data typically fell in the range $0.4 \mu\text{m} < w_0 < 0.5 \mu\text{m}$. The radiation pattern measurements for the ITT-material laser diodes were compared to those for other commercial diodes and an example is shown in Figure 39. The solid lines are Gaussians and the tabular inset gives the type of laser diode, the full width at the half-power (FWHP) points, and the waist diameter ($= 2w_0$).

10-2887

TRANSVERSE LASER BEAM PROFILE

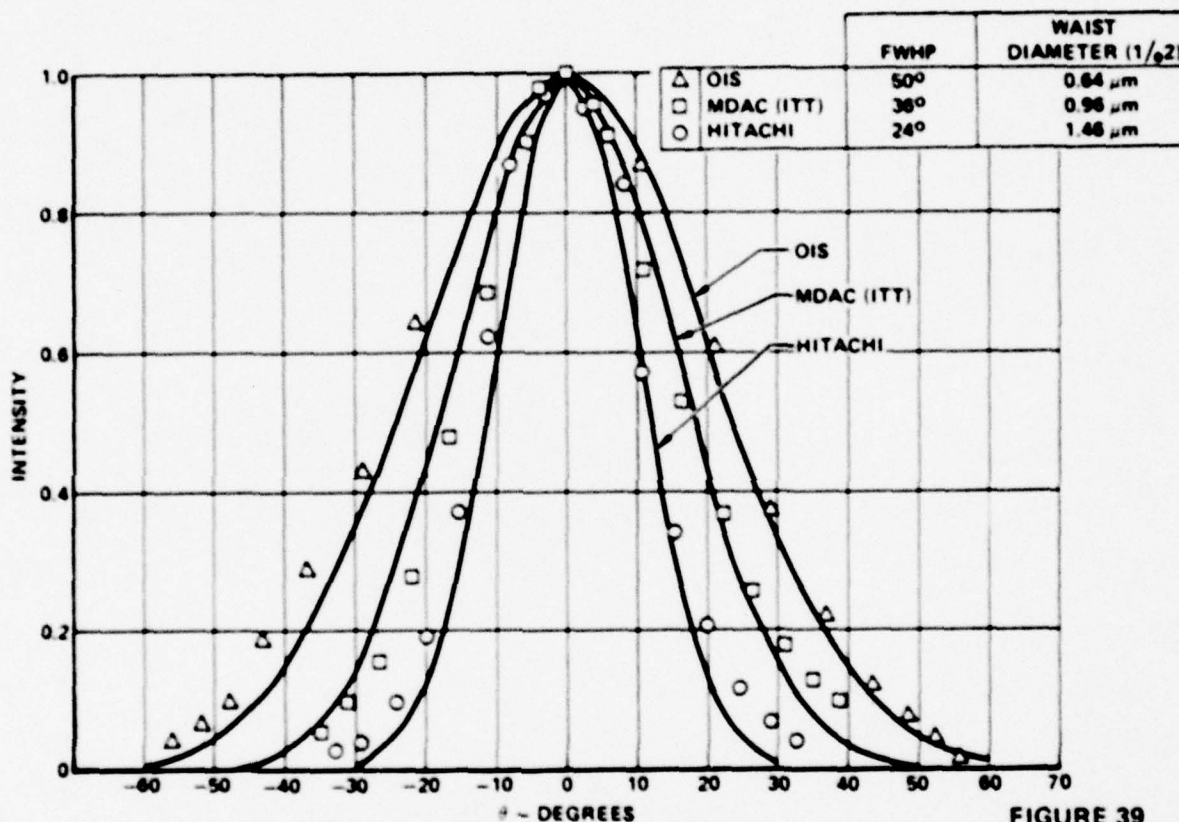


FIGURE 39

For use in the coupling alignment sensitivity measurements, the laser diodes were mounted protruding from their heat sinks by about $9 \mu\text{m}$. The laser diodes used in the fabrication of the coupler chips were bonded to the silicon substrates by an indium soldering process. After oxidizing the silicon substrate surface, a layer of nichrome was electroplated onto the SiO_2 , followed by a layer of sputtered gold, a layer of electroplated nickel, and a layer of electroplated indium solder layer. The final processing step was the indium soldering of the laser diode to the stack described above. This procedure was found to be successful provided each surface was kept clean before and during the deposition of the next layer.

2.10 Waveguide Edge Polishing

Twelve LiNbO_3 waveguides were successfully polished during the course of the program. The most serious problem, fracturing of the waveguide at the scribed identification mark during polishing, was eliminated by scribing the identification mark in the center of the LiNbO_3 substrate before depositing the titanium (Ti) layer. While some waveguide edges prove easier to polish than others, no consistent pattern could be identified and the procedure can be said to be reduced to routine.

The edge polishing procedure involved mounting the waveguides, grinding, and polishing. Mounting the waveguides was the most critical part of the process. The waveguides were stacked together with a thin layer of wax (as close to optical contact as possible) and a piece of similar material was mounted on each side of the stack to act as riders. Once in contact and cooled, the waveguides were heated in a fixture with weight applied to the stack to squeeze out excess wax.

The crystal surface polishing procedure consisted of three operations: (1) rough grinding, (2) fine grinding, and (3) polishing. The rough grinding step required more than one abrasive size if less than 0.5mm of material needed to be removed. If more than 0.5mm of material needed to be removed then several different size abrasives were required. The fine grinding step required only one abrasive size. The polishing step first required cleaning the surface and then two different size polishing powders were used to achieve the desired surface finish.

2.11 Optical Coating Development

The optical coating development consisted of the design, deposition, and evaluation of a thin film antireflection (AR) coating. The design consisted of a single layer of 99.9999% pure fused silica (SiO_2). The AR coating was designed to have an optical thickness of a quarter wavelength at $\lambda_0 = 840$ nm, which is the approximate center of the ILD wavelength band. The ILD wavelength limits were defined to be 810 nm to 870 nm, which had corresponding reflectances of 0.12% and 0.11%, respectively. Figure 40 is a plot of the calculated reflectance versus wavelength for the $\text{Ti}:\text{LiNbO}_3$ waveguide and the SK-1 glass witness sample. Table 1 is a list of reflectance values associated with Figure 40.

AR COATING FOR WAVE GUIDE EDGE (ILD Wavelength Range: 810 nm — 870 nm)

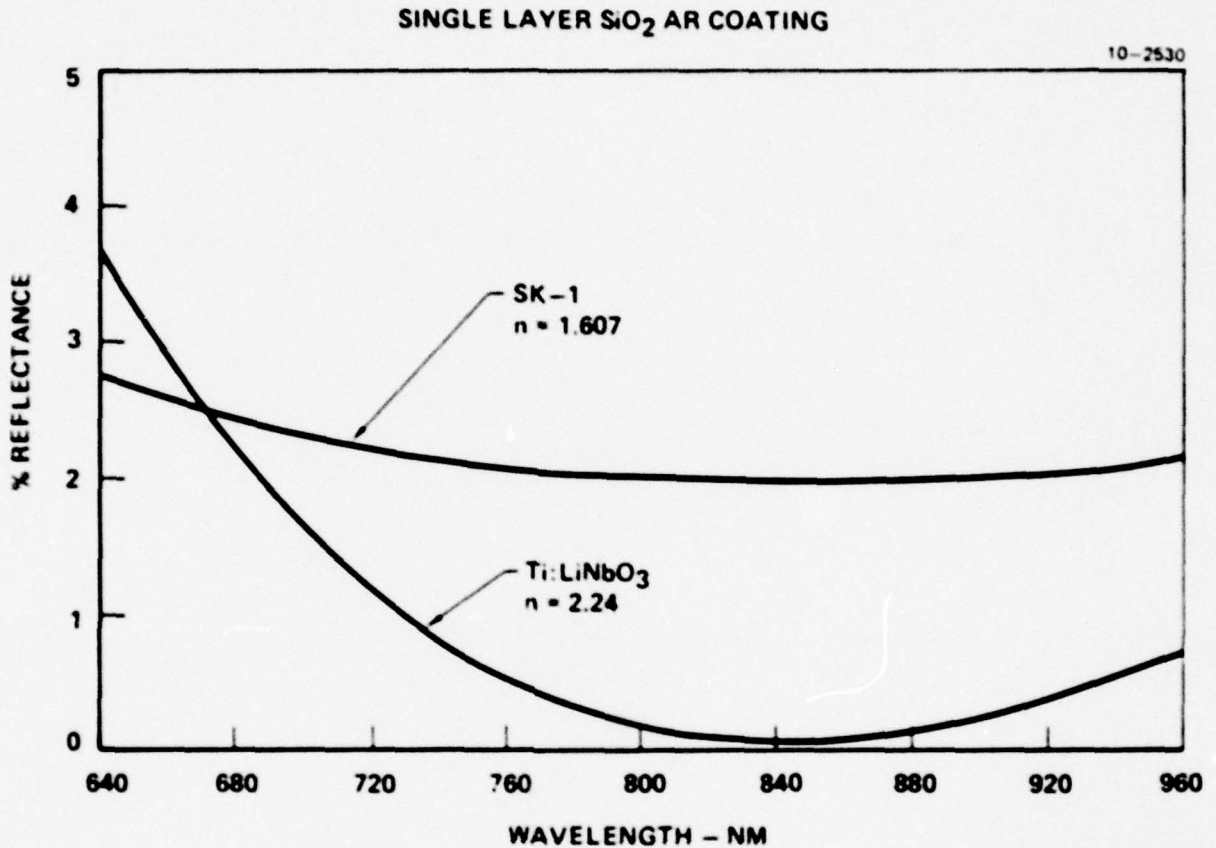


FIGURE 40

The deposition parameters of the thin film AR coating were: $\lambda = 840$ nm; optical thickness (nt) = $\lambda/4$; substrate temperature = 250°C; and the deposition pressure = 2×10^{-5} torr. A schott glass, SK-1 was used as the witness sample in each coating run.

The evaluation of the thin film coating consisted of: (1) determining the index of refraction and thickness of the deposited thin film using an ellipsometer, (2) measuring the reflectance at near normal incidence (using HeNe laser radiation, $\lambda = 633$ nm) of the witness sample and waveguide, and (3) measuring the reflectance at near normal incidence (using ILD laser radiation) of the witness sample and waveguide.

TABLE I
PERCENTAGE REFLECTANCE VERSUS WAVELENGTH

10-2525

	Ti:LiNbO ₃ n = 2.24	SK-1 n = 1.607
WAVELENGTH (nm)	REFLECTANCE (%)	REFLECTANCE (%)
630	4.16	2.86
633	4.02	2.82
645	3.51	2.71
660	2.92	2.58
675	2.40	2.47
690	1.94	2.37
705	1.54	2.26
720	1.19	2.21
735	0.90	2.14
750	0.66	2.09
765	0.46	2.05
780	0.31	2.02
795	0.20	2.00
810	0.12	1.98
825	0.08	1.97
840	0.06	1.97
855	0.07	1.97
870	0.11	1.98
885	0.17	1.99
900	0.25	2.01
915	0.34	2.03

2.12 Bulk Electromechanical Coupling Experiment

In order to determine the fabrication tolerances associated with the development of a laser diode-to-diffused waveguide coupler, the sensitivity of the coupling efficiency to both longitudinal (z) and transverse (x) alignment was measured. A sketch of the experimental system is shown in Figure 41 and a photograph is shown in Figure 42. In this system, a GaAlAs laser diode was mounted on a series of stages which provided three translational and two rotational degrees of freedom. Two Burleigh Inchworm translators were used to scan the laser diodes in the x- and z-directions with respect to the (fixed) waveguide while a silicon detector monitored the intensity of the m-line coupled out of the waveguide through a rutile prism.

Since the Burleigh Inchworms were nonlinear, it was necessary to develop a technique for accurately measuring the displacement of the laser diode with respect to the LiNbO₃ waveguide. To accomplish this, two Michelson interferometers (with a HeNe laser source) were constructed with one mirror of each interferometer attached to adjacent sides of the translation stage. The data were taken using a

ILD/WAVEGUIDE COUPLER EXPERIMENT

10-2527

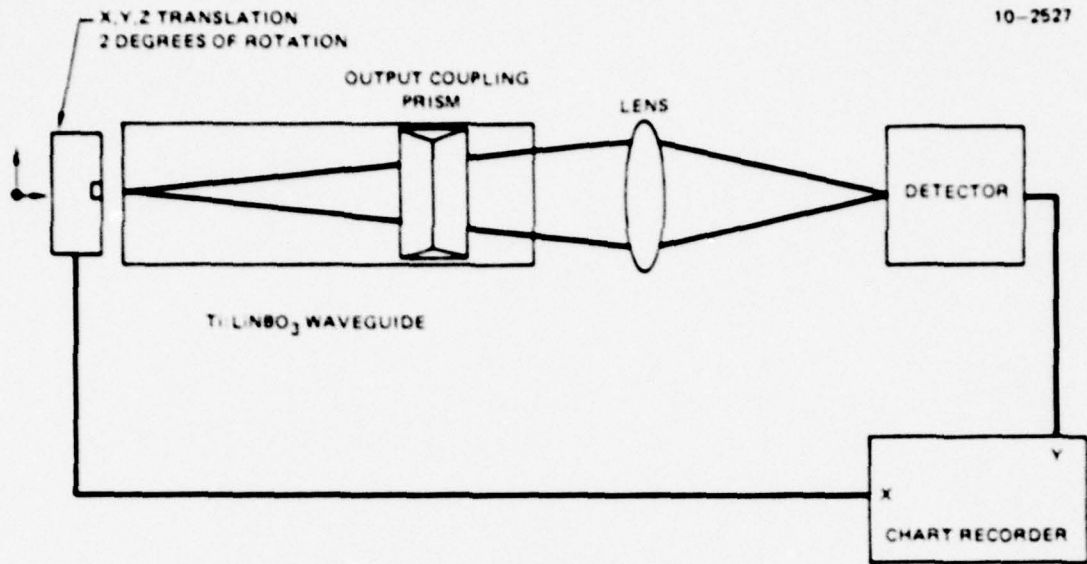


FIGURE 41

PHOTO OF COUPLING APPARATUS

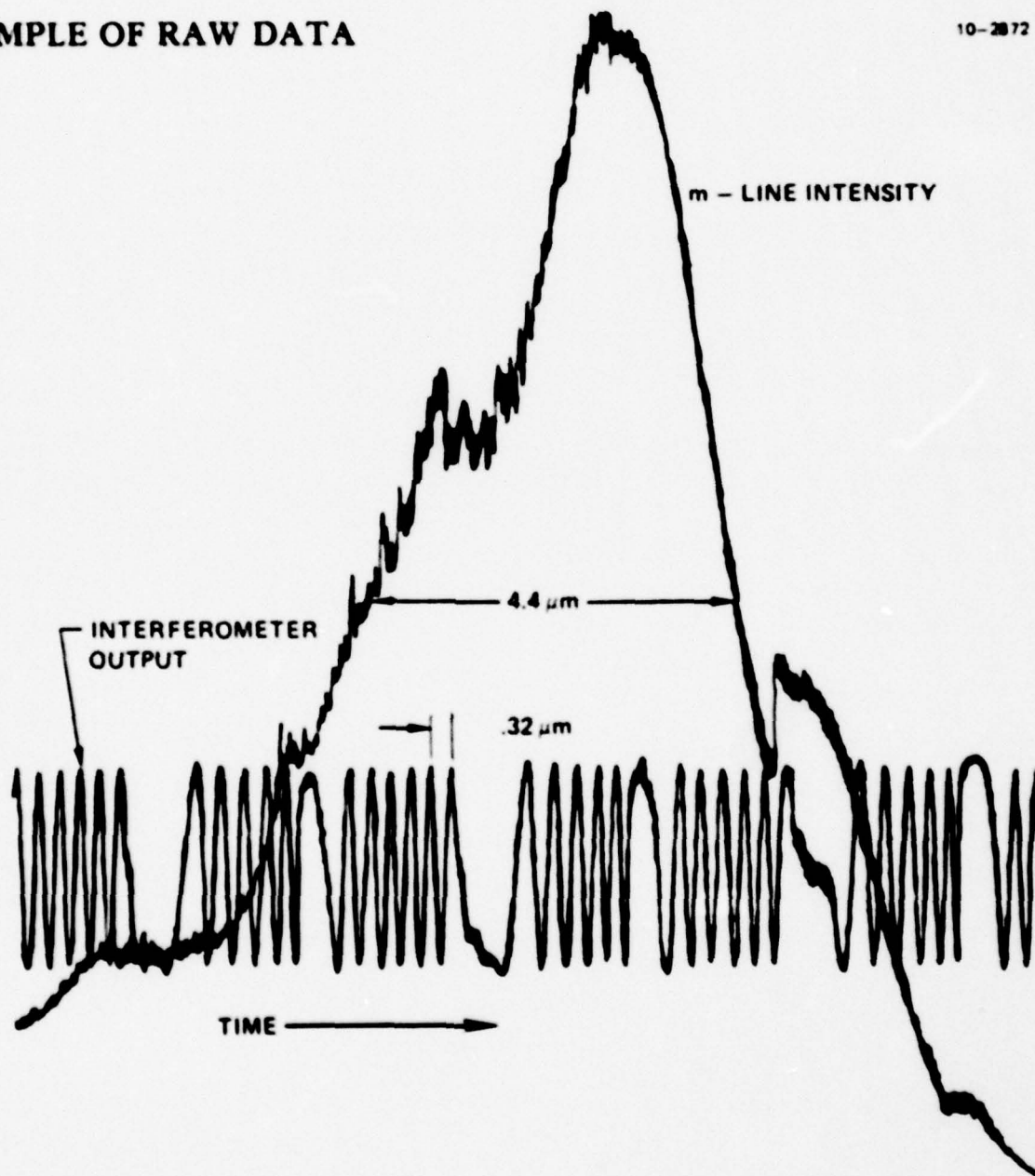


FIGURE 42

2-pen chart recorder with a time based scan. While one pen recorded the *m*-line intensity, the second pen recorded the fringes produced by the appropriate interferometer in response to the motion of the Burleigh Inchworm. In this way, an accurate record of the *m*-line intensity as a function of either *x* or *z* was readily obtained. As an example of a segment of a raw data, Figure 43 shows a typical scan of the *m*-line intensity as a function of the transverse coordinate *x*. It is

SAMPLE OF RAW DATA

10-2872



important to note that the Inchworm cannot scan continuously over a range sufficiently large to cover the total displacement needed in the experiment. Instead, the Inchworm "pauses", takes another "bite", and then continues scanning. These "pauses" lead to shoulders in the m -line scan and elongation of the fringes and are clearly evident in Figure 43. In spite of this disadvantageous feature of the Burleigh Inchworms, no fringes are lost if the data is analyzed carefully and, for example, the data of Figure 43 can be corrected to give the plot shown in Figure 44.

REDUCTION OF DATA OF FIGURE 43 10-3145

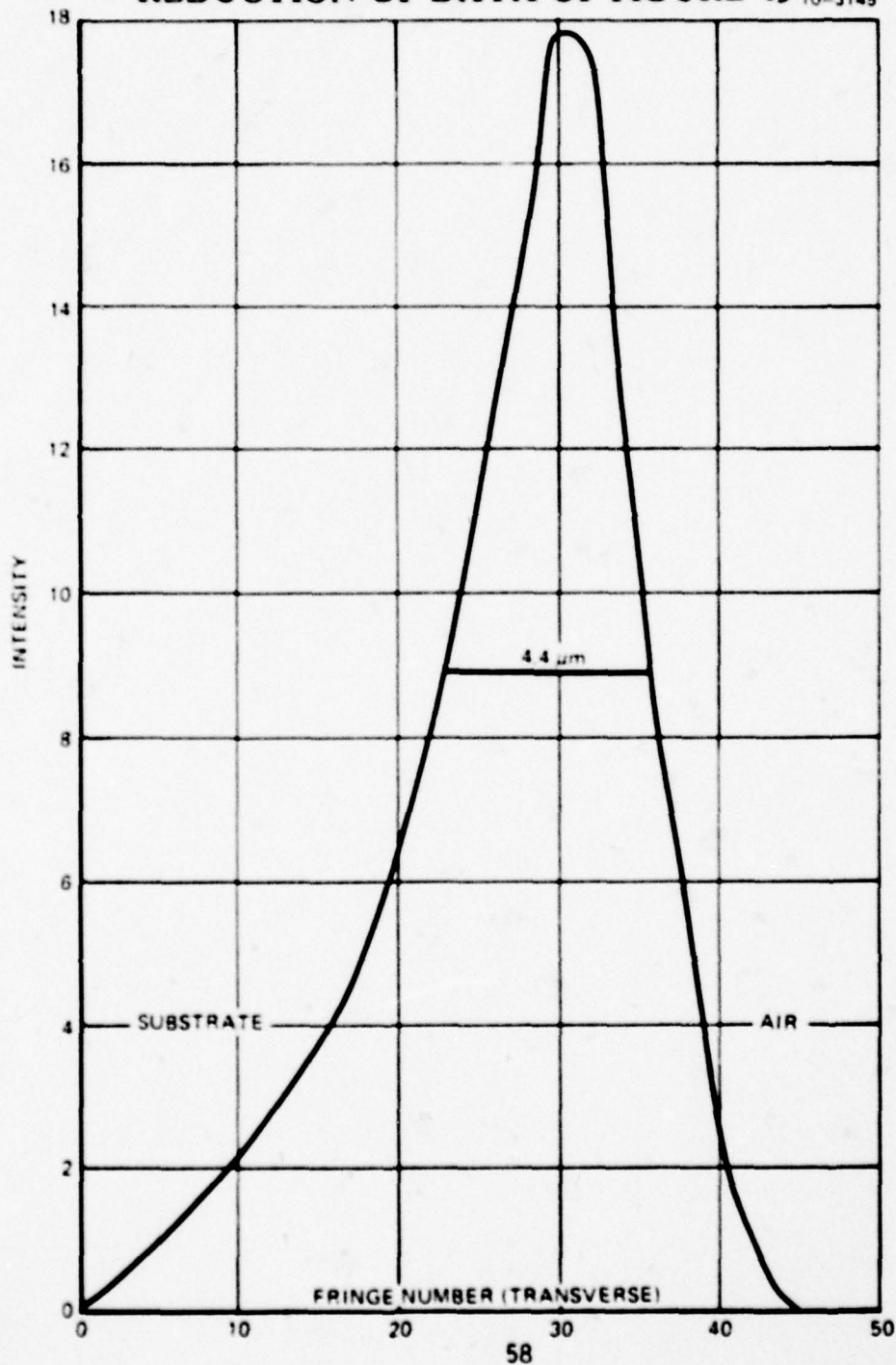
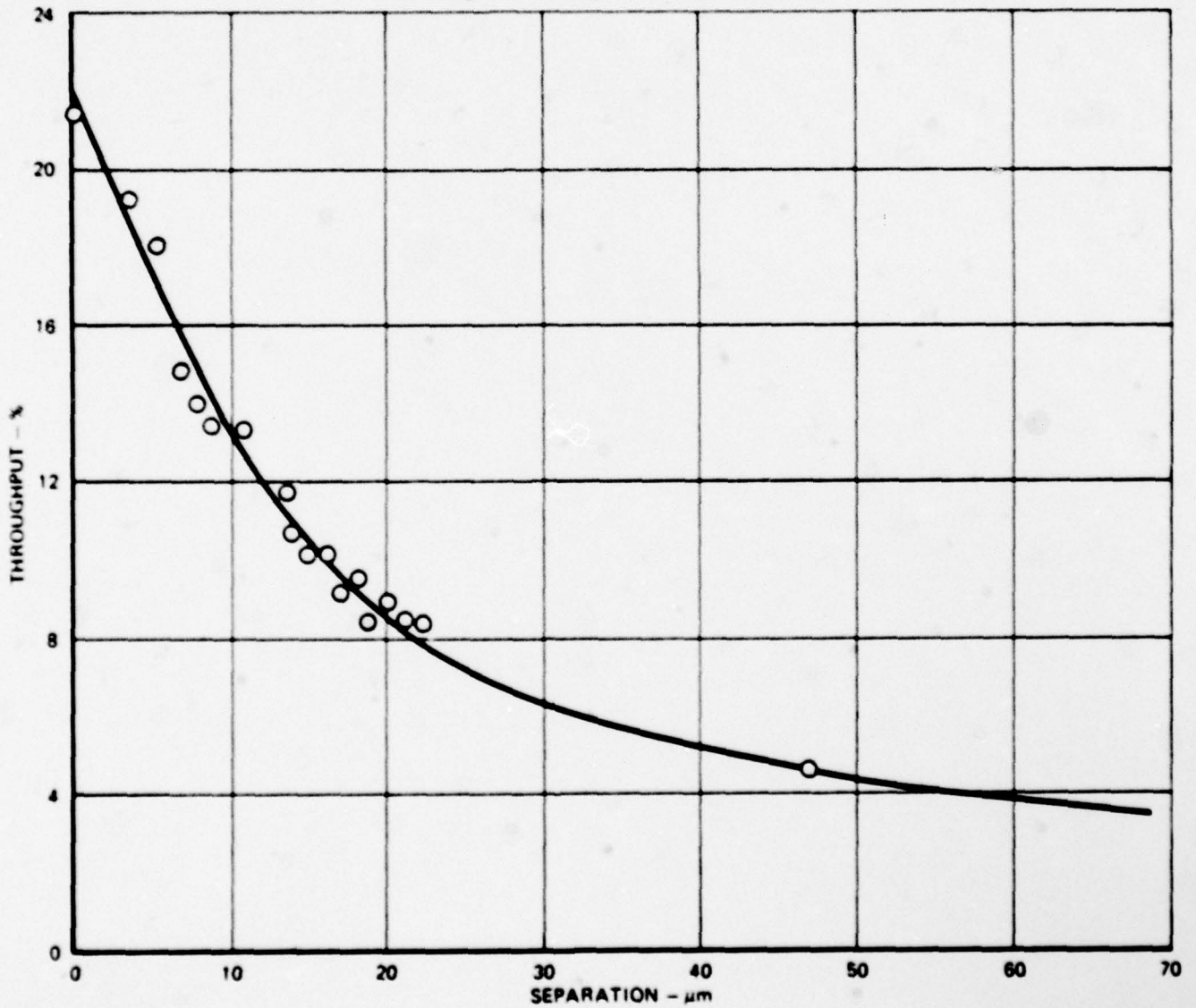


FIGURE 44

Figure 45 presents the results of our measurements of the m-line intensity as a function of z , the longitudinal separation, for a waveguide with an AR-coated edge. The data were collected by performing a transverse scan (x) for several values of z , and each data point in Figure 45 represents the maximum intensity for each value of z . The solid line is merely a guide to the eye, not a fit to the data, and actually passes through one additional data point at $z = 72.5 \mu\text{m}$ which is not shown on this plot. It should be noted that the vertical axis in Figure 45 gives the system throughput and not the actual butt-coupling

THROUGHPUT EFFICIENCY VS. ILD/WAVEGUIDE SEPARATION
Waveguide Edge is AR Coated

10-2726



efficiency. The system throughput was decreased from 100% by the butt-coupling efficiency, the prism coupling efficiency, propagation losses in the waveguide, reflection losses at the prism edge, and reflection losses at the lens positioned in front of the detector. For the waveguide used in this experiment, an estimate of 45% for all other system losses resulted in a butt-coupling efficiency of 50%. Reduced estimates of the prism coupling efficiency give a corresponding increase in the inferred butt-coupling efficiency.

In addition to providing a measure of the sensitivity of the m-line intensity to longitudinal misalignment, the experiment measured the transverse misalignment sensitivity. As the laser diode was translated in the x-direction, the m-line intensity recorded by the detector assumed a roughly Gaussian shape and a few examples are shown in Figure 46. The full width at half (power) maximum (FWHM)

10-2085

THROUGHPUT VS. TRANSVERSE DISPLACEMENT

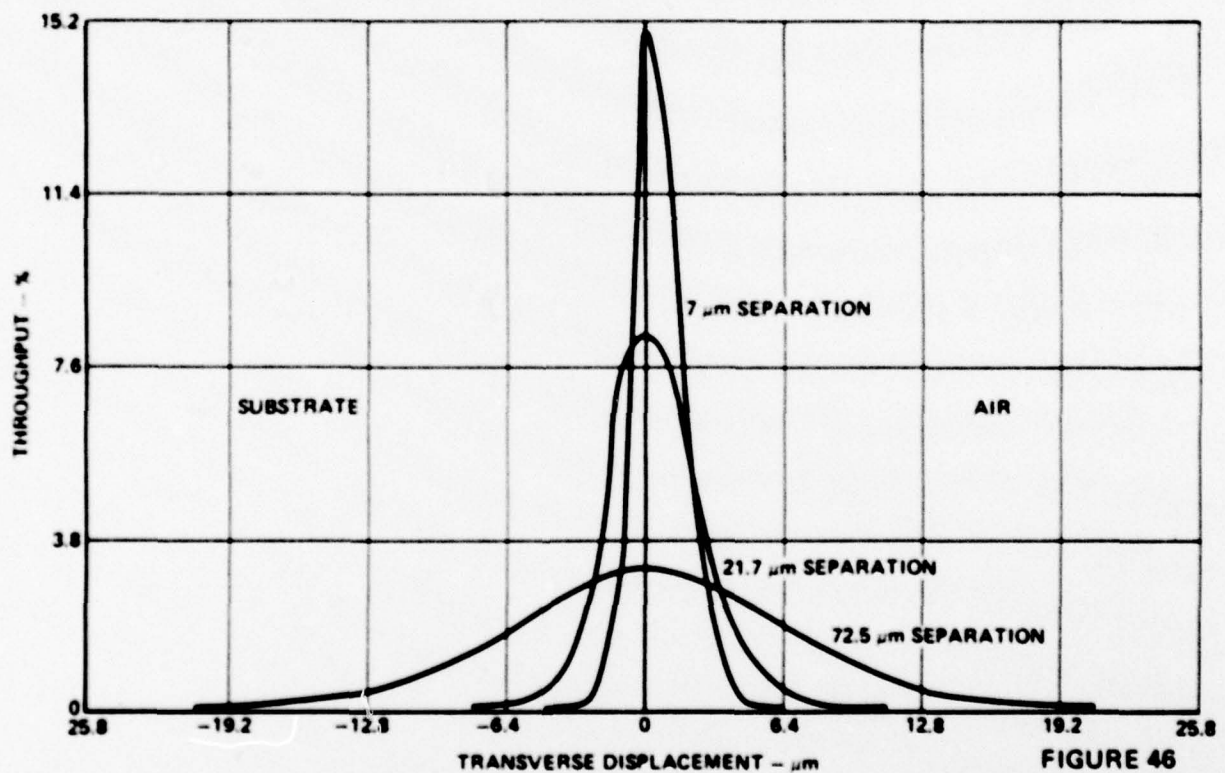


FIGURE 46

of this intensity distribution is plotted in Figure 47 as a function of the longitudinal (z) separation between the laser diode and the waveguide edge. The solid line is a least squares fit to the data points and has the equation

$$\text{FWHM } (\mu\text{m}) = 0.16z + 1.3 \mu\text{m} \quad (2.39)$$

where z is in micron units.

FWHM VS. ILD/WAVEGUIDE SEPARATION

Waveguide Edge is AR Coated

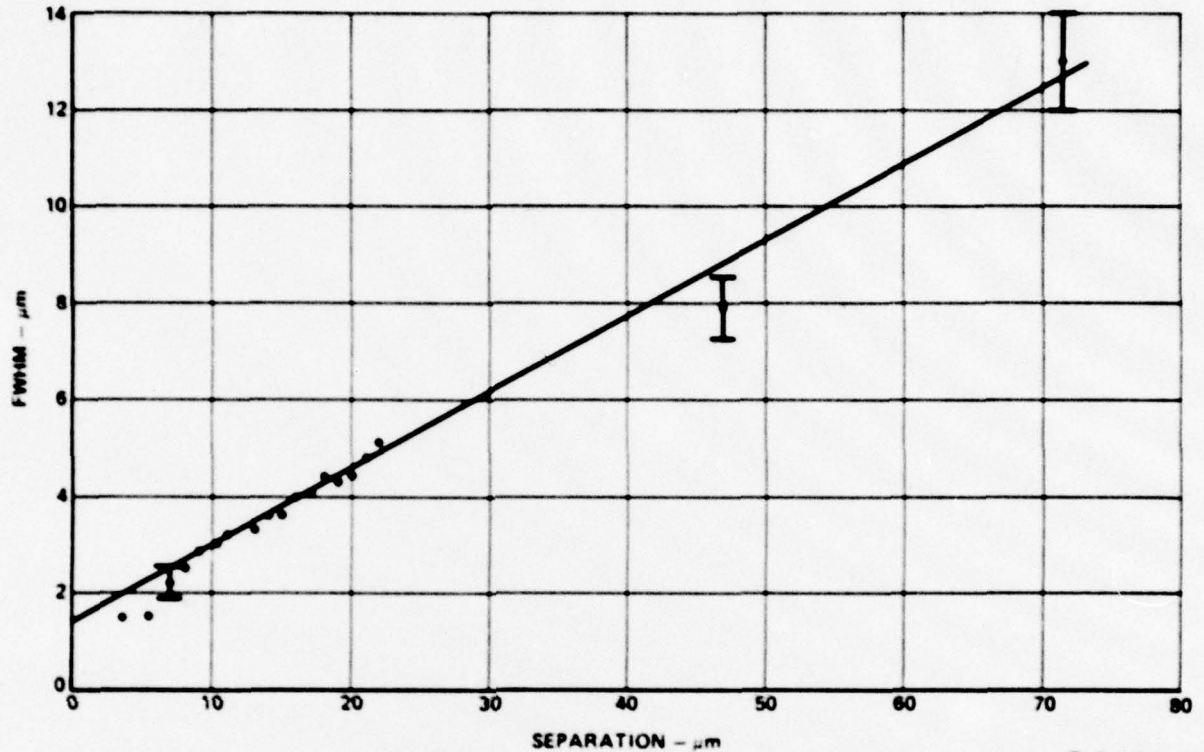


FIGURE 47

The data presented in Figure 45 and 47 provide information regarding the alignment tolerances associated with the fabrication of a hybrid coupling chip. Figure 45 demonstrated that the coupling efficiency was a slow function of the longitudinal separation. A separation of approximately 15 microns resulted in only a 50% reduction from the maximum coupled power. The transverse alignment tolerance, on the other hand, was extremely tight. For laser/waveguide separations of 5.0 μm or less, a transverse displacement of one micron or less in either direction reduced the coupled power by 50%. Therefore, the fabrication of a hybrid coupler chip requires a transverse positioning capability with a resolution of less than one micron.

The bulk electromechanical apparatus has been used to evaluate the effectiveness of the AR edge-coatings in reducing feedback to the laser diode. Hunsperger, Yariv, and Lee¹⁸ demonstrated that, when placed in close proximity, the polished waveguide edge and the front face of the laser diode formed a Fabry-Perot interferometer which modified the amount of power that was coupled into the waveguide.

In their experiment, the coupled power oscillated between maxima and minima as a function of the longitudinal (z) separation, with a modulation depth of approximately 20% of the average power. This same effect has been observed in conjunction with the work with a similar value for the modulation depth ($\sim 20\%$). Figures 48 and 49 show plots of the m-line intensity as a function of z for both an uncoated and a coated waveguide edge. For the coated waveguide, the modulation depth has been reduced to approximately 2% of the average power and represents a factor of ten improvement over the uncoated edge.

THROUGHPUT VS. SEPARATION DATA
SHOWING FABRY-PEROT EFFECT

10-2873

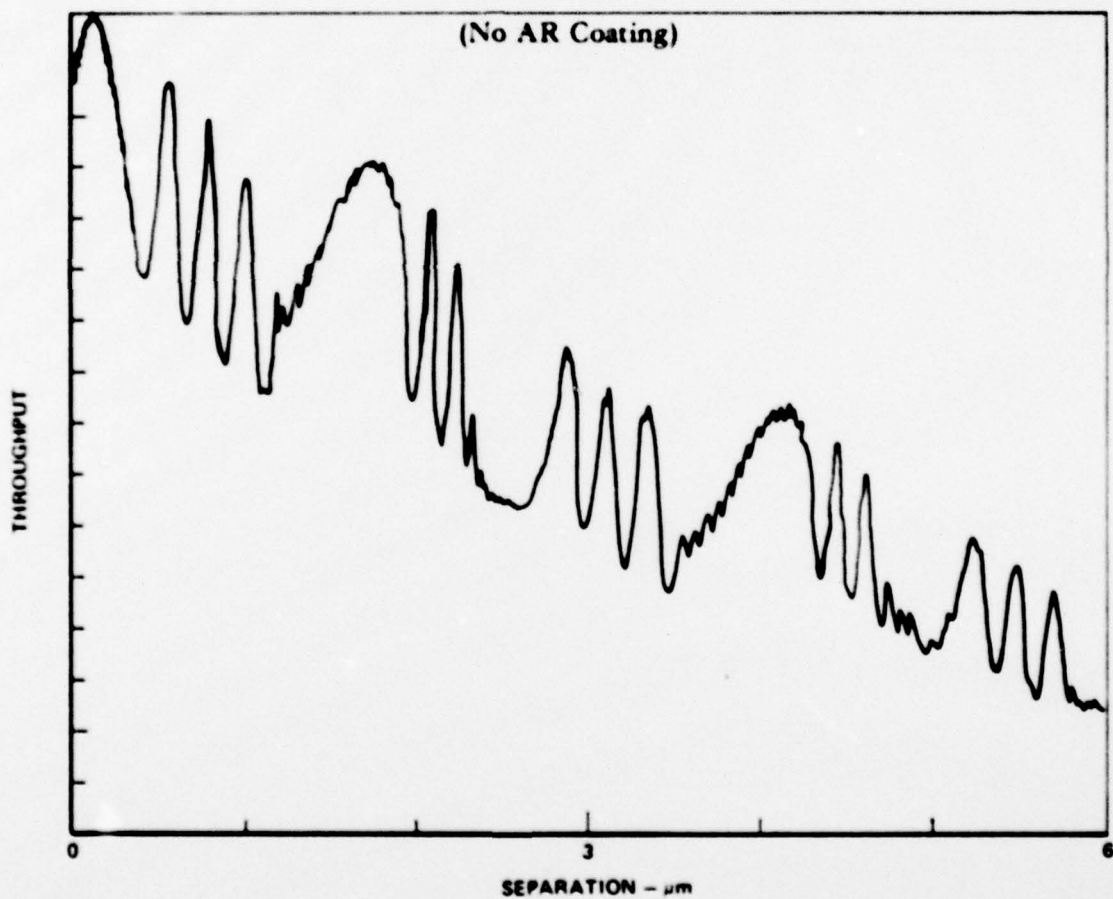


FIGURE 48

THROUGHPUT VS. SEPARATION DATA (With AR Coating)

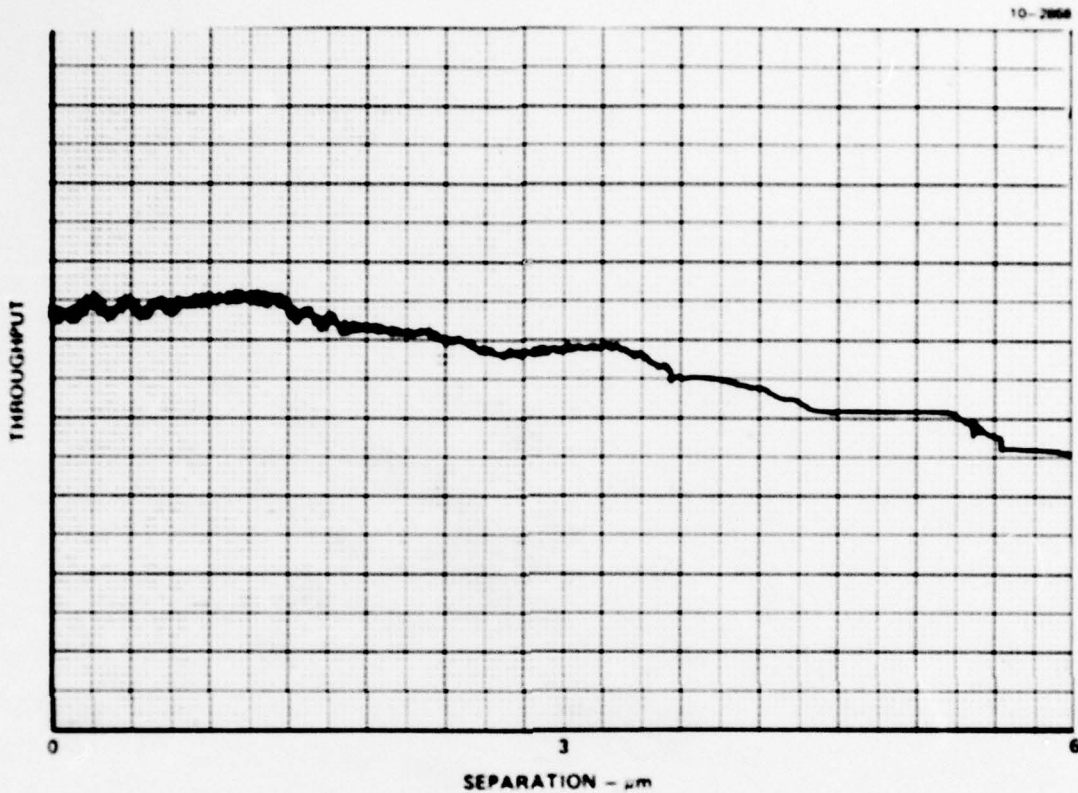


FIGURE 49

As mentioned in Section 2.2 of this report, the Gaussian-Gaussian coupling model provides a good fit to the measured coupling sensitivity, as shown in Figure 50. In comparing Equation (2.36) (with $\Delta = 0$) with the data, it was necessary to specify both w_{10} and w_{20} . The first of these was inferred to be $w_{10} = 0.4$ micrometers from measurements of the laser diode far field pattern. The second parameter w_{20} was treated as an adjustable parameter. The agreement between theory and experiment is quite good for $1.5 \mu\text{m} \geq w_{20} \geq 1.4 \mu\text{m}$. If one equates $2w_{20}$ with the mode depth of the TE_0 guided wave in Ti:LiNbO_3 , one obtains a $3 \mu\text{m}$ mode depth which is consistent with other measurements and calculations.

It is important to note that the vertical axis of the plot in Figure 50 is throughput and not coupling efficiency. The experimental points are ratios of the m-line intensity to the total intensity emitted by the laser diode. To compare theory and experiment, the coupling efficiency given by Equation (2.36) was

LONGITUDINAL SENSITIVITY Theory and Experiment

10-2100

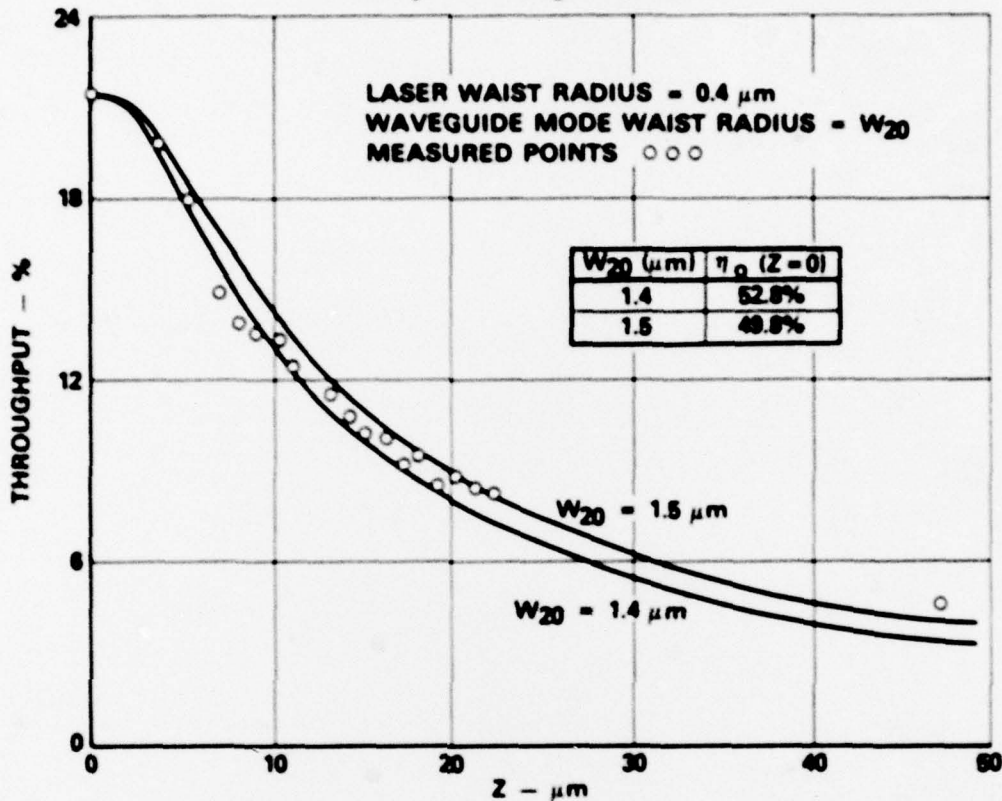


FIGURE 50

normalized so that the values at $z = 0$ were the same. This is equivalent to multiplying the edge-coupling efficiency η by a transmission factor which accounts for all reflections, propagation losses in the waveguide, and the prism coupling efficiency. Since the agreement between theory and experiment is very good, this fitting procedure can be used to extract the actual (maximum) edge-coupling efficiency from the data. The inferred values of η_0 are shown in the tabular inset in Figure 50 and are $\eta_0 = 52.8\%$ and $\eta_0 = 49.8\%$ for $w_{20} = 1.5 \mu\text{m}$, respectively.

2.13 Prototype Coupler

The prototype coupler is presented in Figure 51. It consisted of an oxidized silicon substrate, ILD, Ti:LiNbO₃ waveguide, conducting pads, and bond wires. The substrate had a 1mm wide by 0.005mm deep channel in which a 1.27mm long by 0.25mm wide conducting/soldering pad was deposited. The prototype coupler required nine fabrication steps: (1) a 50.4mm diameter x 1.27mm thick silicon wafer was cut to

PROTOTYPE COUPLER SCHEMATIC

10-2531

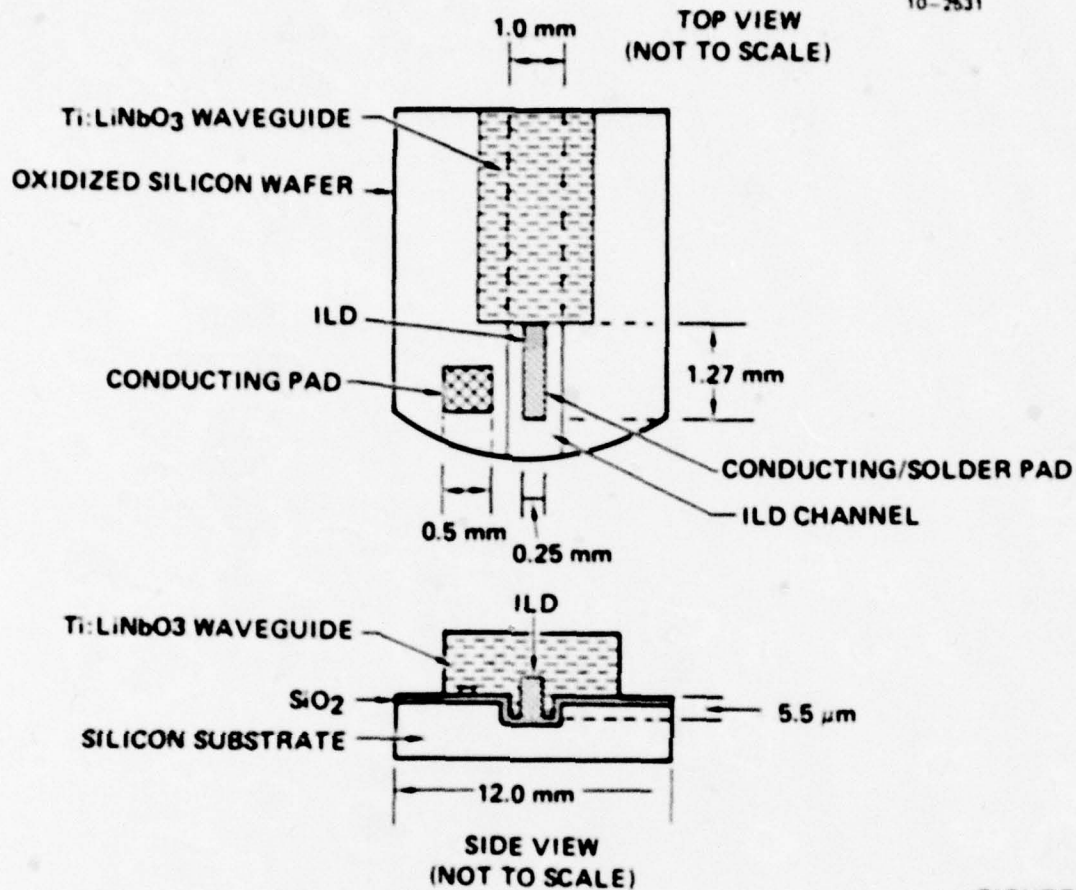


FIGURE 51

the designed configuration, (2) a channel was chemically etched into the silicon, which served to align the ILD junction to the plane of the waveguide, (3) a layer of silicon dioxide (SiO₂) was thermally grown over the entire surface to provide electrical insulation and a relatively low refractive index interface between the waveguide and substrate, (4) the conducting pads were deposited, (5) indium was plated over the electrode in the channel, (6) the ILD was soldered at the edge of the indium pad, (7) wire leads were bonded from the ILD to the wider electrode, (8) the waveguide was actively aligned and coupled to the ILD, and (9) the waveguide was bonded onto the substrate.

The prototype coupler successfully coupled radiation from the ILD to the waveguide. The photograph in Figure 52 shows the guided wave radiation propagating from the end of the waveguide. The vertical structure on the bottom of the center

RADIATION PATTERN OF INJECTION LASER DIODE COUPLED TO A Ti:LiNbO_3 WAVEGUIDE

10-2534

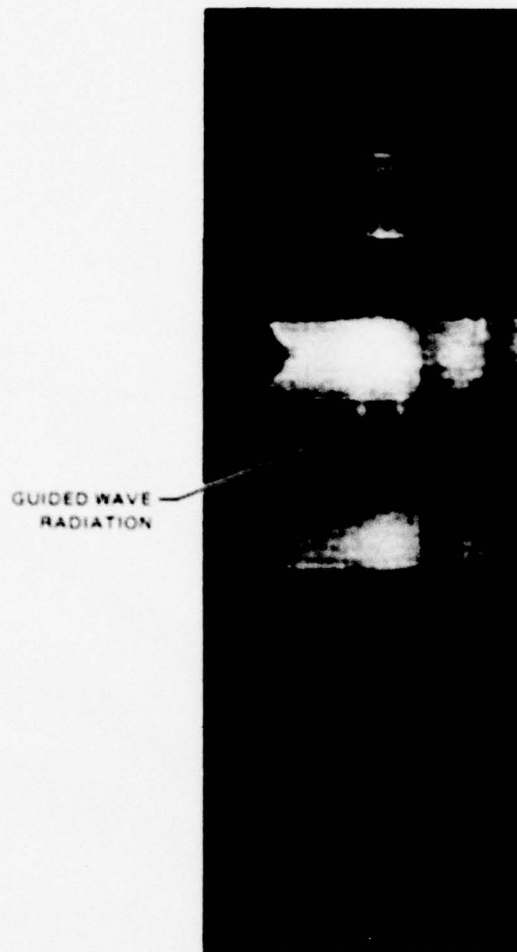


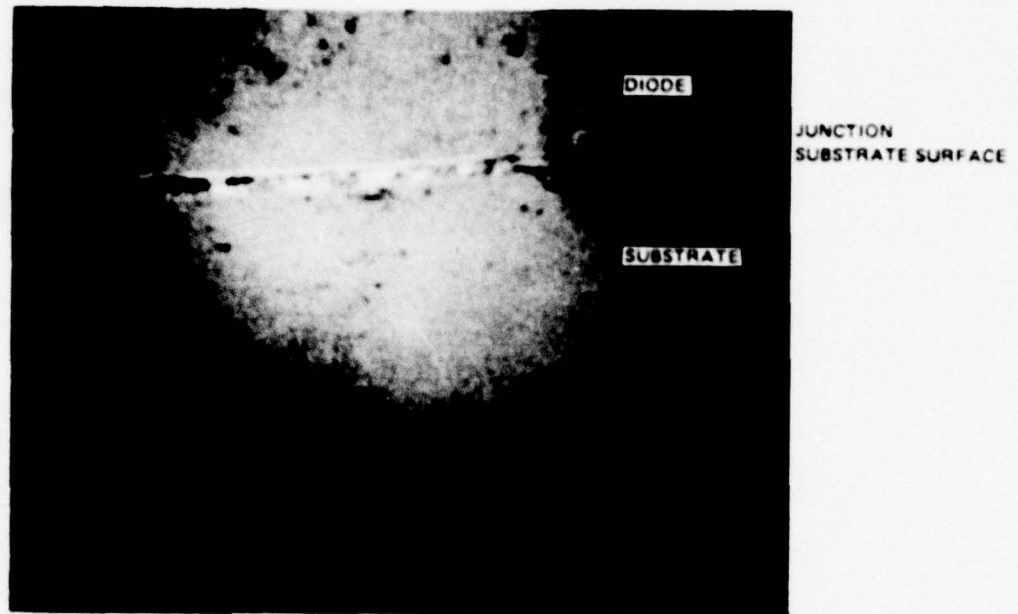
FIGURE 52

bar was the guided wave radiation. The bar structure resulted from substrate modes due to illumination by the ILD. The separation of the ILD and waveguide turned out to be about $12 \mu\text{m}$, so that only a few percent of the ILD light was coupled into the guided mode.

Initially, the height of the p-n junction was determined by first bonding an ILD onto a silicon substrate and then grinding and polishing the silicon and ILD to facilitate the measurement of the thickness of the bonding material. The entire fixture was placed under an infrared microscope and the ILD was activated to a fluorescing state. The separation between the p-n junction and the silicon substrate was measured to be approximately $5.5 \mu\text{m}$. A photograph of this fixture is shown in 53.

PHOTO OF SOLDERED ILD

10-2533



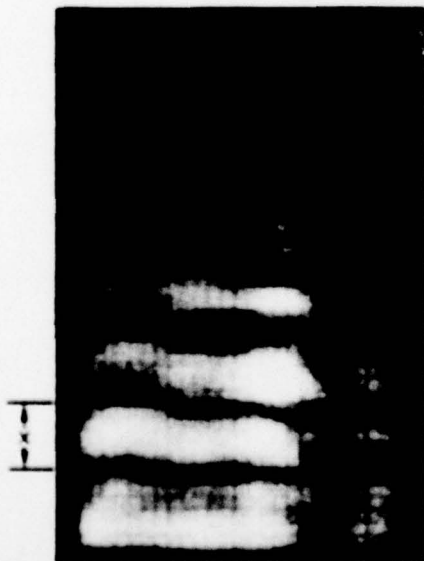
340X MAGNIFICATION

FIGURE 53

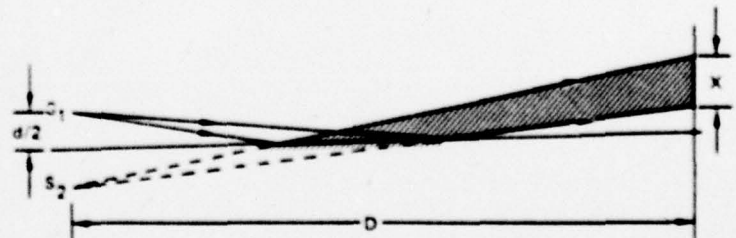
The photograph in Figure 54 is an interference pattern between the ILD and its reflection in the substrate before waveguide coupling. The interference pattern was used to determine the height of the p-n junction above the substrate (Figure 54b).

SOLDERED ILD RADIATION PATTERN

10-2532



a) PHOTO OF INTERFERENCE FRINGES



b) LLOYD'S MIRROR REPRESENTATION

FIGURE 54

The equation used to calculate the p-n junction height was:

$$\frac{d}{2} = \frac{\lambda_0 D}{2X}, \quad (2.40)$$

where λ_0 is the optical wavelength, D is the separation between the source and observation plane, and X is the separation between adjacent minima. This measurement was the standard procedure in characterizing the ILD soldering process.

2.14 Improved Coupler

A schematic of the improved coupler is shown in Figure 55. The basic fabrication procedure is similar to the prototype coupler with the following exceptions: (1) the substrate configuration is a 12mm by 19mm rectangle, (2) the ILD channel width is 0.5mm, and (3) the addition of two 1mm long by 0.25mm wide by 0.125mm deep drainage channels. The addition of the drainage channels is for the excess cement and requires an extra chemical etching step in the fabrication procedure.

A photograph of one of the two coupler units delivered to NRL is shown in Figure 56. The waveguide is bonded to the silicon substrate by UV curing cement and has been designed to overhang the silicon substrate to accommodate an output prism. Because of the tight alignment tolerance in the transverse dimension, the coupler chips achieved only a 5% - 10% throughput as measured through the edge of the waveguide. This represents an edge-coupling efficiency two to four times less than the theoretical limit of approximately 50%. To achieve the theoretical limit, it will be necessary to devise a scheme to reliably identify and maintain optimum alignment during fabrication. Figure 57 shows a photograph of the radiation emerging from the edge of Ti:LiNbO₃ waveguide mounted on the coupler chip. The sharp-edged vertical bars in the photograph correspond to substrate total-internal-reflection modes. The waveguide radiation is rather diffuse and is located at the center of the photograph.

IMPROVED COUPLER DESIGN

10-2535

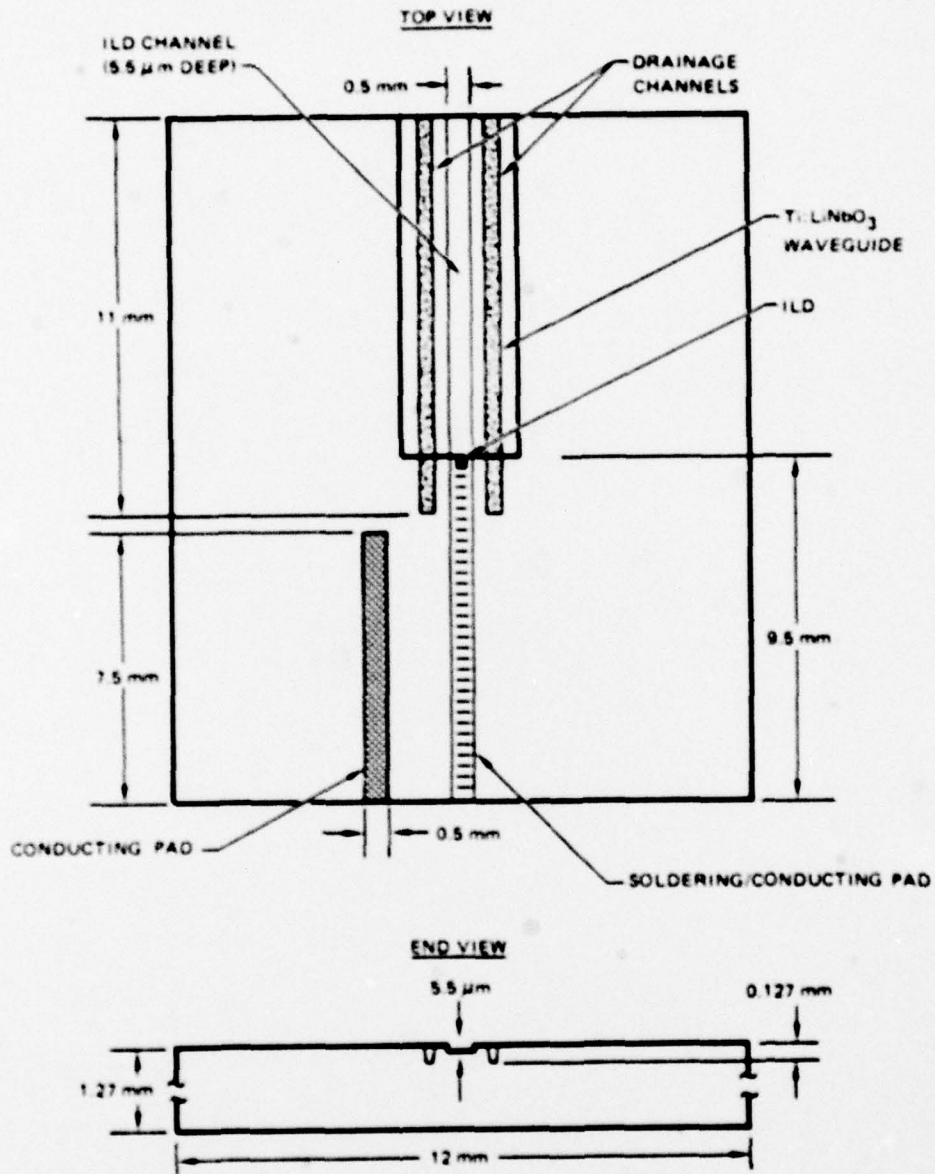


FIGURE 55

PHOTOGRAPH OF THE IMPROVED COUPLER

10-3201

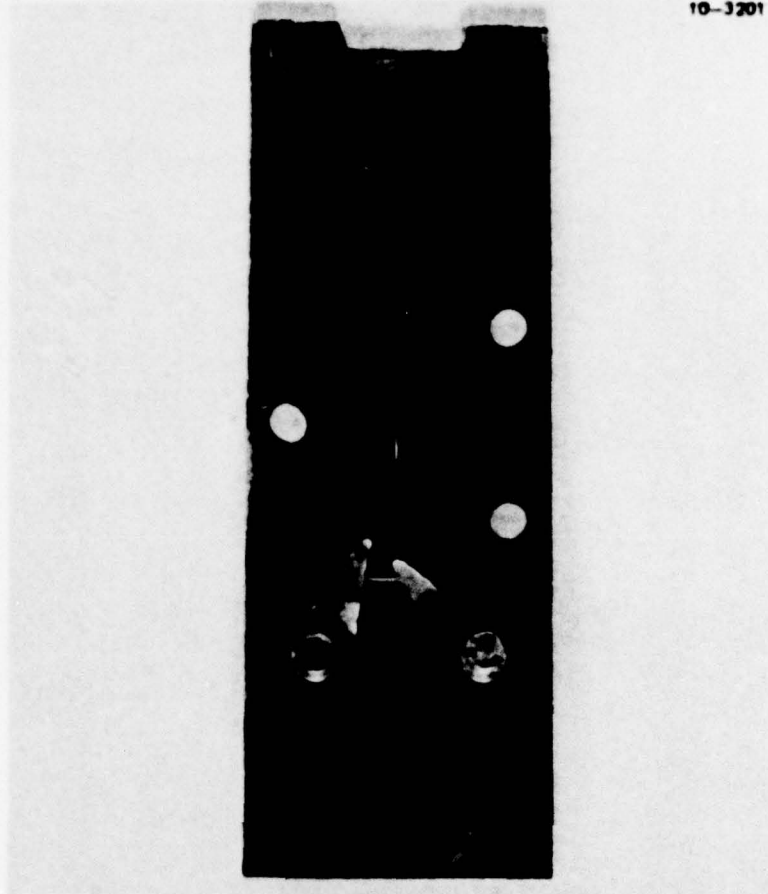


FIGURE 56

**PHOTOGRAPH OF RADIATION EMERGING
FROM WAVEGUIDE EDGE**

10-3202



FIGURE 57

3.0 CONCLUSIONS

The efficiency with which a double-heterostructure, GaAlAs laser diode can be edge-coupled to a Ti:LiNbO₃ diffused waveguide has been studied using both theoretical and experimental approaches. Both the analytical and the numerical estimates of the coupling efficiency predict maximum efficiencies of approximately 50% for the laser diodes used in this program. Measurements of the sensitivity of the coupling efficiency to both transverse and longitudinal misalignment have been performed and these measurements show the coupling efficiency to be a slow function of the longitudinal separation and a strong function of the transverse offset. When the measured data are fit to an analytical model, the results indicate that a maximum coupling efficiency of about 50% has been achieved. Two coupler chips were fabricated and delivered to NRL. The coupler chips used a flip-chip design and were fabricated on silicon substrates. The units delivered to NRL had coupling efficiencies of 5% - 10% and thus fell short of the theoretically predicted efficiency. This result was due primarily to the stringent alignment tolerance imposed by the sensitivity of the coupling efficiency to transverse offset.

4.0 REFERENCES

1. Zachos, T. H., and J. C., "Resonant Modes of GaAs Junction Lasers - III: Propagation Characteristics of Laser Beams with Rectangular Symmetry", IEEE Journal of Quantum Electronics, QE-6:6, 1970, p. 317.
2. Zachos, T. H., "Gaussian Beams from GaAs Junction Lasers", Applied Physics Letter, 12:9, 1968, p. 318.
3. Casey, H. C. Jr., Sell, D. D., and Panish, M. B., "Refractive Index of $\text{Al}_x\text{Ga}_{1-x}\text{As}$ Between 1.2 and 1.5 eV", Applied Physics Letters, 24:2, 1974, pp. 63-65.
4. Hocker, G. B., and Burns, W. K., "Modes in Diffused Optical Waveguides of Arbitrary Index Profile", IEEE Journal of Quantum Electronics, 11:6, 1975, p. 270.
5. Kaminow, I. P., and Carruthers, J. A., "Optical Waveguiding Layers in LiNbO_3 and LiTaO_3 ", Applied Physics Letters, 22, 1973, pp. 326-328.
6. Schmidt, R. V., and Kaminow, I. P., "Metal-Diffused Optical Waveguides in LiNbO_3 ", Applied Physics Letters, 25:8, 1974, pp. 458-460.
7. Conwell, E. M., "Modes in Optical Waveguides Formed by Diffusion", Applied Physics Letters, 23:6, 1973, p. 328.
8. Naitoh, H., Nunoshita, M., and Nakayama, T., "Mode Control of Ti-Indiffused LiNbO_3 Slab Optical Waveguide", Applied Optics, 16:9, 1977, pp. 2546-2549.
9. Fukuma, N. J., and Iwasaki, H., "Optical Properties in Titanium-Diffused LiNbO_3 Strip Waveguides", Journal of Applied Physics
10. Burns, W. K., Klein, P. H., West, E. J., and Plew, L. E., "Ti Diffusion in Ti: LiNbO_3 Planar and Channel Optical Waveguides", to be published.
11. CRC Standard Mathematical Tables, 19th Edition, Selby, S. M., Editor, The Chemical Rubber Company, Cleveland, 1971, p. 518.
12. Jahnke, E., and Ende, F., Tables of Functions with Formula and Curves, 4th Edition, Dover Publications, New York, 1945.
13. Tables of Bessel Function of Fractional Order, the Computation Laboratory of the National Applied Mathematics Laboratories, U.S. National Bureau of Standard, Vol. I, Columbia University Press, New York, 1948.
14. Botez, D., "Near and Far-Field Analytical Approximations for the Fundamental Mode in Symmetric Waveguide DH Lasers", RCA Review, 39, 1978.
15. Butler, J. K., and Kressel, H., "Design Curves ofr Double-Heterojunction Laser Diodes", RCA Review, 38, 1977, pp. 542-558.

16. Botez, D., and Ettenberg, M., "Beamwidth Approximations for the Fundamental Mode in Symmetric Double-Heterojunction Lasers", IEEE Journal of Quantum Electronics, QE-14:11, 1977, pp. 542-558.
17. Hocker, G. B., "Diffused Optical Waveguide Modes", unbulished results.
18. Hunsperger, R. G., Yariv, A., and Lee, A., "Parallel End-Butt Coupling for Optical Integrated Circuits", Appl. Opt. 16, 1026 (1977).